amU
Aix Marseille Université

NNT : 2024AIXM0001

THÈSE DE DOCTORAT

Soutenue à AMU — Aix-Marseille Université
le 19 decembre 2024 par

Isael Alejandro HERRERA HERNANDEZ

From 2D polarized fields to 3D Stokes polarimetric imaging at nanoscales.

Methods and applications.

Discipline
Physique et Sciences de la Matière

Spécialité
Optique, Photonique
et Traitement d'Image.

École doctorale
Ecole Doctorale Physique et Sciences de la Matière ED352

Laboratoire/Partenaires de recherche
Institut Fresnel

Composition du jury

Rafael PIESTUN Professor. University of Colorado Boulder.	Rapporteur
Gabriel MOLINA Research professor. Centro de Física de Materiales.	Rapporteur
Etienne BRASSELET Directeur de Recherche. Laboratoire Ondes et Matière d'Aquitaine.	Président du Jury
Samira KADHIR Maître de conférences. Université Côte d'Azur.	Examinatrice
Sophie BRASSELET Directrice de recherche. Institut Fresnel.	Directrice de thèse
Miguel A. ALONSO Professeur d'Université. Institut Fresnel.	Co-Directeur de thèse

INSTITUT FRESNEL

cnrs

Affidavit

I, undersigned,Isael Alejandro Herrera Hernandez hereby declare that the work presented in this manuscript is my own work, carried out under the scientific supervision of Miguel A. Alonso and Sophie Brasselet„ in accordance with the principles of honesty, integrity and responsibility inherent to the research mission. The research work and the writing of this manuscript have been carried out in compliance with both the french national charter for Research Integrity and AMU charter on the fight against plagiarism.

This work has not been submitted previously either in this country or in another country in the same or in a similar version to any other examination body.

Marseille le 24 Octobre 2024



This work is licensed under Creative Commons Attribution-NonCommercial-NoDerivatives 4.0 International Public License

Publications list and participation in conferences.

List of publications:

1. Isael Herrera, Luis A. Aleman-Castaneda, Sophie Brasselet, and Miguel A. Alonso, "Stokes-based analysis for the estimation of 3D dipolar emission," J. Opt. Soc. Am. A 41, 2134-2148 (2024). https://doi.org/10.1364/JOSAA.538706.

2. Isael Herrera, Luis. A. Aleman-Castaneda, Miguel. A. Alonso, and Sophie. Brasselet, Nanoscale polarized imaging in 3D, in Optica Imaging Congress 2024 (3D, AOMS, COSI, ISA, pcAOP), Technical Digest Series (Optica Publishing Group, 2024), paper IM3G.7. https://doi.org/10.1364/ISA.2024.IM3G.7.

3. David Marco, Isael Herrera, Sophie Brasselet, and Miguel A. Alonso; Propagation-Invariant Optical Meron Lattices. ACS Photonics. 11 (6), 2397-2405 (2024). https://doi.org/10.1021/acsphotonics.4c00292.

4. David Marco, Isael Herrera, Sophie Brasselet, Miguel A. Alonso. Periodic skyrmionic textures via conformal cartographic projections. APL Photonics 9, 110803 (2024). https://doi.org/10.1063/5.0230959.

5. Rodrigo Gutiérrez-Cuevas, Luis A. Aleman-Castaneda, Isael Herrera, Sophie Brasselet, Miguel A. Alonso; Vectorial phase retrieval in super-resolution polarization microscopy. APL Photonics. 9 (2), 026106. 2024. https://doi.org/10.1063/5.0179906.

Participation in conferences and summer schools:

1. Presentation at Optica Sensing, Toulouse, France 2024.

2. Presentation at the Journees Imagerie Optique Non-Convenionelle, Paris France. 2024

3. Poster presentation at the conference Focus on microscopy, Geneoa. Italy, 2024.

4. Participation and poster presentation at the Summer School Waves in Complex Media. Les Houches, France. 2023

5. Practical workshop presentation at the CNRS Thematic School MiFoBio2023, Presqu'île de Giens. France. 2023.

6. Poster presentation at the conference Biophotonics and Optical Angular Momenum, Paris, France. 2023.

7. Presentation at the conference Focus on Microscopy (FOM). Porto, Portugal. 2023

8. Poster presentation at the conference Single Molecule Localization Microscopy Symposium (SMLMS), Paris, France. 2022

9. Poster presentation at the conference International Conference on Optical Angular Momentum, (ICOAM), Tampere, Finland. (2022).

Résumé et mots clés

Dans ce travail, nous étudions divers aspects de la polarisation de la lumière, des échelles macroscopiques aux échelles nanoscopiques. Nous proposons et mettons en œuvre des faisceaux présentant toutes les ellipses de polarisation possibles dans le régime paraxial. Nous expliquons comment générer et mesurer des structures de polarisation skyrmioniques définies à partir de projections conformes proposés dans le cadre de la cartographie. De plus, nous avons généré et mesuré des réseaux de Méron invariants lors de la propagation.

Si la mesure de la polarisation de la lumière à des échelles macroscopiques peut être réalisée simplement avec des caméras et des éléments optiques courants tels que des polariseurs et des lames à retard, mesurer la polarisation de la lumière à des échelles nanoscopiques, où le champ peut osciller en 3D, n'est pas aussi simple. Ce domaine a fait l'objet d'études au cours des dernières décennies. Dans ce travail, nous proposons des outils théoriques, numériques et expérimentaux pour explorer les états de polarisation 3D des champs lumineux.

Les bases de ce travail reposent sur les paramètres dits *Stokes-Gell-Mann généralisés*, un ensemble de neuf paramètres qui décrivent entièrement les aspects géométriques des champs électriques. Nous avons étendu le champ d'application de ces paramètres à la description des sources dipolaires et à leur mesure avec des microscopes optiques.

Un autre domaine de recherche qui s'est développé ces dernières années est la mesure de fluorophores orientés en 3D. Depuis le développement des techniques de microscopie à super-résolution, un intérêt croissant s'est manifesté pour la mesure non seulement de la position 3D des molécules individuelles, mais aussi de leur orientation 3D. Dans ce travail, nous tirons parti de la nature dipolaire des fluorophores uniques et étendons les applications des paramètres de Stokes-Gell-Mann à l'étude des molécules orientées en 3D.

Mots clés: polarisation, microscopie, imagerie, nanoparticules, molécules.

Abstract and keywords

In this work, we study aspects of light polarization, from macroscopic to nanoscopic scales. We propose and implement beams exhibiting all possible polarization ellipses in the paraxial regime. We explain how to generate and measure such skyrmionic polarization structures defined from conformal mappings proposed in the context of cartography. Also, we generate and measure propagation invariant Meron lattices.

While measuring the polarization of light at macroscopic scales can be done simply with cameras and common optical elements such as polarizers and wave plates, measuring it at nanoscopic scales, where the field can oscillate in 3D, is not straightforward. This has been a field of study in the last decades. In this work, we propose theoretical, numerical and experimental tools to explore 3D polarization states at nanoscales in imaging configuration.

The foundations of this work are the so-called *Generalized Stokes-Gell-Mann* parameters, a set of nine parameters that completely describe the geometrical aspects of the electric fields oscillations. We have extended the range of applications of those parameters to the description of dipole sources and their measurement with optical microscopes.

Another area of research that has been developed in recent years is the measurement of individual 3D-oriented fluorophores. Since the development of super-resolution microscopy techniques, there has been an interest in measuring not only the 3D position of single molecules but also their 3D orientation. In this work, we benefit from the dipolar nature of single fluorophores and extend the range of applications of the Stokes-Gell-Mann parameters to the study of 3D-oriented molecules.

Keywords: polarization, microscopy, imaging, nanoparticles, molecules.

Résumé étendu en français.

Dans cette thèse, nous explorons les aspects théoriques et expérimentaux de la polarisation 3D ou de la polarisation non paraxiale de la lumière. Nous discutons de la manière dont il est possible de mesurer cette propriété de la lumière à des échelles nanométriques. Nous décrivons également la relation qui existe entre la mesure de dipôles électriques orientés en 3D avec des objectifs de microscope et la polarisation non paraxiale. Nous expliquons l'application de techniques polarimétriques non paraxiales dans l'étude de molécules orientées en 3D dans le contexte de la microscopie de fluorescence. Nous commençons par discuter des aspects théoriques de la lumière.

La description des champs optiques dans l'espace libre considère généralement des ondes se propageant dans une seule direction, de sorte que les oscillations du champ sont limitées au plan transverse. Cette hypothèse est valable pour des faisceaux faiblement divergents et est connue sous le nom d'approximation paraxiale. Mathématiquement (pour des champs monochromatiques), cela signifie que lorsque le champ est décrit comme une superposition d'ondes planes, la principale contribution au spectre provient d'ondes planes dont les vecteurs d'onde sont presque contenus sur le même axe.

Bien qu'il existe aujourd'hui de nombreuses techniques pour mesurer le champ paraxial complexe à l'aide de configurations interférométriques, de caméras de phase ou d'algorithmes de récupération de phase, des techniques telles que la polarimétrie de Stokes et de Muller sont encore en constante amélioration et développement en raison de la simplicité qu'elles offrent en se basant uniquement sur des mesures d'intensité des projections de polarisation du champ, sans avoir besoin d'un faisceau de référence, d'auto-interférence ou de post-traitement coûteux en termes de calcul.

Caractériser les oscillations vectorielles du champ électrique en un point donné de l'espace en termes des paramètres de Stokes est défini comme la *polarimétrie de Stokes*. Le chemin décrit par le vecteur du champ électrique peut être le même au fil du temps, ou partiellement ou complètement aléatoire. Le premier décrit la lumière totalement polarisée, tandis que le second correspond à la lumière partiellement polarisée ou non polarisée (également appelée dépolarisée).

Il est bien connu que, dans le régime paraxial, les champs totalement polarisés décrivent (en tout point de l'espace) une trajectoire elliptique contrainte à osciller dans le plan transverse à la direction de propagation. Cela est une conséquence directe des équations de Maxwell pour les champs électromagnétiques se propageant dans un milieu isotrope.Dans ce cas particulier, il est possible d'associer chaque ellipse paraxiale à la sphère de Poincaré. Les états entièrement polarisés correspondent à des points sur la surface de la sphère. L'équateur correspond à une polarisation linéaire et les

pôles nord/sud à une polarisation circulaire gauche/droite. L'orientation et l'ellipticité de l'ellipse de polarisation physique sont une fonction des angles sphériques $\phi \in [0, \pi]$ et $\theta \in [-\pi/2, \pi/2]$, la spin étant codée dans le signe de θ.

La trajectoire elliptique est également observée dans les champs non paraxiaux totalement polarisés, où l'ellipse peut être orientée dans n'importe quelle direction 3D. Ce chemin décrit par le champ est connu sous le nom d'ellipse de polarisation.

Dans ce cas, il n'est pas possible de construire une sphère pour représenter tous les états de polarisation possibles. Des structures plus complexes sont nécessaires, comme cela est discuté dans d'autres travaux. [1].

Avec des configurations expérimentales simples appliquées dans le régime paraxial, il est possible de mesurer non seulement les aspects géométriques de l'ellipse de polarisation, c'est-à-dire ses axes majeur et mineur (où, dans le cas général des champs non-paraxiaux, ces axes sont des vecteurs en 3D) mais aussi le sens de rotation et le degré d'indépendance temporelle des oscillations.

Avant de discuter des méthodes de mesure des aspects de polarisation de la lumière, abordons les deux cas limites des champs entièrement polarisés. Le premier cas correspond à ce que l'on appelle la lumière polarisée linéairement, où le champ oscille en décrivant une ligne droite, et le second cas correspond à la lumière polarisée circulairement. Ces deux limites sont importantes car tout état paraxial complètement polarisé peut être décrit comme une superposition de deux états de polarisation linéaire ou circulaire orthogonaux.

Pour la lumière paraxiale polarisée elliptiquement, la direction de l'oscillation du champ est appelée *spin*, et les termes Droite/Gauche sont utilisés pour caractériser cette direction. Lorsqu'un champ entièrement polarisé est autorisé à osciller en 3D, le spin doit être décrit en termes de vecteur. Nous définissons le spin comme le vecteur orthogonal au plan d'oscillation selon la règle de la main droite, et dont l'amplitude est proportionnelle à la surface délimitée par l'ellipse.

Pour les champs non-paraxiaux partiellement polarisés, la trajectoire tracée par les oscillations diffère d'une simple ellipse. Néanmoins, certaines propriétés statistiques restent mesurables, telles que le spin moyen et l'ellipsoïde d'inertie, qui caractérisent le volume exploré par les oscillations du champ. Le *degré de polarisation* est un paramètre utilisé pour quantifier à quel point un champ est totalement polarisé ou dépolarisé .

En réalisant des mesures d'intensité uniquement sur des champs entièrement polarisés, il est possible de connaître l'ellipse tracée dans le temps à différentes positions par le champ électrique local. Cependant, il est impossible de connaître le point de départ de la trajectoire du champ pour toutes les positions. En d'autres termes, il est impossible de connaître la *phase globale* du champ, qui n'est accessible que par des approches interférométriques.

La génération et la mesure de l'amplitude et de la phase des champs non-paraxiaux ont été des sujets de recherche au cours des deux dernières décennies. La plupart des méthodes reposent sur la mesure du signal diffusé par des nanocapteurs ou des nanotips de balayage. Cependant, ces méthodes sont limitées au test du champ à une position à la fois, contrairement au régime paraxial où les caméras permettent des

mesures simultanées à différents points d'un plan.

Les tentatives de décrire la polarisation des faisceaux de champ non-paraxiaux dans un cadre théorique similaire au formalisme de Stokes remontent à près d'un siècle, curieusement dans les travaux du physicien marseillais Soleillet . Cependant, la généralisation du formalisme de Stokes aux champs non-paraxiaux a été récemment proposée. La contrepartie expérimentale, c'est-à-dire la mise en œuvre d'une polarimétrie complète des champs non-paraxiaux et la description d'un polarimètre non-paraxial en termes du formalisme généralisé de Stokes, reste peu explorée, entre autres en raison du fait que les champs non-paraxiaux varient de manière significative à des échelles de longueur d'onde.

Pour le moment, discutons de quelques techniques expérimentales proposées pour mesurer des champs non-paraxiaux.La mesure directe des champs optiques non-paraxiaux a été un domaine de recherche actif au cours des deux dernières décennies Dans le régime paraxial, des configurations simples basées sur des mesures uniquement d'intensité ou des configurations interférométriques permettent une mesure complète de la nature vectorielle complexe de la lumière paraxiale avec un simple post-traitement des données. Pour les champs non-paraxiaux, la caractérisation complète de la lumière à l'échelle nanométrique dépend encore de configurations expérimentales complexes et de traitements impliquant des nanotips de balayage, des couches fluorescentes ou l'analyse en champ lointain du signal généré par des nanoparticules.

Des expériences préliminaires [2] dans des champs non-paraxiaux illustrent la présence d'une composante de champ longitudinal en excitant des molécules fluorescentes sur une lamelle et en mesurant dans le plan d'image d'un objectif de microscope à NA élevée. Différentes morphologies dans la distribution d'intensité des molécules étaient associées à diverses orientations 3D qui ne pouvaient être excitées que par la présence d'une composante de champ parallèle à cette direction.

Des mesures quantitatives de l'amplitude et de la phase du champ sont aujourd'hui possibles en utilisant des pointes de balayage en champ proche combinées à des configurations interférométriques. Ces méthodes sont particulièrement adaptées pour mesurer des champs évanescentes avec des structures sublongueur d'onde. Au cours de la dernière décennie, l'utilisation de nanoparticules a été proposée pour réaliser des mesures quantitatives de champs non-paraxiaux. Une seule particule est déposée sur une lamelle montée sur un support contrôlé en translation qui permet la mesure du champ dans un plan. Le signal est collecté par un objectif de microscope et les mesures sont effectuées à la sortie de l'objectif. Avec cette configuration, il est possible de mesurer des structures de polarisation sublongueur d'onde telles que des bandes de Möbius [3]. Des configurations similaires ont été utilisées pour mesurer d'autres champs structurés non-paraxiaux. Arrêtons-nous un moment pour discuter des méthodes basées sur l'interaction du champ non-paraxial avec des nanosondes.

L'utilisation de nanoparticules comme sondes de champ présente plusieurs avantages par rapport aux nanotips de balayage ; en particulier, elle représente une approche plus flexible qui pourrait être mise en œuvre dans des microscopes optiques commerciaux. Bauer *et al* [4] ont proposé une méthode où un objectif à haute ou-

verture numerique NA est utilisé pour générer un champ non-paraxial testé par une sphère en nanogold. Le motif d'interférence entre le faisceau entrant et le champ diffusé est mesuré dans le plan de foyer arrière d'un second objectif. Ensuite, différentes régions du plan pupille sont intégrées pour créer un ensemble de données qui dépend de la position de la sphère. En ajustant ces données à un modèle basé sur la diffusion de Mie, les auteurs ont pu reconstruire l'amplitude et la phase des faisceaux fortement focalisés sur des zones de 1 μm^2 tout en résolvant des structures sub-longueur d'onde.

Dans d'autres méthodes les auteurs ont réalisé une polarimétrie de Stokes paraxiale sur le signal collimaté diffusé par les nanosphères. Eismann *et al* ont placé une particule sur un prisme utilisé pour générer un champ évanescent. Le signal collecté par un objectif à haute ouverture numérique a été analysé dans le plan de Fourier à l'aide d'un polarimètre standard et comparé aux simulations. Dans un travail similaire, Rodriguez-Herrera *et al* [5] ont prouvé la conversion de moment angulaire de spin en moment angulaire orbital de la lumière en focalisant fortement un faisceau avec une lentille à haute ouverture numérique. La même lentille est ensuite utilisée pour collecter le signal diffusé par une nanosphère. Ils ont effectué une polarimétrie de Stokes paraxiale sur le signal collecté au plan pupillaire. Dans ces travaux, les informations de localisation de la particule sont perdues puisque les mesures sont effectuées au plan pupillaire. Néanmoins, les auteurs peuvent reconstruire une distribution de champ en corrélant la position de la particule aux déplacements de la scène piézoélectrique. Une autre caractéristique commune de ces méthodes est que la nanosonde peut être considérée comme un diffuseur dipolaire avec un moment dipolaire $\hat{\boldsymbol{\mu}}$. Le problème de la mesure des champs non-paraxiaux devient alors un problème de mesure efficace du dipôle.

Lors de l'utilisation d'une sonde dipolaire, il convient de veiller à ce que le système de mesure soit sensible à toutes les configurations dipolaires possibles, ce qui n'est pas nécessairement vrai pour des configurations simples d'objectif à haute NA et de caméra. Le problème de la mesure des émetteurs dipolaires et de leur localisation en 3D a été largement étudié dans les techniques modernes de microscopie à molécule unique. Arrêtons-nous maintenant pour discuter de la mesure des molécules uniques.

La microscopie de localisation à une seule molécule (SMLM) est une famille de méthodes de microscopie optique à super-résolution qui ont été proposées au cours des deux dernières décennies pour observer des objets avec des structures sub-longueur d'onde [6]. Ces techniques ont dépassé la limite de résolution en mesurant les positions individuelles des molécules uniques (émetteurs dipolaires), puis en reconstruisant l'objet cible en accumulant toutes les positions individuelles. En particulier, des techniques comme la microscopie de localisation photoactivée (PALM) [7], la microscopie de reconstruction optique stochastique (STORM) [8], ou l'accumulation de points pour l'imagerie en topographie à l'échelle nanométrique (PAINT) [9] sont basées sur la mesure du centroïde de la distribution d'intensité associée à des fluorophores uniques. La différence entre ces techniques réside dans le mécanisme physique/chimique qui permet la sparsité temporelle des détections, mais leur principe de reconstruction est le même : une caméra est placée dans le plan conjugué au plan de l'échantillon et il est supposé que la distribution d'intensité mesurée, également ap-

pelée fonction de répartition ponctuelle (PSF), est décrite par une distribution gaussienne 2D . En trouvant le centre de cette distribution, une image à super-résolution peut être obtenue en traçant les fluorophores comme une distribution gaussienne avec un écart-type égal à l'incertitude du centre estimé.

On suppose qu'un modèle de PSF 2D gaussien est valide tant que le fluorophore explore plusieurs orientations plus rapidement que le temps d'intégration de la caméra (c'est-à-dire qu'il se comporte comme un émetteur dépolarisé). Lorsque la mobilité du fluorophore est contrainte dans une direction moyenne, une PSF plus complexe peut être observée [10–13]. Cependant, mesurer l'orientation 3D réelle de l'émetteur n'est pas trivial ; même lorsque l'émetteur a une orientation fixe, l'information complète sur l'orientation 3D n'est pas accessible en mesurant uniquement la PSF naturelle dans une configuration simple d'objectif, de lentille de tube et de caméra. Pour une molécule avec une orientation 3D fixe, son vecteur moment dipolaire est donné par $\hat{\boldsymbol{\mu}} = (\sin\eta\cos\xi, \sin\eta\sin\xi, \cos\eta)$, où (η, ξ) sont respectivement les angles polaire et azimutal. Cependant, les molécules ne sont pas statiques ; elles peuvent osciller dans le temps, plus vite que le temps d'intégration des détecteurs. Dans des situations où la molécule oscille isotropiquement autour d'une direction fixe, elle décrit une distribution dont l'angle d'ouverture δ est une mesure de son oscillation. Cette quantité est analogue au degré de polarisation des champs non paraxiaux.

Ces dernières années, un intérêt croissant s'est développé pour l'élaboration de méthodes de microscopie d'orientation et de localisation de molécules uniques (SMOLM) afin d'extraire l'orientation, l'oscillation et la position 3D des fluorophores à partir de leurs PSF. Il est possible de classer ces méthodes en deux familles générales : l'ingénierie de la PSF et les mesures ratiométriques [14]. Dans l'ingénierie de la PSF, un objet qui module la phase et/ou la polarisation est placé dans le plan de pupille du microscope, et il est parfois suivi par la séparation du signal en plusieurs composants de polarisation. La PSF résultante peut dépendre de manière significative et sans ambiguïté des paramètres d'orientation et de localisation de l'émetteur. Dans les schémas ratiométriques, le signal est séparé en canaux soit par polarisation soit par filtres spatiaux, le déséquilibre relatif de l'énergie dans les canaux est associé aux paramètres d'orientation et/ou spatiaux.

L'approche proposée dans cette thèse pour réaliser une polarimétrie non paraxiale s'inspire des techniques d'ingénierie de la PSF proposées dans la SMOLM, où des dipôles linéaires sont mesurés pour récupérer l'orientation 3D, le wobbling et la position des molécules. Dans ce projet de thèse, nous proposons d'utiliser un réseau de diffuseurs dipolaires pour mesurer des champs non paraxiaux à plusieurs positions en une seule prise. Ce réseau est placé près du plan focal d'un objectif à haute ouverture numérique dans une configuration de réflexion standard. Le système repose sur la séparation du signal diffusé en ses composantes de polarisations circularires gauche et droite, et de sa mesure dans une configuration d'imagerie, ce qui permet de découpler les informations spatiales du dipôle. L'utilisation de diffuseurs dipolaires n'est pas anodine; le dipôle induit sur un diffuseur de Rayleigh est proportionnel au champ externe. Ainsi, le problème de la mesure de la polarisation se réduit à la mesure du dipôle à partir du signal émis par le diffuseur.

Dans le chapitre 1, nous proposons un cadre basé sur les paramètres de Stokes généralisés pour étudier des situations où des dipôles elliptiques sont mesurés avec un microscope à haute NA afin de prendre en compte la lumière elliptique. Nous prouvons que l'information complète des sources dipolaires peut être obtenue en séparant simplement le signal en ses composantes de polarisation circulaire. Nous exploitons les propriétés mathématiques des paramètres généralisés de Stokes-Gell-Mann pour décrire le système de mesure et analyser les données.

Dans le Chapitre 2, nous parlons de la manière de structurer la lumière avec un modulateur spatial de lumière. Arrêtons-nous un moment pour discuter un peu du concept de lumière structurée. La lumière est considérée comme une onde électromagnétique avec différents degrés de liberté : amplitude, phase, polarisation et fréquence. Au cours des dernières décennies, un grand effort théorique et expérimental est réalisé pour développer de nouvelles façons de manipuler et de contrôler des faisceaux de lumière monochromatique se propageant dans l'espace libre pour des applications en bio-imagerie, astronomie, communication quantique et classique, ou micromanipulation, pour ne citer que quelques exemples. De nos jours, il est courant d'utiliser des métasurfaces, des modulateurs de lumière spatiale basés sur la technologie des cristaux liquides, des dispositifs numériques à micromiroirs ou certaines optiques transparentes pour effectuer une modulation spatiale de l'amplitude, de la phase et de la polarisation des faisceaux monochromatiques. Tous ces progrès dans le contrôle de la lumière permettent la mise en œuvre de certaines structures lumineuses exotiques telles que des faisceaux invariants à la propagation, des faisceaux accélérants, des nœuds optiques, des Hopfions optiques, des skyrmions optiques, des mérons ou des bandes de Möbius de lumière. Nous décrivons les méthodes numériques et expérimentales derrière la génération et la mesure de réseaux de skyrmions et de mérons optiques via la projection de la sphère de Poincaré vers l'espace physique.

Nous introduisons deux familles de textures périodiques skyrmioniques. La première est obtenue en projetant la sphère de Poincaré dans l'espace réel à l'aide de transformations conformes introduites au 19e siècle dans le contexte de la cartographie. La seconde famille correspond à des réseaux de Méron générés par l'interférence de quelques ondes planes placées dans un anneau dans l'espace de Fourier, ce qui confère au champ la propriété d'invariance de propagation.

Dans le Chapitre 3, nous décrivons l'émission dipolaire observée avec un microscope, illustrons le calcul numérique de la PSF vectorielle du dipôle et montrons des résultats numériques qui concordent avec la littérature.

Nous définissons le concept de base de Stokes Gell-Mann pour caractériser les capacités de tout microscope à mesurer des dipôles elliptiques. Nous expliquons comment calculer et interpréter les éléments de la base de Stokes-Gell-Mann.

Les émetteurs dipolaires sont la source de radiation la plus courante. À des fréquences optiques, une pléthore de systèmes physiques peut être considérée comme des sources dipolaires : atomes, molécules fluorescentes, nanoparticules métalliques et points quantiques, pour n'en nommer que quelques-uns. Dans l'imagerie et les études de propagation de la lumière à travers des milieux complexes, l'interaction de la lumière avec la matière peut être simulée en supposant que le milieu est composé

d'un grand nombre de diffuseurs dipolaires.

Les dipoles électriques sont caractérisés par leur vecteur moment dipolaire $\hat{\boldsymbol{\mu}} = (\mu_x, \mu_y, \mu_z)$, dont les composants complexes, $\mu_i = A_i e^{i\phi_i}$, encodent l'amplitude et la phase de la projection d'oscillation le long des axes cartésiens. Nous nommons *dipoles rectilignes* le cas spécifique où les trois composants oscillent en phase, et *dipoles elliptiques* celui pour lequel certains des composants dipolaires oscillent hors phase. Les dipoles rectilignes sont une source de lumière polarisée linéairement, tandis que les dipoles elliptiques sont une source de lumière polarisée elliptiquement. Cependant, la radiation produite par ces dipoles n'est pas isotrope et dépend de la direction d'observation.

L'objectif principal de Chapitre 3 est de décrire les conditions expérimentales nécessaires pour mesurer $\hat{\boldsymbol{\mu}}$ dans le cadre des paramètres généralisés de Stokes-Gell-Mann lorsque la source dipolaire est observée avec un objectif de microscope à grande ouverture numérique en configuration d'imagerie. Pour un dipole rectiligne, les composants de $\hat{\boldsymbol{\mu}}$ sont les coordonnées cartésiennes de son orientation en 3D.

Dans le Chapitre 4, nous introduisons C-3POL, une configuration expérimentale simple basée sur la projection en composantes circulaires gauche et droite, pour mesurer des dipôles rectilignes et elliptiques orientés en 3D en une seule prise. Nous discutons de ses capacités à mesurer l'ensemble complet des 9 paramètres généralisés de Stokes-Gell-Mann. En calculant la matrice d'information de Fisher du système, nous montrons que seules deux ensembles de variables sont corrélés, contrairement à d'autres systèmes simples (discutés dans le Chapitre 3) où plus de variables peuvent être corrélées. Nous commentons la présence de vortex optiques dans les composants de polarisation droite et gauche de la radiation dipolaire et comment cette caractéristique peut être associée à des systèmes expérimentaux capables de mesurer des dipôles orientés en 3D.

Nous introduisons une méthodologie basée sur la linéarité de la forme de la PSF par rapport à la base de Stokes-Gell-Mann pour analyser les données. Nous découplons le problème de la mesure des neuf paramètres de Stokes-Gell-Mann et de la position 3D des émetteurs en créant un ensemble de bases pré-calculées qui prennent en compte la localisation 2D et en sélectionnant celle associée au meilleur ajustement. Nous estimons la coordonnée axiale via une approximation de Taylor. Dans les deux cas (récupération des paramètres de Stokes et localisation 3D), l'inversion est basée sur des opérations de multiplication matricielle, d'où l'algorithme peut être utilisé pour analyser de grands ensembles de données. Nous discutons également de la compatibilité de cet algorithme avec d'autres méthodes basées sur la mesure des PSF.

Pour le cas des dipôles rectilignes, nous montrons qu'il est possible de mesurer sans ambiguïté la position 3D des émetteurs sur la base d'une expansion de Taylor. Nous présentons des simulations de Monte Carlo pour le cas des dipôles rectilignes orientés en 3D et montrons les performances dans le régime de haut et bas nombre de photons. Nous observons des performances similaires dans la récupération des informations de localisation et d'orientation par rapport aux techniques SMLM et SMOLM à la pointe de la technologie. Dans les chapitres suivants, nous discutons de l'application de C-3POL dans la polarimétrie non paraxiale et la microscopie d'orientation de molécules

uniques.

Dans le Chapitre 5, nous présentons des résultats expérimentaux où un arrangement de particules métalliques nanométriques est utilisé pour mesurer des champs électriques non paraxiaux. Enfin dans le Chapitre 6, nous montrons également des résultats en microscopie de fluorescence où la détection et la mesure orientationnelle de nombreuses molécules sont utilisées pour construire une image de super-résolution de l'actine dans une cellule, ainsi que pour obtenir des informations sur la localisation 3D et l'orientation 3D de fluorophores. Dans la Fig. 1, nous présentons un résumé graphique de ce projet de thèse.

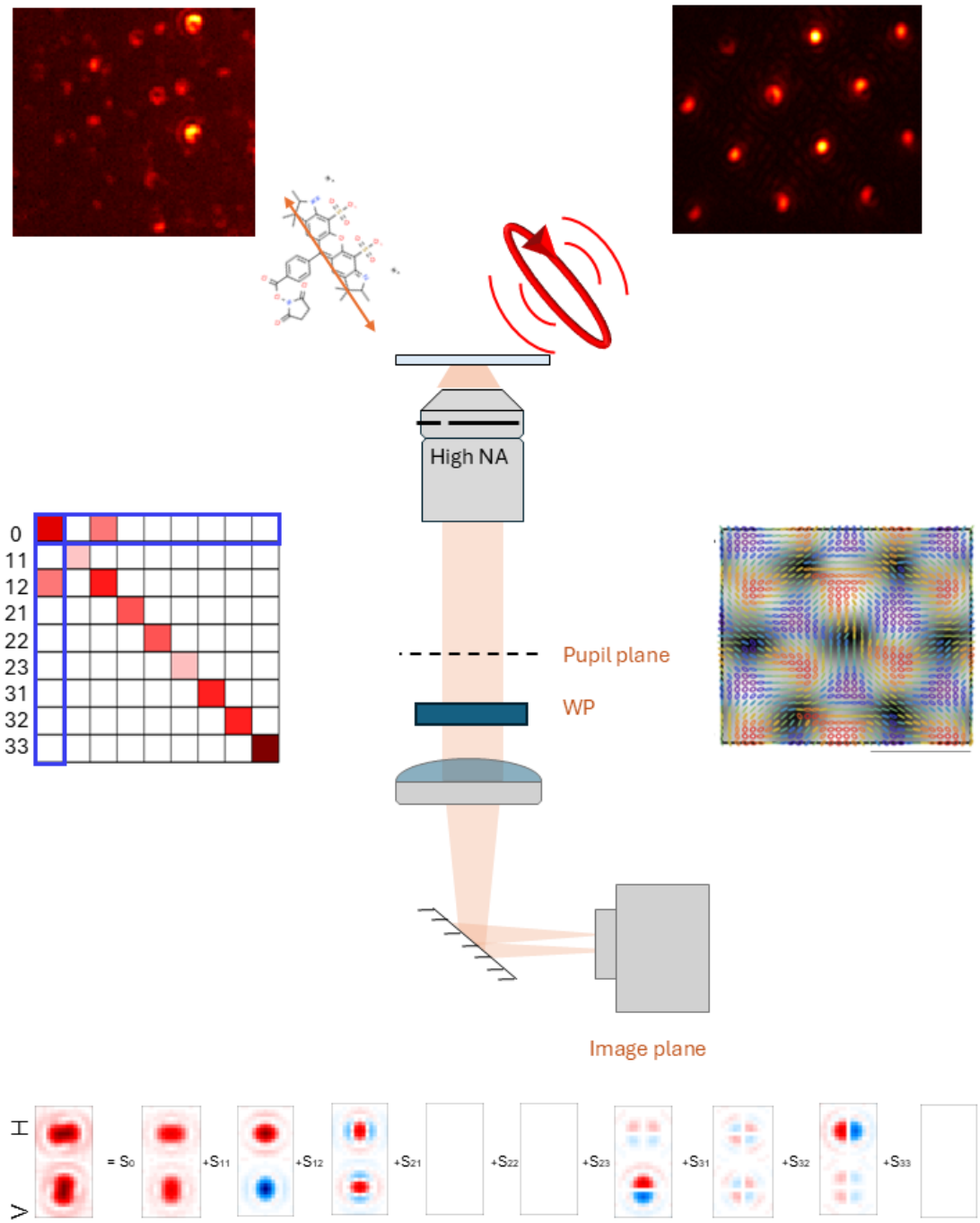

Figure 1.: Résumé graphique.La radiation de dipoles est capture avec un objectif de microscope pour mesurer l'orientation 3D des molécules, image de gauche, et de l'état de polarisation de la lumière en 3D, image de droit. Nous décrivons le rayonnemet en termes de bases de Stokes et caractérisons différents types de microscopes avec la matrice d'information de Fisher. De plus, nous présentons des états de lumière paraxiaux structurés spatialement qui présentent toutes les possibles ellipses de polarisation 2D.

Acknowledgments

I thank my supervisors, Sophie Brasselet and Miguel Alonso, who have supported and guided me from the beginning. I am grateful to them for this wonderful project, which allowed me to work on both its theoretical and experimental aspects. I have learned a lot from you! I will miss our discussions!

I would also like to thank the researchers, staff, and students of the Fresnel Institute, especially the members of the Mosaic team, who were always willing to help me whenever I needed it. In particular, I am grateful to Anne Sentenac, Frédéric Galland, Guillaume Baffou, Sandro Heuke, Luis Alemán Castañeda, Miguel Sison, Maximilian Langauer, Charitra Kumar, Pascal Nguyen, Eric Fantuzzi, David Marco, and Rodrigo Gutierrez, with whom I had very enriching conversations and discussions. I would also like to thank Sisira Suresh. It was both pleasant and helpful that we defended at the same time! I will never forget these last few months of hard work – we did it! I also want to thank all the people in Team Raccoon who made my PhD days more enjoyable: Carla, Vanessa, Maelle, Astrid, Clement, Armando, Tania, Moritz, Moritz S., Chrysa, Chang, Pierre, Lorry, and Naveen.

I would also like to thank my family, who have always supported and motivated me from the other side of the world: my mom, Isabel Hernández, my dad, Alejandro Herrera, and my sisters, Jimena and Erika. I also thank Esmeralda Aguilar for all her support and for our long conversations across the distance. Thank you for so many years of friendship! Additionally, I am grateful to my university friends, Samuel Corona and Alberto del Ángel, with whom I learned physics and who made my university years much more enjoyable! Finally, I want to thank my boyfriend, Alejandro Rivera, for still being here after 11 years!

Finally, I would like to thank the French people, who, through their taxes, funded my project via Aix-Marseille Université, the CNRS, and the ANR-21-CE24-0014 grant.

Contents

Affidavit 2

Publications list and participation in conferences. 3

Résumé et mots clés 5

Abstract and keywords 6

Résumé étendu en français. 7

Acknowledgments 16

Contents 17

1. Theory and methods in nonparaxial optical fields. 20
- 1.1. Paraxial and nonparaxial optical fields. . . . 20
- 1.2. 2D polarization. . . . 22
- 1.3. 3D Polarization. . . . 24
- 1.4. Experimental methods in the nonparaxial regime. . . . 27
  - 1.4.1. Measuring nonparaxial fields with nanospheres . . . 28
  - 1.4.2. Measuring 3D oriented molecules. . . . 29
  - 1.4.3. Stokes polarimetric imaging at nanoscales. . . . 31

2. Generation and measurement of spatially variant 2D polarized fields. 35
- 2.1. Introduction: Structured light. . . . 35
- 2.2. Structuring 2D polarized fields. . . . 36
- 2.3. Measuring 2D polarized fields. . . . 38
- 2.4. Special case of 2D beams: Skyrmion and Meron lattices. . . . 39
- 2.5. Periodic skyrmions via cartographic maps. . . . 41
- 2.6. Propagation invariant meron lattices. . . . 45
- 2.7. Final remarks 47

3. Measuring 3D oriented dipoles with a microscope: General considerations. 49
- 3.1. Introduction: 3D oriented dipoles in microscopy. . . . 49
- 3.2. Dipole PSF description in terms of Stokes-Gell-Mann basis. . . . 58
- 3.3. Stokes-Gell-Mann basis for polarized measurements. . . . 63
- 3.4. Fisher Information Matrix 66
- 3.5. Final remarks 70

4. C-3POL: circular polarization decomposition for measuring 3D oriented dipoles. 71
4.1. Introduction. . . . 71
4.2. Circular vs Linear polarization separation. . . . 72
4.3. Stokes-Gell-Mann Basis and FIM for the circular projection configuration. 76
4.4. Implementation. . . . 77
4.4.1. Registration. . . . 79
4.4.2. Initial 2D localization of dipole emitters. . . . 82
4.4.3. Background estimation. . . . 82
4.4.4. Stokes-Gell-Mann parameter estimation. . . . 83
4.4.5. Accurate Stokes-Gell-Mann parameter estimation and correction to the initial 2D location. . . . 84
4.4.6. 3D localization of dipole emitters. . . . 86
4.5. Numerical studies. . . . 90
4.5.1. Continuous medium and fully polarized rectilinear dipoles. . . . 90
4.5.2. Continuous medium and fully polarized elliptical dipoles. . . . 94
4.6. Final remarks . . . 97

5. Nonparaxial polarimetry. 99
5.1. Introduction . . . 99
5.2. Generating nonparaxial fields. . . . 100
5.3. Experimental results. . . . 101
5.3.1. Measurements of constant linearly polarized fields exhibiting 3D orientations. . . . 101
5.3.2. Measurements of 3D-oriented ellipses of polarization with opposite handedness. . . . 106
5.3.3. Measurement of the interference pattern of two p-polarized waves. 107
5.4. Final remarks. . . . 109

6. Stokes-Gell-Mann formalism applied to SMOLM. 111
6.1. Introduction. . . . 111
6.2. Photoselection of single 3D-oriented fluorophores on a coverslip by varying the excitation polarization. . . . 111
6.3. C-3POL applied to STORM. . . . 114
6.4. Final remarks . . . 117

Conclusion 119

Bibliography 122

ANNEXES 131

A. Complementary expressions. 132
.1. Conformal maps. . . . 132

.2. Computation of the Stokes-Gell-Mann derivatives basis. 132

1. Theory and methods in nonparaxial optical fields.

Sommaire

1.1. Paraxial and nonparaxial optical fields. 20
1.2. 2D polarization. 22
1.3. 3D Polarization. 24
1.4. Experimental methods in the nonparaxial regime. 27
1.4.1. Measuring nonparaxial fields with nanospheres 28
1.4.2. Measuring 3D oriented molecules. 29
1.4.3. Stokes polarimetric imaging at nanoscales. 31

1.1. Paraxial and nonparaxial optical fields.

The theoretical description of optical fields $\mathbf{E}(x,y,z)$ in free space usually considers waves propagating in one direction e.g. z, hence, the field oscillations are restricted to the transverse plane (x,y). This assumption is valid for slowly divergent beams and is referred to as the *paraxial approximation*. Mathematically (for monochromatic fields), this means that when the field is described as a superposition of plane waves [15],

$$\mathbf{E}(x,y,z) = \int_{-\infty}^{\infty}\int_{-\infty}^{\infty} \tilde{\mathbf{E}}_0(k_x,k_y)e^{i[k_x x+k_y y+k_z z]}\,dk_x\,dk_y \tag{1.1}$$

also known as the *angular representation*, the main contribution to the spectrum comes from plane waves whose wave vectors (k_x,k_y,k_z) satisfy the condition $k_z = \sqrt{k^2-k_x^2-k_y^2} \approx k - \frac{k_x^2+k_y^2}{2k}$, and $k = nk_0$, where n is the medium's refractive index and k_0 the wave number in vacuum. In the previous expression $\tilde{\mathbf{E}}_0(k_x,k_y)$ is the 2D Fourier transform of $\mathbf{E}(x,y,0)$. The physical field is recovered from 1.1 as $\mathscr{E}(x,y,z,t) = \mathrm{Re}\left[\mathbf{E}(x,y,z)e^{-i\omega t}\right]$. Although useful, the paraxial approximation fails to describe situations such as fields at the focus of a high numerical aperture lens, the diffraction of light close (at distances compared to the wavelength) to sources, evanescent fields or the image formation by high numerical aperture objectives. In these situations, the complete 3D nature of the fields needs to be taken into account.

Nowadays, there are many techniques for measuring the complex paraxial field $\mathbf{E}(x,y,z)$ such as interferometric configurations, phase cameras, or phase retrieval algorithms. Nevertheless, techniques such as Stokes and Muller polarimetry are

still in constant improvement and development due to the simplicity of relying on intensity-only measurements of the field polarization projections without the need of a reference beam, or computationally expensive post-processing.

The characterization of the vectorial oscillations of the electric field at a given point in space in terms of the so-called Stokes parameters (described in the next section) is referred to as *Stokes Polarimetry*. The path described by the electric field vector can be the same over time, or partially or completely ramdom. The former describes fully polarized light, while the latter corresponds to partially and unpolarized (also called depolarized) light.

It is well known that in the paraxial regime, fully polarized fields describe (at every point of the space) an elliptical trajectory constrained to oscillate in the plane transverse to the propagation direction. This is a direct consequence of Maxwell's equations for electromagnetic fields propagating in an isotropic medium. The elliptical trajectory is also observed in fully polarized nonparaxial fields, where the ellipse can be oriented in any 3D direction. This path described by the field is known as the *polarization ellipse*.

With simple experimental configurations (described below and throughout this thesis) applied in the paraxial regime, it is possible to measure not only the geometric aspects of the polarization ellipse i.e. its major/minor semi-axes **a**, **b** (where for the general case of nonparaxial fields these axes are vectors in 3D) but also the direction of rotation and the degree of time-independence of the oscillations.

Before discussing how to measure the polarization aspects of light, let us discuss the two limiting cases of fully polarized fields: 1) $|\mathbf{b}| = 0$ and 2) $|\mathbf{a}| = |\mathbf{b}|$. The first case corresponds to what is known as linearly polarized light where the field oscillates describing a straight line and the second case corresponds to circularly polarized light. These two limits are important because any fully polarized paraxial state can be described as a superposition of two orthogonal linear or circular polarization states.

For paraxial elliptically polarized light, the direction of the field oscillation is referred to as *handedness* and the terms Right/Left are employed to characterize this direction. When a fully polarized field is allowed to oscillate in 3D the handedness must be described in terms of a vector. We define the spin as the vector orthogonal to the oscillation plane according to the hand-right rule and whose magnitude is proportional to the area enclosed by the ellipse.

For nonparaxial partially polarized fields the path traced by the oscillations differs from a simple ellipse. Still, some statistical properties remain measurable, such as the average spin and the so-called ellipsoid of inertia, which characterize the volume explored by the field oscillations. The *degree of polarization* (P) is a parameter used to quantify how fully polarized ($P = 1$) or depolarized ($P = 0$) a field is.

By performing intensity-only measurements on fully polarized fields it is possible to know the ellipse traced in time at different positions by the local electric field; it's however, impossible to know the starting point of the field trajectory for all the positions. In other words, it is impossible to know the *global phase* of the field, which is only accessible by interferometric approaches.

Generating and measuring the amplitude and phase of nonparaxial fields has been

a research topic during the last two decades [2, 4, 16] in the context of nanophonics. Most of the methods rely on the measurement of the scattered signal by nanoprobes or scanning nanotips. However, these methods are limited to testing the field one position at a time contrary to the paraxial regime where cameras allow simultaneous measurements at different points of a plane.

Attempts to describe the polarization of nonparaxial fields in a theoretical framework similar to the Stokes formalism can be traced back almost a hundred years to the work of Soleillet [17]. However, the generalization of the Stokes formalism to nonparaxial fields have been recently proposed [1]. The experimental counterpart, i.e. the implementation of complete polarimetry of nonparaxial fields and the description of a nonparaxial polarimeter in terms of the generalized Stokes formalism remains underexplored, among other reasons because nonparaxial fields vary significantly at wavelength (nanometric) scales. The generalized Stokes parameters were applied recently in the study of 3D-oriented fluorophores within the context of single molecule orientation and localization microscopy (SMOLM) [18]. The connection between nonparaxial fields and 3D-oriented fluorescent molecules will be explained in the following sections.

We begin by reviewing the theoretical aspects of paraxial and nonparaxial Stokes polarimetry. We then discuss some methods for measuring nonparaxial fields. Finally, we review some techniques employed to measure 3D-oriented dipole sources and comment on their relation to nonparaxial polarimetry.

1.2. 2D polarization.

Quantitative polarimetry techniques are used to measure the local geometric oscillations of the electric field. In particular, for fully polarized fields, the goal is to measure the polarization ellipse and its handedness. For non-monochromatic fields, the physical electric field is given by $\mathscr{E} = \mathrm{Re}\left[\mathbf{E}(x,y,z,t)\right]$ where $\mathbf{E}(x,y,z,t) = \int \tilde{\mathbf{E}}(x,y,z,\omega)e^{-i\omega t}d\omega$. A general description of the field oscillations is given by the correlation matrix of the field $\mathbf{E}(x,y,z,t)$ with its complex conjugate $\mathbf{E}(x,y,z,t)^\dagger$:

$$\Gamma_{2D} = \langle \mathbf{E}(x,y,z,t)\mathbf{E}(x,y,z,t)^\dagger \rangle = \begin{pmatrix} \langle E_x E_x^* \rangle & \langle E_x E_y^* \rangle \\ \langle E_y E_x^* \rangle & \langle E_y E_y^* \rangle \end{pmatrix}, \tag{1.2}$$

where $\langle\cdot\rangle$ denotes time-averaged quantities. For simplicity, the spatial and temporal dependence has been omitted in the matrix elements, but it is important to remember that Γ_{2D} is defined in every point of the space. Note that for monochromatic beams we can neglect the temporal dependence and hence omit the temporal averaging. In this case the correlation matrix reduces to

$$\Gamma_{2D} = \begin{pmatrix} E_x E_x^* & E_x E_y^* \\ E_y E_x^* & E_y E_y^* \end{pmatrix}. \tag{1.3}$$

It is easy to see that the complex electric field $\mathbf{E} = (E_x, E_y)$ is the eigenvector of Γ_{2D} associated with its only non-zero eigenvalue. 3 Note that, in the general case, Γ_{2D} is Hermitian and its off-diagonal elements can be complex, so, four independent parameters are needed to completely parameterize it. We use the parametrization proposed by Stokes:

$$\Gamma_{2D} = \frac{1}{2}\begin{pmatrix} S_0 + S_1 & S_2 - iS_3 \\ S_2 + iS_3 & S_0 - S_1 \end{pmatrix} = \frac{1}{2}\sum_{m=0}^{3} S_m \sigma_m, \tag{1.4}$$

with

$$\begin{aligned} S_0 &= \text{Trace}[(\Gamma)_{2D}] = \langle E_x E_x^* \rangle + \langle E_y E_y^* \rangle, \\ S_1 &= \langle E_x E_x^* \rangle - \langle E_y E_y^* \rangle, \\ S_2 &= 2\text{Re}(E_x^* E_y) = \langle E_p E_p^* \rangle - \langle E_m E_m^* \rangle, \\ S_3 &= 2\text{Im}(E_x^* E_y) = \langle E_l E_l^* \rangle - \langle E_r E_r^* \rangle, \end{aligned} \tag{1.5}$$

where $E_{p,m} = (E_x \pm E_y)/\sqrt{2}$, are the field's Cartesian components along the axes **p**, **m** rotated by 45º with respect to **x**, **y**, and $E_{l,r} = (E_x \pm iE_y)/\sqrt{2}$ are the circular left **l** and right **r** polarization components. The last term in Eq. (1.4) is the decomposition of Γ_{2D} in terms of the identity matrix of 2×2 and the Pauli matrices:

$$\sigma_0 = \begin{pmatrix} 1 & 0 \\ 0 & 1 \end{pmatrix}, \quad \sigma_1 = \begin{pmatrix} 1 & 0 \\ 0 & -1 \end{pmatrix}, \quad \sigma_2 = \begin{pmatrix} 0 & 1 \\ 1 & 0 \end{pmatrix}, \quad \sigma_3 = \begin{pmatrix} 0 & -i \\ i & 0 \end{pmatrix}, \tag{1.6}$$

which form a complete and orthogonal basis for the 2×2 Hermitian matrices. It can be proven [19] that the eigenvalues of Γ_{2D} are non-negative and therefore $S_0^2 \geq S_1^2 + S_2^2 + S_3^2$. If the normalized Stokes parameters $s_n = S_n/S_0$ are used, the previous inequality reduces to $s_1^2 + s_2^2 + s_3^2 \leq 1$. This condition constrains the domain of $\{s_n\}$ to the interior and surface of a sphere known as the *Poincaré Sphere*. Points over the surface are related to *fully polarized* states, and points at the interior of the sphere correspond to *partially polarized* or *unpolarized* states. The norm of the normalized Stokes vector is a measure of the degree of polarization, $P_{2D} = \sqrt{s_1^2 + s_2^2 + s_3^2}$ and it can be interpreted as a measure of the fraction of the optical power that is fully polarized.

The azimuthal and polar angles on the Poincaré sphere can be computed by using

$$\phi = \text{atan}(s_2, s_1), \tag{1.7}$$

$$\theta = \arcsin(s_3). \tag{1.8}$$

These angles are associated with the ellipse's orientation and ellipticity, as illustrated in Fig. 2.1. The semi-major and semi-minor axes of the normalized polarization ellipses are

$$a = \left[\tan\left(\frac{\theta}{2}\right) + 1\right]^{-1/2}, \tag{1.9}$$

$$b = \sqrt{1 - a^2}. \tag{1.10}$$

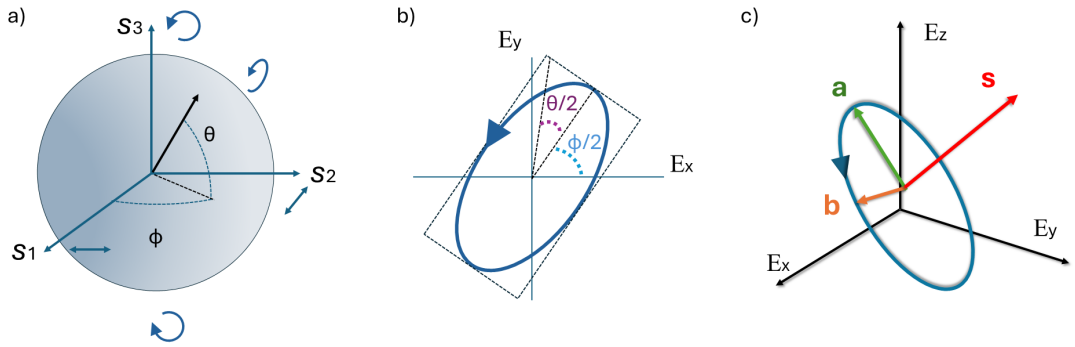

Figure 1.1.: Poincaré sphere and polarization ellipse. a) Every point on the sphere is related to a local field polarization state. Fully polarized states correspond to points over the sphere surface. The equator corresponds to linear polarization and the north/south poles to circular left/right polarization. b) The orientation and ellipticity of the physical polarization ellipse is a function of the spherical angles $\phi \in [0,\pi]$ and $\theta \in [-\pi/2,\pi/2]$, the handedness is encoded in the sign of θ. c) 3D oriented ellipse of polarization, where the major/minor axis are shown in green/orange, and the spin vector is shown in red.

There are other elegant features related to the Stokes formalism and the Poincaré sphere that can be found in [1, 19, 20]; for now, let us briefly discuss how these parameters can be measured.

From Eq. (2.1) it is clear that S_0 is the field's total intensity, which can be directly measured with cameras or single photo-detectors; S_1 and S_2 can be computed from the measurements of four linear polarization projections accessible by placing a linear polarizer in front of the photodetector at different orientations (**x**,**y**, **p**,**m**), and S_3 can be calculated from the measurement of two orthogonal circular polarization projections, measurable with a combination of quarter-wave plate (whose fast axis is oriented along **p m**), followed by a horizontal linear polarizer.

In the last decades, there has been intense research around the control and measurement of complex paraxial polarization structures [21]. In particular, the so-called Poincaré beams are light fields that exhibit all possible polarization states [22]. These fields can be understood as a map of every point over the Poincaré sphere to the real space through the stereographic projection. In Chapter 2 we explain how special maps of the Poincaré sphere to the real plane create periodic *skyrmionic* fields that can be experimentally generated.

1.3. 3D Polarization.

As mentioned earlier, evanescent fields, tightly focused beams, or light fields close to their sources can have non-negligible components in the three directions of space.

Similar to the 2D case, it is possible to define the polarization matrix as:

$$\Gamma_{3D} = \langle \mathbf{E}(x,y,z,t)\mathbf{E}(x,y,z,t)^{\dagger} \rangle = \begin{pmatrix} \langle E_x E_x^* \rangle & \langle E_x E_y^* \rangle & \langle E_x E_z^* \rangle \\ \langle E_y E_x^* \rangle & \langle E_y E_y^* \rangle & \langle E_y E_z^* \rangle \\ \langle E_z E_x^* \rangle & \langle E_z E_y^* \rangle & \langle E_z E_z^* \rangle \end{pmatrix}. \tag{1.11}$$

This is also a Hermitian non-negative definite matrix. Equivalently to the paraxial case, we can omit time averaging for monochromatic fields and write

$$\Gamma_{3D} = \begin{pmatrix} E_x E_x^* & E_x E_y^* & E_x E_z^* \\ E_y E_x^* & E_y E_y^* & E_y E_z^* \\ E_z E_x^* & E_z E_y^* & E_z E_z^* \end{pmatrix}. \tag{1.12}$$

Again, the complex electric field $\mathbf{E} = (E_x, E_y, E_z)$ is then the only eigenvector with nonzero eigenvalue of this matrix, with the total intensity $I = |E_x|^2 + |E_y|^2 + |E_z|^2$ as the corresponding eigenvalue. In the general case, Γ_{3D} can be written in terms of the so-called generalized Stokes-Gell-Mann parameters

$$\Gamma_{3D} = \frac{1}{2}\begin{pmatrix} \frac{2}{3}S_0 + S_{11} + \frac{S_{12}}{\sqrt{3}} & S_{23} - iS_{33} & S_{22} + iS_{32} \\ S_{23} + iS_{33} & \frac{2}{3}S_0 - S_{11} + \frac{S_{12}}{\sqrt{3}} & S_{21} - iS_{31} \\ S_{22} - iS_{32} & S_{21} + iS_{31} & \frac{2}{3}S_0 - 2\frac{S_{12}}{\sqrt{3}} \end{pmatrix}, \tag{1.13}$$

with

$$\begin{aligned} &S_0 = \mathrm{Tr}[\Gamma_{3D}] = \langle E_x E_x^* \rangle + \langle E_y E_y^* \rangle + \langle E_z E_z^* \rangle, \\ &S_{11} = \langle E_x E_x^* \rangle - \langle E_y E_y^* \rangle, \qquad S_{12} = \frac{\langle E_x E_x^* \rangle + \langle E_y E_y^* \rangle - 2\langle E_z E_z^* \rangle}{\sqrt{3}}, \\ &S_{21} = 2\mathrm{Re}\langle E_z E_y^* \rangle, \qquad S_{22} = 2\mathrm{Re}\langle E_x E_z^* \rangle, \qquad S_{23} = 2\mathrm{Re}\langle E_y E_x^* \rangle, \\ &S_{31} = 2\mathrm{Im}\langle E_z E_y^* \rangle, \qquad S_{32} = 2\mathrm{Im}\langle E_x E_z^* \rangle, \qquad S_{33} = 2\mathrm{Im}\langle E_y E_x^* \rangle, \end{aligned} \tag{1.14}$$

This parametrization results from decomposing Γ_{3D} in terms of the 3×3 identity matrix and the Gell-Mann matrices:

$$\Gamma_{3D} = \frac{1}{3}S_0\Theta_0 + \frac{1}{2}\sum_{n,m} S_{n,m}\Theta_{n,m}, \tag{1.15}$$

with

$$\Theta_0 = \begin{pmatrix} 1 & 0 & 0 \\ 0 & 1 & 0 \\ 0 & 0 & 1 \end{pmatrix}, \quad \Theta_{11} = \begin{pmatrix} 1 & 0 & 0 \\ 0 & -1 & 0 \\ 0 & 0 & 0 \end{pmatrix}, \quad \Theta_{12} = \frac{1}{\sqrt{3}} \begin{pmatrix} 1 & 0 & 0 \\ 0 & 1 & 0 \\ 0 & 0 & -2 \end{pmatrix},$$
$$\Theta_{21} = \begin{pmatrix} 0 & 0 & 0 \\ 0 & 0 & 1 \\ 0 & 1 & 0 \end{pmatrix}, \quad \Theta_{22} = \begin{pmatrix} 0 & 0 & 1 \\ 0 & 0 & 0 \\ 1 & 0 & 0 \end{pmatrix}, \quad \Theta_{23} = \begin{pmatrix} 0 & 1 & 0 \\ 1 & 0 & 0 \\ 0 & 0 & 0 \end{pmatrix}, \tag{1.16}$$
$$\Theta_{31} = \begin{pmatrix} 0 & 0 & 0 \\ 0 & 0 & -i \\ 0 & i & 0 \end{pmatrix}, \quad \Theta_{32} = \begin{pmatrix} 0 & 0 & i \\ 0 & 0 & 0 \\ -i & 0 & 0 \end{pmatrix}, \quad \Theta_{33} = \begin{pmatrix} 0 & -i & 0 \\ i & 0 & 0 \\ 0 & 0 & 0 \end{pmatrix},$$

which form an orthogonal basis for the Hermitian 3×3 matrices.

There is a special case of particular interest where $S_{31} = S_{32} = S_{33} = 0$. If this condition is valid in the general case of non-monochromatic fields, the three eigenvectors of Γ_{3D} determine the axes of an ellipsoid volume that determines the average region explored by the field. We can associate the eigenvector related to the largest eigenvalue as the main direction of the field oscillations [23]. The unified description and notation used in this section to explain paraxial and nonparaxial polarization follow conventions proposed recently [1], some other works have discussed nonparaxial fields and the interpretation of the quantities here presented [24, 25].

In the following section and throughout the thesis we discuss the process of measuring the Stokes-Gell-Mann parameters. For the moment, let us discuss how to retrieve the physical path described by the field.

As mentioned earlier, if we restrict ourselves to monochromatic fields, $\mathbf{E}(x, y, z, t) = \mathbf{E}(x, y, z)e^{-i\omega t}$, the only eigenvector of Γ_{3D} with non-zero eigenvalue is $\mathbf{E}(x, y, z)$. However, in experimental situations Γ_{3D} could have more than one eigenvalue different from zero due to the presence of noise, bias in the measurement system, or other experimental imperfections. In these situations, we can take into account only the eigenvector associated with the largest eigenvalue of Γ_{3D} as the *expected* field $\hat{\mathbf{E}}$. We can decompose this 3D vector as [1]

$$\hat{\mathbf{E}}(x, y, z) = Ae^{i\Phi}(\mathbf{a} + i\mathbf{b}), \tag{1.17}$$

where $A = |\hat{\mathbf{E}}(x, y, z)|$ is the local field amplitude, $\Phi = \frac{1}{2}\arg(\hat{\mathbf{E}} \cdot \hat{\mathbf{E}})$ is a global phase and $\mathbf{a}$ and $\mathbf{b}$ are the ellipse's major and minor semi-axis vectors, which are real and mutually orthogonal. Whereas A and Φ are directly computed from $\hat{\mathbf{E}}(x, y, z)$, $\mathbf{a}$ and $\mathbf{b}$ are calculated from the normalized field $\mathbf{f}=\frac{\hat{\mathbf{E}}}{A}e^{-i\Phi}$ as $\mathbf{a}$=Re($\mathbf{f}$), $\mathbf{b}$=Im($\mathbf{f}$). For a fully polarized field, the normalized *spin density* is defined as

$$\mathbf{s} = \frac{\mathrm{Im}(\hat{\mathbf{E}}^* \times \hat{\mathbf{E}})}{|\hat{\mathbf{E}}|^2} = 2\mathbf{a} \times \mathbf{b}. \tag{1.18}$$

The 3D polarization ellipse and the vectors $\mathbf{a}$, $\mathbf{b}$ and $\mathbf{s}$ are illustrated in Fig. 1.1c.

The Stokes-Gell-Mann parameters can be normalized with respect to S_0, which equals the total field intensity, as $s_{nm} = (\sqrt{3}/2)S_{nm}/S_0$. Similarly to the paraxial case, the 3D degree of polarization can be defined as the norm of the vector that has as components the eight normalized Stokes-Gell-Mann parameters, $P_{3D} = \sqrt{\sum_{nm} s_{nm}^2} \leq 1$, although this is not the only proposed definition [26–28]. Unlike the paraxial regime where the normalized Stokes parameters are constrained inside and at the surface of the Poincaré sphere, the domain of s_{nm} is not delimited by a hypersphere [1].

So far, we have discussed the physical quantities of interest and how to compute the local field $\mathbf{E}$ from Γ_{3D}. In the next section, we discuss some proposed methods to experimentally test fields at nanoscales, and we briefly introduce our proposal to perform nonparaxial polarimetry in a single shot and its connection with the measurement of 3D oriented dipolar sources.

1.4. Experimental methods in the nonparaxial regime.

The direct measurement of nonparaxial optical fields has been an active research area during the last two decades [21]. In the paraxial regime, simple setups based on intensity-only or interferometric configurations allow complete measurement of the complex vectorial nature of paraxial light with simple data postprocessing [29]. For nonparaxial fields, the full characterization of light at nanoscales still depends on complex experimental setups involving scanning nanotips, fluorescent layers, or the far-field analysis of the signal generated by nanoscatterers. In Fig. 1.2 we illustrate general examples of methods used to measure complex nonparaxial fields at nanoscales.

Early experiments [2] in nonparaxial fields illustrated the presence of a longitudinal field component by exciting fluorescent molecules on a coverslip and measuring in the image plane of a high NA microscope objective. Different spatial distributions on the molecules' intensity were associated with various 3D orientations that could only be excited by the presence of a field component parallel to that direction, as shown in Fig. 1.2a.

Quantitative measurements of the field's amplitude and phase are nowadays possible by using near-field scanning tips combined with interferometric configurations. These methods are particularly suitable for testing evanescent fields with subwavelength structures such as skyrmion fields, as illustrated in Fig. 1.2b. During the last decade, the use of nanoscatterers was proposed to perform quantitative measurements of nonparaxial fields. A single particle is deposited on a coverslip mounted on a piezo stage that allows the measurement of the field across one plane. The signal is collected by a microscope objective and measurements are performed at the exit of the objective. With this configuration, it is possible to measure subwavelength structures of polarization such as Möbius strips [3], as shown in Fig. 1.2c. Similar

configurations have been used to measure other nonparaxial structured fields. Let us discuss these techniques in detail in the next section.

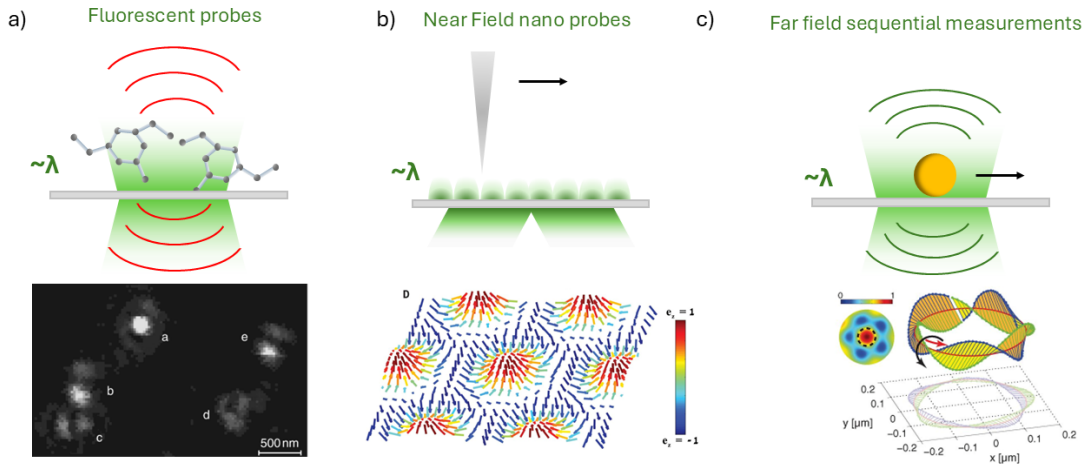

Figure 1.2.: Illustration of methods for nonparaxial field characterization. a) The first experiments probing nonparaxial fields used fluorescent molecules to test the longitudinal field components [2]. More recently, fluorescent layers were used to test more complex nonparaxial fields [16]. In both cases the signal is collected by a high NA objective and measured by a camera placed at the image plane; in Ref. [2] the objective was placed in reflection mode whereas in Ref. [16] it was in transmission mode. (Adapted from [2]). b) Nano tips were used to scan evanescent fields and reconstruct the polarization distribution in 2D and 3D [30, 31]. This configuration was used to test optical skyrmions where the electric field explores all 3D orientations. (Adapted from [31]). c) A scanning nanosphere was used to test nonparaxial fields by measuring the interference between the far field of the incoming field and the signal from the particle. The sequential measurements were fitted to a model based on Mie scattering. This configuration allowed measuring Möbius strips of the electric field with subwavelength resolution [3].

1.4.1. Measuring nonparaxial fields with nanospheres

The use of nanoparticles as field probes presents several advantages over scanning nanotips. In particular, it represents a more flexible approach that could be implemented in commercial optical microscopes. Bauer *et al.* [4] proposed a method, illustrated in Fig. 1.3a, where a high NA objective is used to generate a nonparaxial field tested by a nanogold sphere. The interference pattern between the incoming beam and the scattered field is measured at the back focal plane of a second objective. Different regions of the pupil plane are integrated to create a set of data that depends on the sphere's position. By fitting these data to a Mie scattering-based model, the authors were able to reconstruct the amplitude and phase of tightly focused beams across areas of 1 μm^2 while resolving sub-wavelength structures.

In other methods, shown in Fig. 1.3b-c, the authors performed paraxial Stokes polarimetry to the collimated signal scattered by the nanospheres. Eismann *et al.* [32] placed a particle over a prism used to generate an evanescent field. The signal collected by a high NA objective was analyzed in the Fourier plane with a standard polarimeter and compared with simulations. In similar work, Rodriguez-Herrera *et al.* [5] probed the spin-to-orbital angular momentum conversion of light by strongly focusing a beam with a high NA lens. The same lens was then used to collect the signal scattered by a nanosphere. They performed paraxial Stokes polarimetry to the collected signal at the pupil plane. In these works, the particle localization information is lost since the measurements are performed at the pupil plane. Nevertheless, the authors can reconstruct a field distribution by correlating the position of the particle to the displacements of the piezo stage. Another feature that these methods have in common is that the nanoprobe can be considered as a dipole scatterer with dipole moment $\hat{\boldsymbol{\mu}}$. The problem of measuring nonparaxial fields now becomes a problem of efficiently measuring the induced dipole $\hat{\boldsymbol{\mu}}$.

When using a dipole probe care should be taken to ensure that the measurement system is sensitive to all possible dipole configurations, which is not necessarily true for simple setups consisting of a high NA objective and camera, as discussed in Chapter 3. The problem of measuring dipole emitters (i.e. measuring the dipole moment vector $\hat{\boldsymbol{\mu}}$) and localizing them in 3D has been studied extensively in modern single-molecule microscopy techniques. In the next section, we explain some of these methods and their relation to nonparaxial polarimetry.

1.4.2. Measuring 3D oriented molecules.

Single-Molecule Localization Microscopy (SMLM) is one family of super-resolution optical microscopy methods that have been proposed in the last two decades to observe objects with subwavelength structures [6]. These techniques have surpassed the resolution limit by measuring the individual positions of single molecules (dipole emitters) and then reconstructing the target object by accumulating all of the individual positions. In particular, techniques such as Photoactivated Localization Microscopy (PALM) [7], Stochastic Optical Reconstruction Microscopy (STORM) [8], or Point Accumulation for Imaging in Nanoscale Topography (PAINT) [9] are based on the measurement of the centroid of the intensity distribution associated with single fluorophores. The difference between these techniques is the physical/chemical mechanism that allows the time sparsity of the detections, but their reconstruction principle is the same: a camera is placed at the plane conjugate to the sample plane. It is assumed that the measured intensity distribution for each flurophore, referred to as the Point Spread Function (PSF), is described by a 2D Gaussian distribution centered at (x_{PSF}, y_{PSF}) with standard deviation σ_{PSF}. A superresolved image can be obtained by plotting a Gaussian distribution centered at (x_{PSF}, y_{PSF}) with a standard deviation equal to the uncertainty of the estimated center, given by $\sigma_{SMLM} \approx \sigma_{PSF}/\sqrt{N}$ with N the total number of photons contained in the PSF [6].

The assumption that the PSF can be modeled by a 2D Guassian distribution valid as

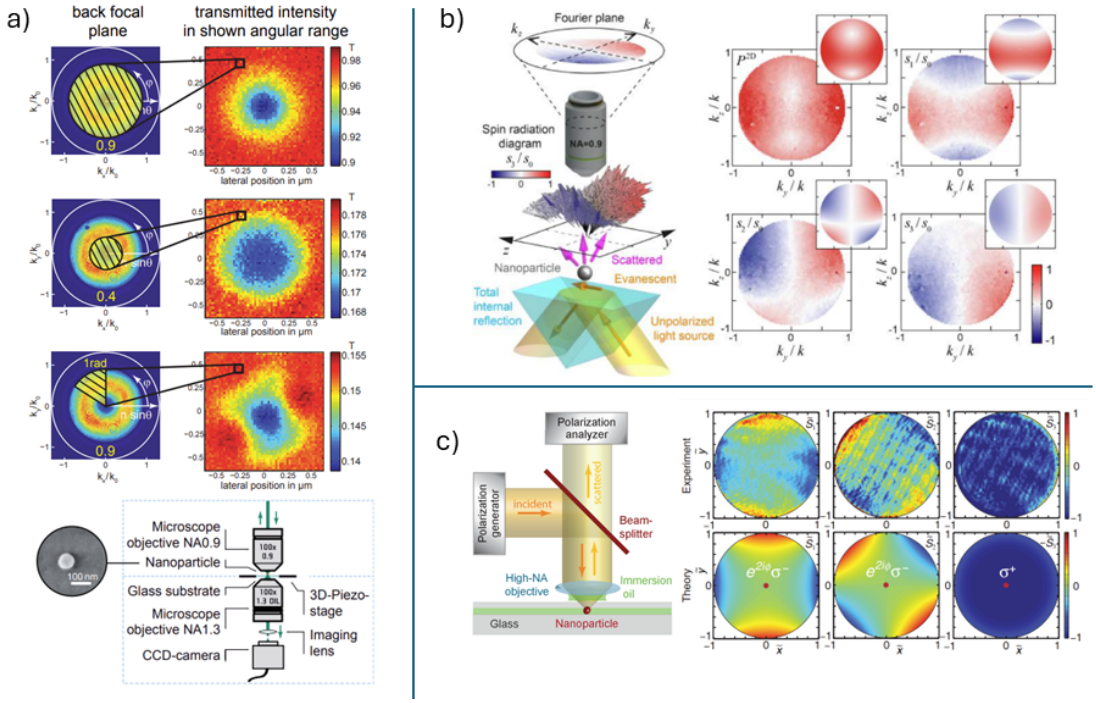

Figure 1.3.: Setups based on measurements at the back-focal plane to investigate nonparaxial fields. a) Two high NA microscope objectives are used to generate and measure tightly focused light fields. A single imaging lens is used to project the field at the back-focal plane onto a camera. Different regions of the pupil plane are analyzed to generate a spatially-dependent array of data that is fitted to a vectorial model. (Adapted from [4]). b) By performing paraxial polarimetry to the collimated signal at the back focal plane, it is possible to measure evanescent fields and c) complex focused beams. (Adapted from [5, 32]).

long as the fluorophore explores multiple orientations faster than the integration time of the camera (i.e. it behaves as a depolarized emitter). When the fluorophore mobility is constrained to an average direction a more complex PSF can be observed [10–13]. However, measuring the actual 3D orientation of the emitter is not trivial; even when the emitter has a fixed orientation the complete 3D orientation information is not accessible by only measuring the natural PSF in a simple configuration consisting of an objective, a tube lens and a camera. For a molecule with a fixed 3D orientation, its dipole moment vector is given by $\hat{\boldsymbol{\mu}} = (\sin\eta\cos\xi, \sin\eta\sin\xi, \cos\eta)$, where (η, ξ) are the polar and azimuthal angles respectively. However, molecules are typically not static, they can wobble in time, faster than the integration time of the detectors. In situations where the molecule wobbles isotropically around a fixed direction, it describes a distribution whose aperture angle δ is a measure of its wobbling. This quantity is related to the degree of polarization P of nonparaxial fields.

In recent years, there has been growing interest in developing Single Molecule Orientation and Localization Microscopy (SMOLM) methods to extract the orientation, wobbling and 3D position of fluorophores from their PSF. This represents at least six parameters to be determined (and more if the wobbling is not symmetric around the main orientation axis). In Fig. 1.4, we present a summary of various methods to simultaneously measure molecular orientation, wobbling and position in imaging configurations. It is possible to classify these methods into two general families: PSF engineering and ratiometric measurements [14, 23]. In PSF engineering an object that modulates phase and/or polarization is placed at the pupil plane of the microscope, and it is sometimes followed by the separation of the signal into several polarization components. The resulting PSF can be significantly and unambiguously dependent on the emission orientation and localization parameters. We discuss this dependence in Chapter 3. In ratiometric schemes the signal is separated into several channels either by polarization or spatial filters, the relative imbalance in the energy in the channels is associated with the orientation and/or spatial parameters.

1.4.3. Stokes polarimetric imaging at nanoscales.

The approach for performing nonparaxial polarimetry proposed in this thesis takes inspiration from PSF engineering techniques used in SMOLM where linear dipoles are measured to retrieve molecular 3D orientation, wobbling and position. We propose to use an array of dipole scatterers to test nonparaxial fields at multiple positions in a single shot. This array is placed close to the focal plane of a high NA objective in a standard reflection configuration mode. The system is based on the circular polarization separation of the scattered signal and its measurement in an imaging configuration, which allows for decoupling the dipole 2D spatial information. The use of dipole scatterers is not accidental: the induced dipole $\hat{\boldsymbol{\mu}}$ on a Rayleigh scatterer is proportional to the external field $\mathbf{E}_{Ext}$. Hence, the problem of measuring the local polarization of $\mathbf{E}_{Ext}$ is reduced to that of measuring $\hat{\boldsymbol{\mu}}$ from the signal radiated by the scatterer.

We propose a framework based on the Stokes-Gell-Mann parameters to study situ-

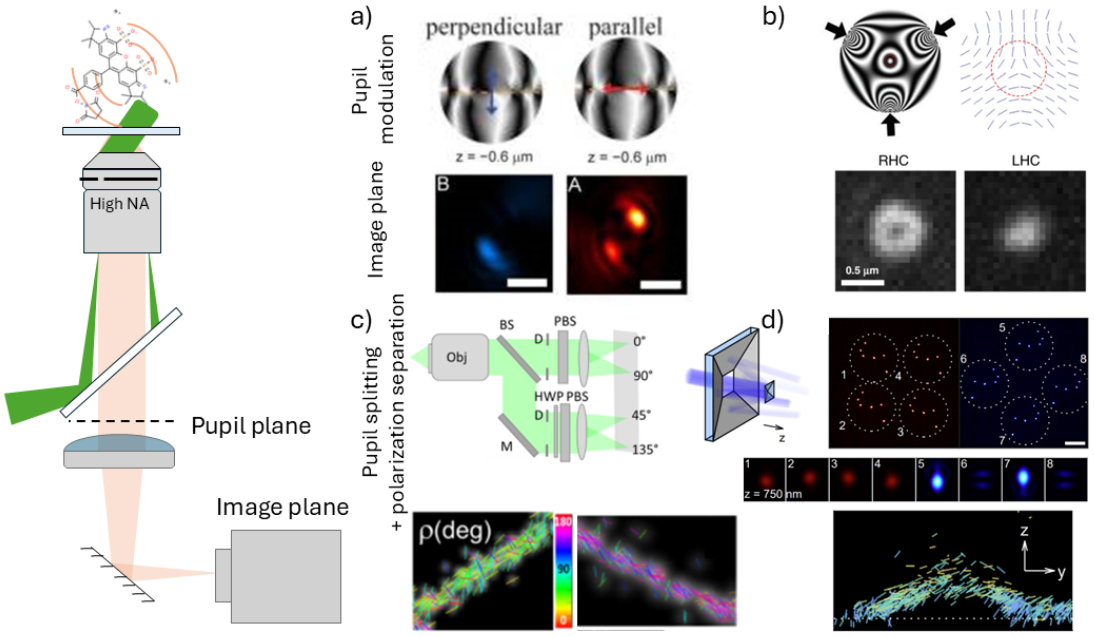

Figure 1.4.: General illustration of SMOLM methods. A standard high NA objective in reflection configuration is used to image fluorescent molecules. The signal can be modulated in phase or polarization by transparent birefringent elements, phase plates or spatial light modulators. Typically, it is necessary to split the signal into two polarized channels. From the combined information from both channels it is possible to recover the 3D orientation (and in some cases, localization) of the fluorophores. a) *Double helix* phase modulation mask applied to the horizontal and vertical components of the signal and the corresponding PSFs. (Adapted from [12].) b) Modulation by a *stressed engineered optic*, which is a glass window subject to forces with trigonal symmetry at its edges, and examples of characteristics PSFs. (Adapted from [18].) c) A ratiometric method where the signal is split into four polarization channels, allowing to measure large amounts of fluorophores in complex and dense biological systems while extracting their orientation information. Here, the sticks represent the fluorophore orientation projection in the sample plane, the color represents the azimuthal angle, (adapted from [18]). d) Illustration of a recently proposed method to measure 3D position and 3D orientation of molecules based on the separation in eight different polarization channels. The signal is divided in four regions at the pupil plane and then separated into the horizontal and vertical polarization components. Similarly, the sticks represent the 3D orientation and the color indicates the polar angle. Note that the $z-y$ plane is shown in the last figure. (Adapted from [33]).

ations where elliptical dipoles are measured with a high NA microscope to account for elliptically polarized light. We show that, when the emitter's 3D position is known, the complete information of dipole sources can be obtained by simply separating the signal into its circular polarization components. We exploit the mathematical properties of the Stokes-Gell-Mann parameters to describe the measurement system and to analyse the data.

In Chapter 2, we present the generation of structures of polarization in paraxial fields using special maps of the Poincaré sphere onto real space. In Chapter 3, we discuss the measurement process of optical dipoles by a high NA microscope in terms of the Stokes-Gell-Mann formalism and comment on the capabilities of previous methods to measure elliptical dipoles. In Chapter 4 we describe a technique to completely characterize dipole sources based on the separation of the signal into its circular polarization components. We present experimental results in nonparaxial polarimetry by using an array of gold nanospheres as field probes in Chapter 5. Finally, in Chapter 6, we explore the use of fluorescent 3D-oriented molecular dipoles in the context of this new circular projection scheme. We present results in molecular orientation microscopy and the potential extension to SMOLM are discussed.

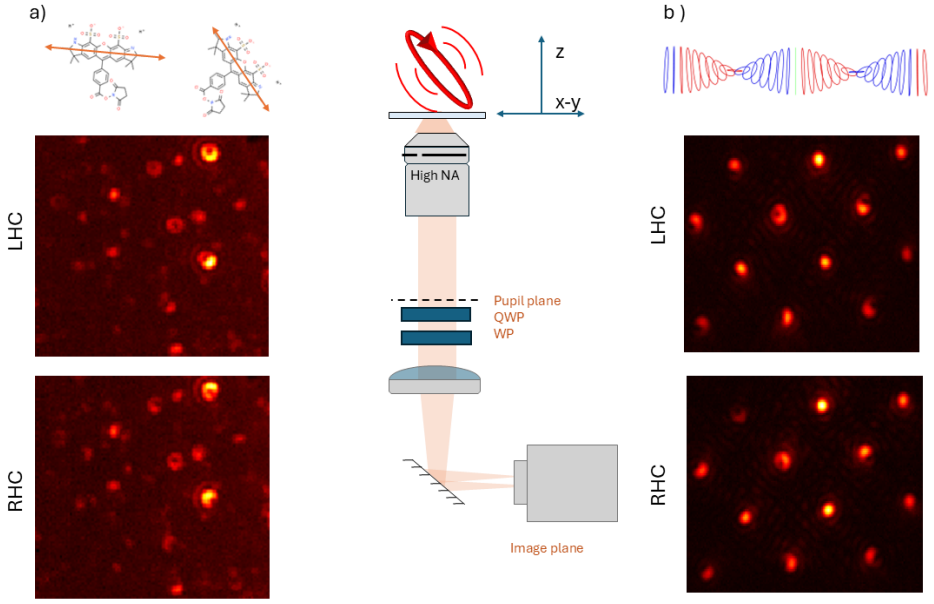

Figure 1.5.: Illustration of the thesis project. A microscope configuration capable of measuring $\hat{\boldsymbol{\mu}}$ can be compatible with (a) single molecule orientation microscopy or (b) nonparaxial polarimetry. The proposed setup is based on the separation of the signal into its right- and left-handed circular polarization components (RHC and LHC, respectively) by placing a quarter wave plate and a Wollaston prism in the Fourier plane. With this configuration two replicas of the same field of view are measured in the same camera. In (a) and (b) we illustrate typical experimental PSFs in fluorescence and scattering configurations. Note the similarity of the PSFs regardless of their source's nature.

2. Generation and measurement of spatially variant 2D polarized fields.

Sommaire

2.1. Introduction: Structured light. 35
2.2. Structuring 2D polarized fields. 36
2.3. Measuring 2D polarized fields. 38
2.4. Special case of 2D beams: Skyrmion and Meron lattices. 39
2.5. Periodic skyrmions via cartographic maps. 41
2.6. Propagation invariant meron lattices. 45
2.7. Final remarks 47

2.1. Introduction: Structured light.

Light is an electromagnetic wave with different degrees of freedom: amplitude, phase, polarization, and frequency. In recent decades, a great theoretical and experimental effort has been devoted to developing new ways to manipulate and control monochromatic light beams propagating in free space [21, 34] for applications in bio-imaging, astronomy, quantum and classical communication, and micromanipulation, to name a few examples. Nowadays, it is common to use metasurfaces, spatial light modulators based on liquid crystal technology, digital micromirror devices or transparent optics to perform spatially-dependent modulation of the amplitude, phase and polarization of monochromatic beams. All this progress in light control has allowed the implementation of exotic light structures such as propagation invariant beams [35], accelerating beams [36], optical knots[37], optical Hopfions [38], optical skyrmions [39], or Möbius strips of light [3]. In this chapter, we study vector fields that result from mapping the Poincaré sphere to the physical space. As a consequence, these beams exhibit all possible polarization ellipse shapes. Depending on the mathematical properties of the mapping between the sphere and the space we refer to those fields as skyrmions or merons. We describe the numerical and experimental methods behind their generation and measurement. This work was done in collaboration with David Marco Castillo, who developed the theoretical formulation. It is reported in two published articles [40, 41].

2.2. Structuring 2D polarized fields.

Paraxial or 2D monochromatic fields have only two significant vectorial components oscillating in the plane (x, y) transverse to the propagation direction z. The elliptical trajectory described by the field is given by $\mathrm{Re}[\mathbf{E}(x,y)e^{-i\omega t}]$, where ω is the angular frequency and $\mathbf{E}(x, y)$ is the complex field. This complex field can be decomposed either in the linear polarization basis as $\mathbf{E}(x,y) = \mathrm{E}_x(x,y)\mathbf{x} + \mathrm{E}_y(x,y)\mathbf{y}$, where $\mathbf{x}$ ($\mathbf{y}$) is the unitary vector along the x (y) axis, or in the circular basis as $\mathbf{E}(x,y) = \mathrm{E}_l(x,y)\mathbf{l} + \mathrm{E}_r(x,y)\mathbf{r}$, where $\mathbf{l},\mathbf{r} = \frac{1}{\sqrt{2}}(\mathbf{x} \pm i\mathbf{y})$. Note that E_x, E_y, E_l and E_r are complex scalar functions defined over the plane (x, y). Any arbitrary polarization ellipse, defined by $\mathbf{E}(x, y)$, can be achieved by controlling the amplitude and phase of E_x and E_y or equivalently, E_l and E_r.

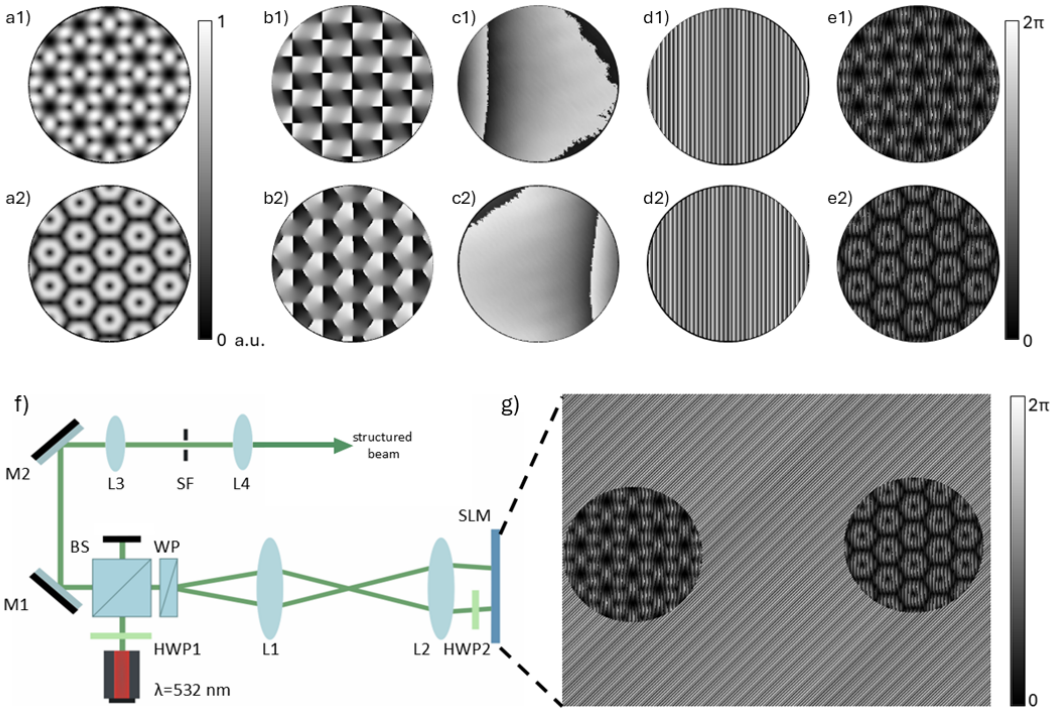

Figure 2.1.: Hologram design and setup. Example of (a1,a2) amplitude and (b1,b2) phase maps for the E_x, E_y components. (c1,c2) Corresponding correction phase Φ_C and (d1,d2) blazed phase Φ_B are used to recombine the beams and separate them from the zeroth order. (e1,e2) Final holograms are displayed on circular areas of 260 pixels in diameter on the SLM. f) Optical setup, not to scale. g) Hologram of 600×800 pixels displayed on the SLM showing the two independent areas on the SLM and an extra blazed phase that deflects the unmodulated light.

One of the most used devices to modify the amplitude and phase of monochromatic beams is the spatial light modulator (SLM) based on liquid-crystal pixels that spatially control the relative phase of the incident field. These commercial devices usually control the phase of a linear polarization component while leaving the other component

unchanged. Let us first discuss how to achieve simultaneous amplitude and phase modulation with a phase-only SLM and then how to combine this approach with a setup [42] to generate arbitrarily spatially-variant polarization distributions. Bolduc *et al.* [43] proposed a hologram algorithm to modulate both amplitude and phase with a phase-only SLM. The SLM acts as a diffraction grating, such that the zeroth diffraction order remains unmodulated whereas the first order contains the modulated part. Suppose that $A(x,y)$ and $\Phi(x,y)$ are the desired amplitude and phase to be generated by the SLM describing one linearly polarized field $E = Ae^{i\Phi}$. In that case, the displayed hologram is given by $\Psi = M\text{Mod}(F,2\pi)$ (assuming an incoming beam with constant amplitude and phase), where $M = 1 + \frac{1}{\pi}\text{sinc}^{-1}(A)$ and $F = \Phi - \pi M$ [43]. Whereas the desired amplitude is simply $A = |E|$, the final desired phase must include the correction term Φ_C (provided by the manufacturer) that accounts for phase inhomogeneities over the SLM screen and a blazed phase Φ_B that is commonly used to separate the zeroth-order from the first modulated order, namely $\Phi = \text{Mod}(\arg[E] + \Phi_B + \Phi_C, 2\pi)$ as shown in Fig. 2.1a-e,g.

Maurer *et al.* [42] proposed an interferometric setup to generate *vector beams*, in particular Laguerre- and Hermite-Gaussian beams with spatial variation of polarization as well as radially azimuthally polarized doughnut modes. The principle of this method is to divide the SLM screen into two independent regions where the two orthogonal **x**,**y** components of the field are modulated. The setup is shown in Fig. 2.1f. The orientation of the linearly polarized state of a continuous-wave (CW) laser beam with a wavelength of $\lambda = 532$ nm is controlled using a half-wave plate (HWP1) before entering a 50:50 beamsplitter (BS). The light is then reflected by the BS to a Wollaston prism (WP), which splits it into two orthogonal linearly polarized beams diverging with an angle of 1°. Subsequently, both beams undergo magnification through a telescope consisting of lenses L1 and L2 of 2 in. of diameter and with focal lengths of $f_1 = 100$ mm and $f_2 = 500$ mm, respectively. After reflecting off the SLM screen, the two components are recombined by the WP. In order to recombine the two components, a blazed phase Φ_B of opposite sign must be added to each component, as shown in Fig. 2.1d. Note that a second half-wave plate (HWP2) is placed in one of the beam paths to convert vertical polarization into horizontal polarization, as the SLM only modulates horizontal polarization. Then, upon reflection by the SLM, HWP2 restores the polarization to its original vertical state. After the WP, the beam returns to the BS, where it is directed to a second telescope comprised of the lenses L3 and L4 with focal lengths $f_3 = 300$ mm and $f_4 = 400$ mm, respectively. A spatial filter (SF) is placed at the Fourier plane of the telescope to remove spurious contributions. This last telescope is used to image the modulated field onto the camera screen.

One of the advantages of this setup is that the two orthogonal polarization components pass through the same optical elements, except for the HWP2 used to rotate the polarization of the E_y component. This makes the resulting structured beam robust to external mechanical vibrations. The angle of 1° associated with the WP was chosen to produce a smooth splitting of the beams to avoid introducing additional aberrations.

2.3. Measuring 2D polarized fields.

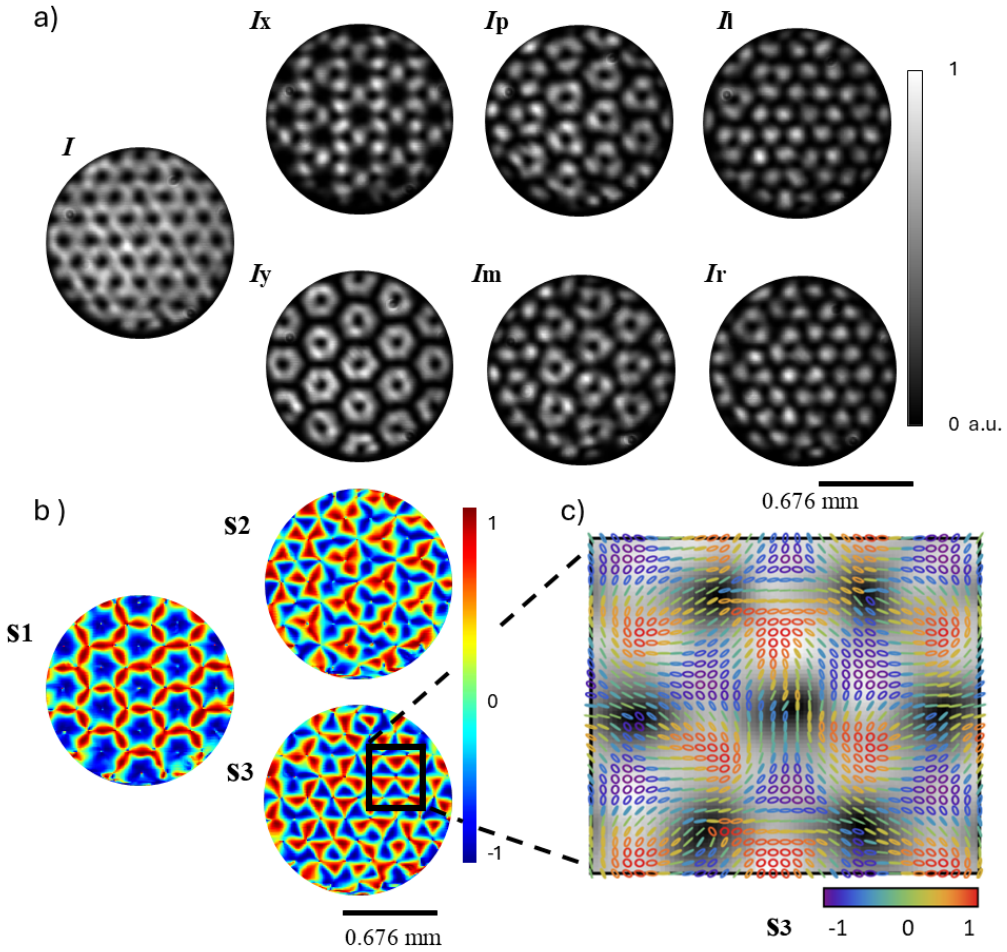

Figure 2.2.: Stokes parameter measurement. a) Example of the measured intensity of six polarization components and the total intensity of a spatially variant structured beam. b) Example of the spatially dependent normalized Stokes parameters reconstructed from the raw data shown in a) using Eq. (2.1). c) Reconstructed polarization ellipse map color according to the value of $\mathbf{s_3}$, where the extreme red and purple represent regions of circular polarization with opposite handedness .

The SLM screen is imaged onto a camera. Between L4 and the camera, a linear polarizer (LP) is placed to measure the intensity distributions of the linearly polarized components: horizontal (**x**), vertical (**y**), and oriented at ±45° from **x** (**p** and **m**, respectively). Between L4 and the LP, a quarter-wave plate (QWP) is placed with its fast axis oriented at ±45° to the LP axis oriented along the **x** direction to measure the left- and right-circular polarization components (**l** and **r**). These intensities are denoted as I_i with $i = \mathbf{x}, \mathbf{y}, \mathbf{p}, \mathbf{m}, \mathbf{l}, \mathbf{r}$. Figure 2.2a shows an example of these measurements. In addition, the total intensity, denoted by I, was measured without LP and QWP. We compute the Stokes parameters as:

$$\begin{aligned} S_0 &= I, \\ S_1 &= I_{\mathbf{x}} - I_{\mathbf{y}}, \\ S_2 &= I_{\mathbf{p}} - I_{\mathbf{m}}, \\ S_3 &= I_{\mathbf{l}} - I_{\mathbf{r}}. \end{aligned} \tag{2.1}$$

The normalized Stokes vector is given by $\mathbf{s} = \mathbf{s}'/|\mathbf{s}'|$, where $\mathbf{s}' = (S_1, S_2, S_3)/S_0$. Note that we divide the vector $\mathbf{s}'$ by its norm to avoid values smaller or even greater than 1, which are produced by the extended size of the pixels and by noise. Figure 2.2b shows an example of these measurements.

Examples of measured ellipses are shown in Fig. 2.2. Given the field's stability, we can afford to perform sequential intensity measurements by rotating the LP and placing or removing the QWP. However, in situations where the field changes faster than the sequential measurement time (typically in the order of ~ 100 ms), it is convenient to implement single-shot polarimetry techniques. In the next chapters, the need for single-shot polarimeters to study the field scattered by a single emitter will become more evident.

With the described experimental scheme we can generate and characterize polarization structures spanning areas of 1.3 mm of diameter with a resolution limited to the camera pixel size of 5.2 μm. In Chapters 4 and 5 we explain how to measure field polarization in areas of 30 μm of diameter with resolution in the order of 50 nm. This represents a difference of 2 orders of magnitude in the spatial dimension of the field structure.

2.4. Special case of 2D beams: Skyrmion and Meron lattices.

We define a 2D skyrmion (also referred to as a *baby skyrmion*) as a vector field distribution over a plane completely determined by a parameter space constrained to the surface of a 2-sphere that preserves the sign of the Jacobian map between the planar region occupied by the skyrmion and the parameter sphere. Skyrmions have been observed in different physical systems, such as magnetic materials [44], sound waves [45], superfluids [46] and optical fields [47]. In the latter case, the spherical

parameter space can be the Poincaré sphere [22], the 3D direction of the spin vector associated with elliptically polarized fields at nanoscales [48, 49] or the 3D direction of polarization for evanescent optical fields [31]. In Fig. 2.3 we illustrate representative optical skyrmions associated with different parameter spheres. When only one sphere's hemisphere is mapped onto a planar region and the sign of the Jacobian is preserved, the resultant vector field is called a *meron* texture.

The Jacobian is also related to an important quantity in skyrmion theory called the Skyrme number N_S that quantifies the number of times the unit vector $\mathbf{s} = (\sin\theta\cos\phi, \sin\theta\sin\phi, \cos\theta)$ wraps around the sphere, and the sense of wrapping determines its sign. Within a given region in the physical space σ, the Skyrme number is given by $N_S = (4\pi)^{-1}\iint_\sigma \rho_S(x,y)\,\mathrm{d}x\,\mathrm{d}y$, where

$$\rho_S(x,y) = \mathbf{s}(x,y)\cdot\left[\partial_x\mathbf{s}(x,y)\times\partial_y\mathbf{s}(x,y)\right] \tag{2.2}$$

is the Skyrme density, which is the Jacobian of the transformation.

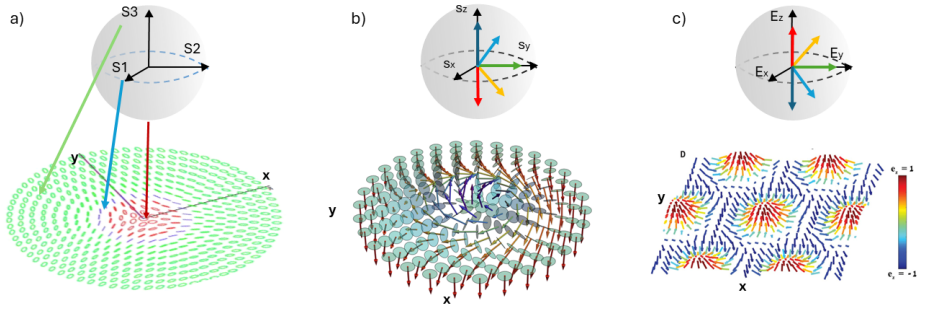

Figure 2.3.: Illustration of 2D optical skyrmions. a) A full Poincaré beam is generated when every point (S_1, S_2, S_3) on the surface of the Poincaré sphere is mapped onto the real plane (x-y) via a stereographic projection. b) When a high-order full Poincaré beam is strongly focused by a high NA objective lens, a Skyrmionic structure appears in the focal plane spanning all possible 3D directions of the spin vector (s_x, s_y, s_z) associated with the 3D oriented ellipses of polarization on the (x-y) plane. c) A skyrmionic lattice defined by all the possible 3D orientations of the instantaneous electric field (E_x, E_y, E_z) has been observed in evanescent fields. (Figure adapted from [22, 31, 48]). Note that the case shown in (a) is a paraxial field whereas (b) and (c) are nonparaxial.

In what follows, we explain the realization of 2D skyrmions and merons on paraxial fields when using the Poincaré sphere as the parameter domain. These fields have been proposed and implemented for the first time in the context of this work and the results have been published [40, 41].

2.5. Periodic skyrmions via cartographic maps.

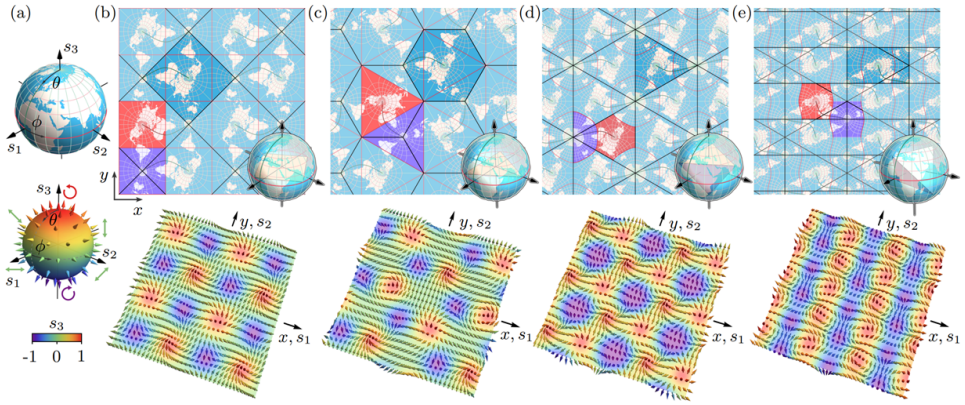

Figure 2.4.: a) The Earth and a spanned spherical parameter space (e.g. the Poincaré sphere). b)-e) Periodic skyrmionic textures resulting from conformal cartographic mappings providing regular tessellations: b) Peirce's quincuncial projection, c) Adams' world in a hexagon, d) Lee's world in a tetrahedron, and e) Wray's variation of Lee's projection. For all, the entire sphere is mapped onto regular polygons (outlined in black), one of them highlighted in darker blue in each case. Rotated versions of these tessellate the plane. The northern and southern hemispheres in each case are highlighted in red and purple, respectively. Figure modified from Ref. [41].

In Fig. 2.3a-b we present two examples of skyrmions that result from mapping once the parameter sphere to real space. Fig. 2.3c, on the other hand, shows a periodic Skyrmionic texture that results from mapping the parameter's sphere to multiple regions of the physical space. The goal of the work presented in this section is to study periodic Skyrmionic textures that preserve the sign of ρ_S. As it turns out, the periodic conformal maps (functions that locally preserve angles between lines) that describe these textures were developed in nineteenth and twentieth-century cartography, for mapping the sphere onto specific regular polygons. Physical space is then tessellated with these polygons without reflections, only translations and rotations. The spherical parameter space is then mapped as if it were the Earth, as shown in Fig. 2.4.

Let us discuss the conformal cartographic transformations and their implementation as skyrmionic textures (Fig. 2.4). We begin with Peirce's *quincuncial* projection [50], which maps the whole sphere, and also each hemisphere, onto a square. The vertices of each square tile mapping a hemisphere are equally spaced along the sphere's equator, as illustrated in Fig. 2.4b. The map is conformal everywhere except at these four singular points. The second mapping is Adams' *world in a hexagon projection* [51], which maps the sphere onto a regular hexagon and each hemisphere onto an equilateral triangle. This map exhibits singular points at the vertices of each triangular tile that spans a hemisphere. These singular points are again equally spaced along the equator, as depicted in Fig. 2.4c. Finally, we explore a projection where the entire

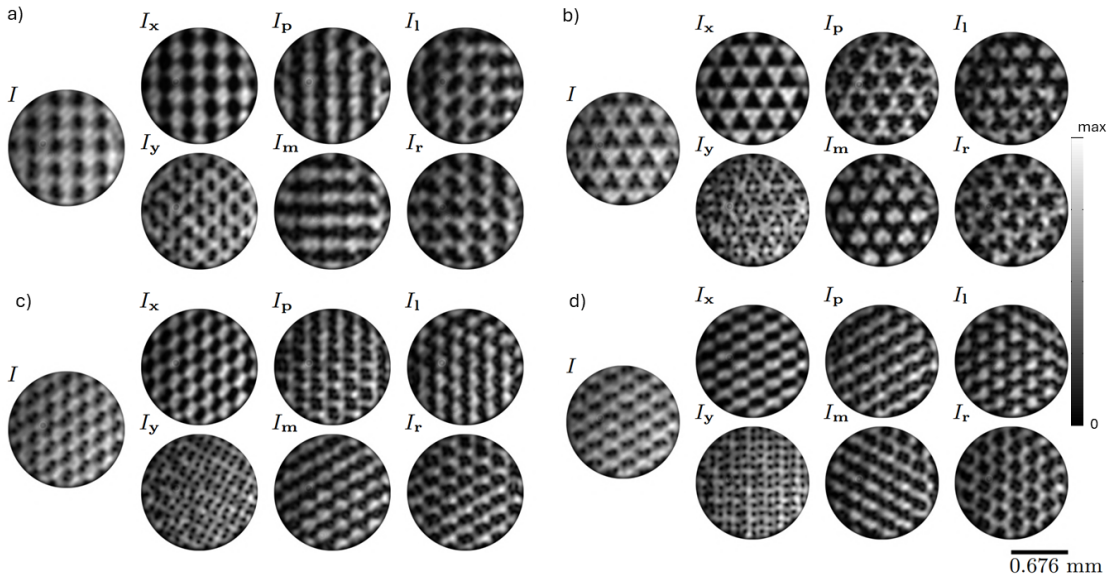

Figure 2.5.: Experimental total intensity I, linear (**x**,**y**,**p**,**m**) and circular polarization (**l**,**r**) components, of (a) Perce's projection, b) Adams's world in a hexagon, c) Lee's world, and d) Wray's projection.

sphere is mapped onto an equilateral triangle, known as Lee's *world in a tetrahedron* projection [52]. Here, the sphere is divided into four equal spherical equilateral triangles, each of which is subsequently projected onto the corresponding face of a regular tetrahedron. Unfolding the tetrahedron yields an equilateral triangle that tessellates the plane with rotated copies of itself. As shown in Fig. 2.4d, one of the tetrahedron's vertices is placed at the south pole. Upon the unfolding of the tetrahedron, the vertices of the resulting equilateral triangle map precisely the south pole. Wray proposed a modified version of Lee's mapping, depicted in Fig 2.4e., that offers a more democratic representation for the poles [53]. It is achieved through a rotation so that each pole is positioned at the midpoints of two opposing edges of the tetrahedron. In contrast to Lee's original projection, Wray's transformation results in the equator forming not closed loops but meandering lines. Upon unfolding the tetrahedron, the resulting triangle can be rearranged into a rectangle (with aspect ratio $\sqrt{3}:1$), yielding a tessellation composed of rectangles. In both versions of Lee's projection (Figs. 2.4d-e, the singular points are placed at the vertices of the tetrahedron.

Mathematically, the realization of these maps involves the sequential concatenation of two conformal transformations: a planar map defined by an analytic function denoted as $w(z)$, where $z = x + iy$ (x and y representing the Cartesian coordinates in physical space), and a stereographic projection from the north pole. These operations result in a map from the plane to the azimuthal and polar coordinates on the sphere as $\phi = \arg[w(z)]$ and $\theta = 2\arctan|w(z)|$, respectively. The 3D Cartesian coordinates in the ambient space of the sphere are $s_1 = \sin\theta\cos\phi$, $s_2 = \sin\theta\sin\phi$ and $s_3 = \cos\theta$.

The Skyrme density can be expressed as $\rho_S = \rho_{SP}\rho_w$, where $\rho_{SP} = 4(1+|w(z)|^2)^{-2}$ is

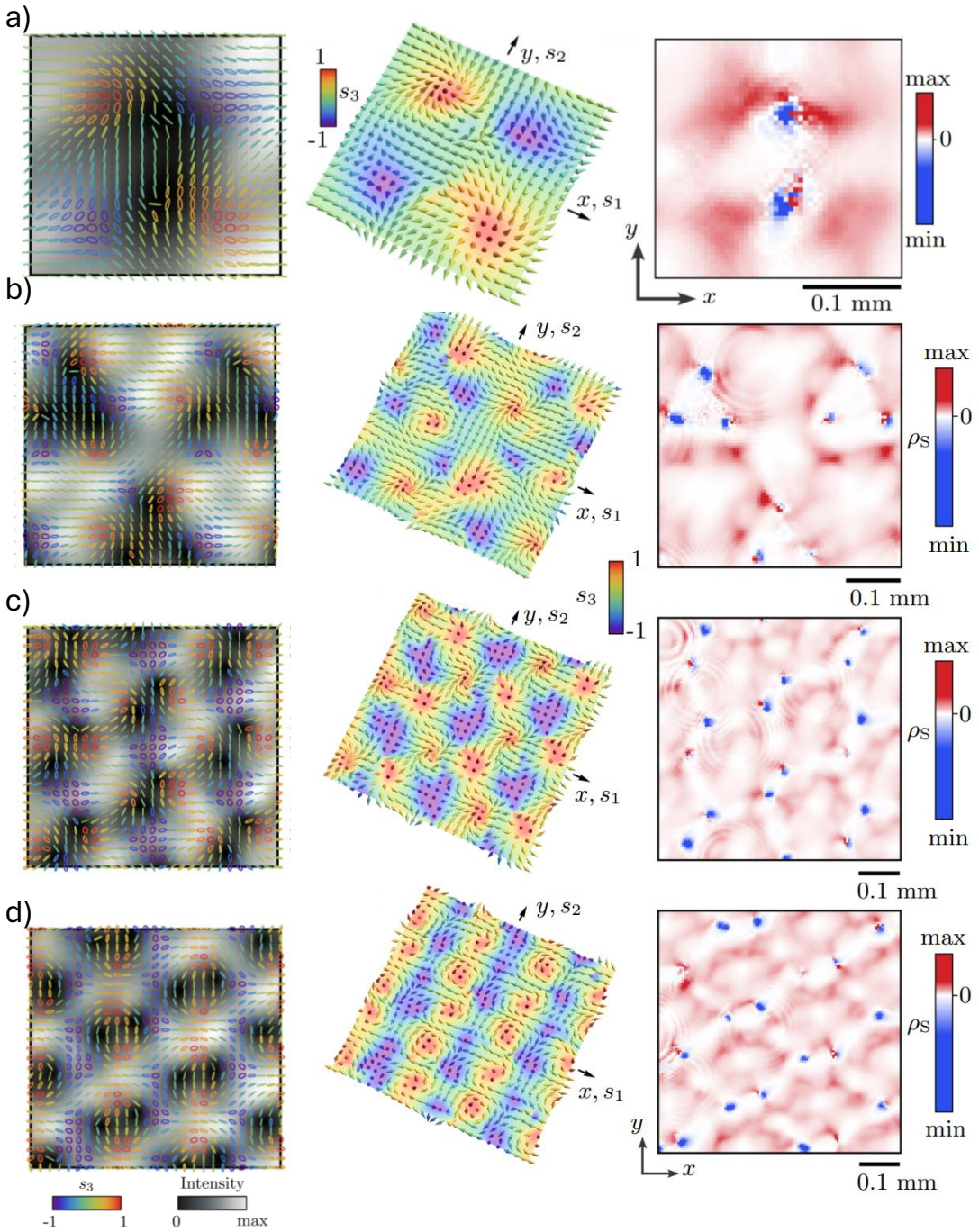

Figure 2.6.: Experimentally measured polarization ellipses, skyrmion textures and Skyrme density, corresponding to: a) Perce's projection, b) Adams's world in a hexagon, c) Lee's world and d) Wray's projection.

the Jacobian of the stereographic projection, and $\rho_w = [\partial_x \mathrm{Re}(w(z))]^2 + \left[\partial_y \mathrm{Re}(w(z))\right]^2$ is the Jacobian of the transformation $w(z)$. The explicit expressions for $w(z)$ are in the Appendix A1.

We now discuss how to implement these skyrmionic structures in the distribution of polarization for a monochromatic optical beam of frequency ω. Recall that the transverse electric field at any point (x, y) and time t is given by $E_0 = \mathrm{Re}\left[\mathbf{E}\exp(-i\omega t)\right]$, where $\mathbf{E}$ is the complex field that can be parametrized as

$$\mathbf{E} = E_0\left[\cos(\theta/2)\mathbf{l} + e^{i\phi}\sin(\theta/2)\mathbf{r}\right] = E_\mathbf{l}\mathbf{l} + E_\mathbf{r}\mathbf{r}, \tag{2.3}$$

with E_0 being a complex function of x and y that provides an overall amplitude and phase and that does not affect the polarization (defined by the expression in brackets). The circular polarization components $E_{\mathbf{l},\mathbf{r}}$ are complex functions of x and y. The relative phase between them is $\phi = \phi_\mathbf{r} - \phi_\mathbf{l}$ (with $\phi_{\mathbf{r},\mathbf{l}} = \arg[E_{\mathbf{r},\mathbf{l}}]$). As discussed, E_0 traces an ellipse within the transverse plane over each optical cycle. We now describe equations for the optical fields that implement these textures, independently of the mapping function $w(z)$. Since $w(z) = \tan(\theta/2)e^{i\phi}$, Eq.(2.3) can be written as $\mathbf{E} = E_\mathbf{l}(z)[\mathbf{l} + w(z)\mathbf{r}]$, so that any reasonable choice for $E_\mathbf{l}(z)$ leads to the desired polarization texture as long as $E_\mathbf{r}(z) = E_\mathbf{l}(z)w(z)$. However, it is desirable to choose a functional form that avoids singularities in the field, and that treats the two hemispheres similarly. Note that, in our convention, the hemisphere with left(right)-handed ellipses corresponds to $|w(z)| < (>)\,1$, with the pole representing left(right)-circular polarization corresponding to $w(z) = 0\,(\infty)$. It is then desirable to find an expression for $E_\mathbf{l}(z)$ such that $E_\mathbf{r}(z) = E_\mathbf{l}(z)w(z)$ takes a similar functional form except for the replacement $w \to 1/w$. One such solution is

$$E_\mathbf{l}(z) = E_0\sqrt{-w_0}\,\frac{w^*(z) - w_0^*}{|w(z)|^2 + |w_0|^2}, \tag{2.4a}$$

$$E_\mathbf{r}(z) = E_0\sqrt{\frac{1}{-w_0}}\,\frac{1/w^*(z) - 1/w_0^*}{|1/w(z)|^2 + |1/w_0|^2}, \tag{2.4b}$$

where E_0 is a constant amplitude factor and w_0 is a dimensionless constant. Note that both polarization components vanish at points where $w(z) = w_0$, meaning that this construction forces zeros in the field at points where the polarization is such that $\tan(\theta/2)e^{i\phi} = w_0$. It is easy to show that the expression for the intensity becomes simpler when w_0 is chosen such that $|w_0| = 1$, giving

$$I(z) = \frac{|w(z) - w_0|^2}{|w(z)|^2 + 1}. \tag{2.5}$$

In this case the field zeros coincide with points of linear polarization with orientation angle equal to $\arg(w_0)/2$. In what follows we choose $w_0 = -1$ to simplify the expressions; the zeros then coincide with points of vertical linear polarization. We rewrite Eq. (2.4) in terms of the linear polarization components:

$$E_{\mathbf{x}} = \frac{1}{\sqrt{2}}\left(E_{\mathbf{r}} + E_{\mathbf{l}}\right), \quad E_{\mathbf{y}} = \frac{i}{\sqrt{2}}\left(E_{\mathbf{r}} - E_{\mathbf{l}}\right). \tag{2.6}$$

We compute the amplitude and phase of those components and use them to generate the cartographic maps with the numerical and experimental methods described in the first section of this chapter. The measured intensity distributions are shown in Fig. 2.5. With those intensities, we compute the Stokes parameters, the ellipse of the polarization map, and the Skyrme density shown in Fig. 2.6.

Note that the measured Skyrme density has the same sign across the analysed field of view except in the vicinity of the points (blue areas) of vertical linear polarization, which correspond to the points where both circular components vanish. As discussed in [41] the angular spectrum of the fields described in Eq. (2.4) spans an infinite area in the Fourier domain which is impossible to resolve with pixel-based modulators. This explains the observation of changes on the sign of ρ_S. In the next section, we describe some polarization structures with a finite angular spectrum that present a more stable behaviour of the sing of ρ_S.

2.6. Propagation invariant meron lattices.

In this section, we present a family of Meron lattices whose angular spectrum is restricted to a ring in the Fourier space. As a consequence, the spatial distributions of intensity and polarization are propagation invariant.

The first texture we present is a square meron lattice with uniform intensity. It is derived by first expressing $\mathbf{E}$ in the $\mathbf{x}$, $\mathbf{y}$ basis as $\mathbf{E} = E_0'\left[\cos(\alpha/2)e^{-i\delta/2}\mathbf{x} + \sin(\alpha/2)e^{i\delta/2}\mathbf{y}\right]$, where E_0', α, δ may vary as functions of (x, y). The polarization state is now determined by the parameters α and δ, whereas E_0' serves as a global amplitude and phase function. Note that the parameters α and δ represent spherical angles with respect to the s_1 axis, in contrast to θ and ϕ, which denote spherical angles with respect to the s_3 axis. As a result, we have $\mathbf{s} = (\cos\alpha, \sin\alpha\cos\delta, \sin\alpha\sin\delta)$.

A field with a uniform intensity distribution can be achieved by making E_0' constant, chosen here for simplicity as $E_0' = 1$. Then, to obtain regions spanning the Poincaré sphere, we assign the angles α and δ in $\mathbf{E}$ to be functions that vary proportionally with the (x, y) coordinates. Specifically, we assign $\alpha \to 2\tilde{x}$ and $\delta \to 2\tilde{y}$, where $\tilde{x} = k_\perp x$ and $\tilde{y} = k_\perp y$, with $k_\perp$ being a positive constant. This results in the periodic coverage of the Poincaré sphere within regions where α and δ sweep a range of π and 2π, respectively, through an equirectangular projection with the poles located at the s_1 axis. In this projection, meridians (parallels) are proportionally mapped to x (y). The resulting complex field is given by $\mathbf{E} = \cos\tilde{x}e^{-i\tilde{y}}\mathbf{x} + \sin\tilde{x}e^{i\tilde{y}}\mathbf{y}$, and its circular polarization components are

$$E_{\mathbf{l},\mathbf{r}} = \frac{\cos\left[(\tilde{x} \mp \tilde{y})\right] \mp i\sin\left[(\tilde{x} \pm \tilde{y})\right]}{\sqrt{2}}. \tag{2.7}$$

Expanding the trigonometric functions in $\mathbf{E}$ into a sum of complex exponential

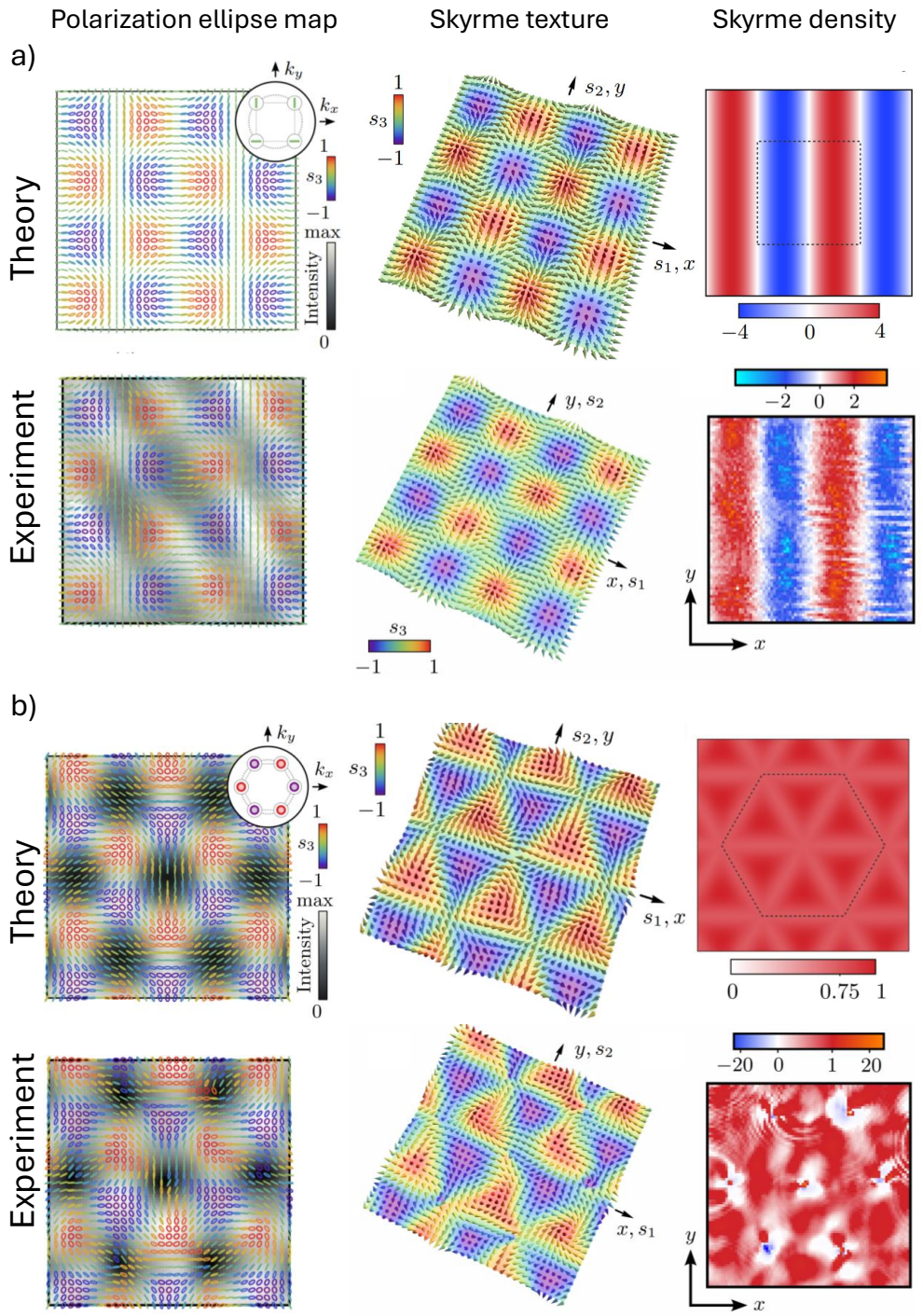

Figure 2.7.: Theoretical and experimental polarization ellipses, Skyrmion textures and Skyrme density, corresponding to: a) a square meron lattice with uniform intensity and b) a triangular meron lattice with a constant sign of ρ_S.

terms reveals that the field is composed of a superposition of four plane waves, with two waves polarized along the x direction and two along the y direction. This decomposition illustrates that $k_\perp$ is indeed the absolute value of the transverse component of wave vectors of the plane waves. The diffraction orders in the field's angular spectrum depicted in Fig. 2.7a indicate that the transverse wave vectors of the four plane waves lie on the same ring so that the texture is propagation-invariant.

Similarly to the cartographic maps, it is more convenient from an experimental point of view to modulate the linear polarization components, so we use Eq. (2.6) to obtain the amplitude and phase of the horizontal and vertical components that are modulated using the method described at the beginning of this chapter. Figure 2.7a) also shows the theoretical and experimental comparison between the polarization maps, the Skyrme texture and the Skyrme density. Notice that, contrary to the beams in the previous section, the Skyrme density oscillates between positive and negative values.

We now introduce a more unconventional family of textures. These are triangular meron lattices that not only remain invariant under propagation but also exhibit uniform sign of the skyrme density, $\mathrm{sgn}(\rho_S)$, across the entire transverse plane just as the cartographic maps do. The circular polarization components of a field rendering these lattices are

$$E_{\mathbf{l},\mathbf{r}} = e^{\mp i\tilde{x}} + 2\, e^{\pm i\tilde{x}/2} \cos\left(\frac{\sqrt{3}}{2}\tilde{y} \pm \frac{2\pi}{3}\right). \tag{2.8}$$

Figure 2.7b illustrates the field's distributions of polarization ellipses and intensity, Skyrme texture and ρ_S. The merons take the shape of equilateral triangles. The unit cell of the texture is a hexagon, including six merons. Note that the triangular arrangement of the texture's merons matches that of a triangular lattice achieved through a conformal transformation introduced in the context of cartography in the previous section, known as Adam's *world in a hexagon projection*. The texture presented in this section is not conformal, but it is invariant under propagation, owing to the fact that the transverse wavevectors of the plane waves forming the field align along a ring (with radius $k_\perp$), as depicted in the inset in Fig. 2.7b. Moreover, in theory, propagation does not disturb the zeros of the field.

The angular spectrum of the field is found by expanding Eqs. (2.8) into complex exponentials representing individual plane waves. Each component $E_{\mathbf{l},\mathbf{r}}$ is a mix of three plane waves. The entire field is composed of six plane waves, characterized by their transverse wavevectors situated at the vertices of a hexagon. Adjacent vertices of the hexagon belong to orthogonal circular polarization components.

2.7. Final remarks

In this chapter, we introduced an experimental method to imprint arbitrary polarization structures in a laser beam with a phase-only spatial light modulator. The setup is based on the separation of an incoming beam into its vertical and horizontal polarization components by a Wollaston prism. The separation angle between the

components is 1° which allows us to manipulate both components with the same optical elements (except for a HWP that only affects one component). This feature provides the setup with stability against external mechanical noise, which makes it suitable for generating more complex structures of polarization, especially at nanoscales. In chapter 5, we discuss how to use this setup as the illumination part of the microscope system used to generate and measure nonparaxial polarized fields.

We introduced two families of Skyrmionic periodic textures. The first one was obtained by mapping the Poincaré sphere to real space with conformal transformations introduced in the 19th century in the context of mapping. The second family corresponds to Meron lattices generated by the interference of a few plane waves arranged in a ring in Fourier space, which confers the property of propagation invariance to the field. In practice, however, the invariance is observed over only a few centimeters. In both cases, the fields are the result of the superposition between two spatially modulated beams. Stable polarization structures were measured with sequential intensity measurements thanks to the interference stability.

3. Measuring 3D oriented dipoles with a microscope: General considerations.

Sommaire

3.1. Introduction: 3D oriented dipoles in microscopy. 49
3.2. Dipole PSF description in terms of Stokes-Gell-Mann basis. 58
3.3. Stokes-Gell-Mann basis for polarized measurements. 63
3.4. Fisher Information Matrix 66
3.5. Final remarks 70

3.1. Introduction: 3D oriented dipoles in microscopy.

Dipole emitters are the most common source of radiation. At optical frequencies, a plethora of physical systems can be considered as dipolar sources: atoms, fluorescent molecules, metallic nanoparticles, and quantum dots, to name a few. In imaging and studies of light propagation through complex media, the interaction of light with matter can be simulated by assuming the medium to be composed of a large number of dipole scatterers.

Electrical dipoles are characterized by their *dipole moment vector* $\hat{\boldsymbol{\mu}} = (\mu_x, \mu_y, \mu_z)$, whose complex components, $\mu_i = A_i e^{i\phi_i}$, encode the amplitude and phase of the oscillation projection along the Cartesian axes. We name *rectilinear dipoles* the specific case where the three components oscillate in phase, and *elliptical dipoles* those for which some of the dipole components oscillate out of phase. Rectilinear dipoles are a source of linearly polarized light, whereas elliptical dipoles can generate elliptically polarized light. However, the radiation produced by these dipoles is not isotropic and depends on the direction of observation.

The main goal of this chapter is to describe the experimental conditions necessary to measure $\hat{\boldsymbol{\mu}}$ within the framework of the generalized Stokes-Gell-Mann parameters when the dipole source is observed with a microscope objective of high numerical aperture in imaging configuration. For a rectilinear dipole, the components of $\hat{\boldsymbol{\mu}}$ are the Cartesian coordinates of its orientation in 3D.

To begin, we describe the model used to simulate the system of dipoles close to a dielectric interface and its observation utilizing a high numerical objective system [15, 23, 54]. The system is illustrated in Fig. 3.1a-b.
The electric field at any point in space $\mathbf{r}$, radiated by a dipole located at $\mathbf{r}_0$ is given by

$$\mathbf{E}(\mathbf{r}) = \mathbf{G}_0(\mathbf{r},\mathbf{r}_0)\cdot\hat{\boldsymbol{\mu}}, \tag{3.1}$$

where $\mathbf{G}_0(\mathbf{r},\mathbf{r}_0)$ is the Green function, whose angular spectrum representation is given by

$$\mathbf{G}(\mathbf{r},\mathbf{r}_0) = \frac{i}{8\pi}\iint_{\infty}^{\infty}\mathbf{M}e^{-i(k_x(x-x_0)+k_y(y-y_0)+k_z(z-z_0))}dk_xdk_y, \tag{3.2}$$

with

$$\mathbf{M} = \frac{1}{k_1^2k_{z1}}\begin{bmatrix} k_1^2-k_x^2 & -k_xk_y & \mp k_xk_{z1} \\ -k_xk_y & k_1^2-k_y^2 & \mp k_yk_{z1} \\ \mp k_xk_{z1} & \mp k_yk_{z1} & k_1^2-k_{z1}^2 \end{bmatrix}. \tag{3.3}$$

As before, $k_1 = n_1k_0$ is the wave number in the medium with index of refraction n_1 and $k_{z1} = \sqrt{k_1^2-k_x^2-k_y^2}$. Equation (3.1) can be interpreted as a matrix multiplication to compute the complete electric field at every point for a given $\hat{\boldsymbol{\mu}}$.

The next step is to compute the transmission of the field through the planar interface. In fluorescence microscopy, the fluorophores are usually immersed in water and when observed with oil-immersion objectives the emission traverses the water-glass interface. In some other cases, as discussed in the next chapter, the dipoles can be immersed in a medium that matches the glass index of refraction, in this case, the effect of the interface is negligible.

One of the advantages of expressing the Green tensor, and hence the electric field as a decomposition of plane waves is that the transmission and reflection of the dipole field through the interface can be easily computed by multiplying each plane wave by the corresponding Fresnel coefficients for the s (transverse electric) and p (transverse magnetic) components, given by

$$r^s(k_x,k_y) = \frac{\mu_2k_{z1}-\mu_1k_{z2}}{\mu_2k_{z1}+\mu_1k_{z2}}, \qquad r^p(k_x,k_y) = \frac{\epsilon_2k_{z1}-\epsilon_1k_{z2}}{\epsilon_2k_{z1}+\epsilon_1k_{z2}}, \tag{3.4}$$

$$t^s(k_x,k_y) = \frac{2\mu_2k_{z1}}{\mu_2k_{z1}+\mu_1k_{z2}}, \qquad t^p(k_x,k_y) = \frac{2\epsilon_2k_{z1}}{\epsilon_2k_{z1}+\epsilon_1k_{z2}}\sqrt{\frac{\mu_2\epsilon_1}{\mu_1\epsilon_2}}, \tag{3.5}$$

where ϵ_i and μ_i are the permittivity and permeability of the medium i respectively. We can decompose the electric field in the $p-s$ components and multiply the corresponding terms by the Fresnel coefficients. In this case, s and p are the unitary vectors in spherical coordinates $\mathbf{n}_\theta$ and $\mathbf{n}_\phi$ respectively defined as

$$\mathbf{n}_\theta = \begin{pmatrix} \cos\theta\cos\phi \\ \cos\theta\sin\phi \\ -\sin\theta \end{pmatrix}, \qquad \mathbf{n}_\phi = \begin{pmatrix} -\sin\phi \\ \cos\phi \\ 0 \end{pmatrix}. \tag{3.6}$$

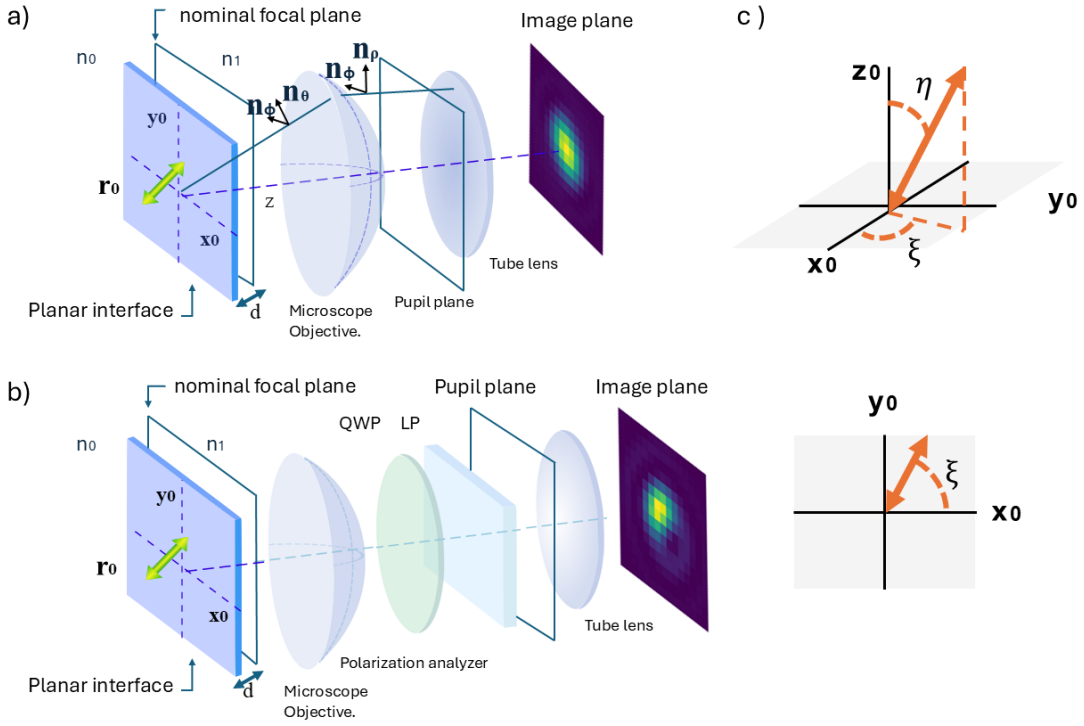

Figure 3.1.: Microscope configurations. a). A 3D oriented dipole located at the position $\mathbf{r_0}$ (measured in the reference system defined by the planar interface; $z_0 = 0$ corresponding to the case of a dipole located exactly over the interface) is immersed in a medium of index n_0 and its radiation is transmitted to a second medium of index n_1. The interface between the two media is located at a distance d from the nominal focal plane of a high numerical aperture lens that collects the light. The signal is collimated by this lens and focused on the image plane of the system. In reality, the signal is detected by a pixelated camera. The parameters of the simulation are chosen to match the real conditions. b) Polarization microscope. In theory, it is always possible to compute the linear polarization components of the collimated signal; in practice, these components are observed by placing a linear polarizer. The circular polarization components can be observed by placing a QWP followed by a linear polarizer. c) Coordinate system, where η represents the angle between the dipole's major axis of oscillation and the optical axis, and ξ denotes the angle between the dipole projection onto the $x-y$ plane and the x-axis.

Once the transmitted field is calculated after the interface it is possible to compute the *far field* which is defined over a spherical surface of radius $r \gg \lambda$ and collimated by the high NA lens:

$$\mathbf{E}(\mathbf{r}) = \frac{\omega^2}{\epsilon_0 c^2}\mu_1 \mathbf{G}_t(\mathbf{r},\mathbf{r}_0)\cdot\hat{\boldsymbol{\mu}}, \tag{3.7}$$

with

$$\mathbf{G}_t(\mathbf{r},\mathbf{r}_0) = \frac{e^{ik_2 r}}{4\pi r} e^{-i\left[k_1\left(x_0\frac{x}{r}+y_0\frac{y}{r}\right)-z_0 k_1\sqrt{1-\left(\frac{k_2\rho}{k_1 r}\right)^2}\right]} e^{id k_2\sqrt{1-\left(\frac{\rho}{r}\right)^2}} \times \begin{bmatrix} \frac{x^2z^2}{\rho^2r^2}\Phi_2+\frac{y^2}{\rho^2}\Phi_3 & \frac{xyz^2}{\rho^2r^2}\Phi_2-\frac{xy}{\rho^2}\Phi_3 & -\frac{xz}{r^2}\Phi_1 \\ \frac{xyz^2}{\rho^2r^2}\Phi_2-\frac{xy}{\rho^2}\Phi_3 & \frac{y^2z^2}{\rho^2r^2}\Phi_2+\frac{x^2}{\rho^2}\Phi_3 & -\frac{yz}{r^2}\Phi_1 \\ -\frac{xz}{r^2}\Phi_2 & -\frac{yz}{r^2}\Phi_2 & \left(1-\frac{z^2}{r^2}\right)\Phi_1 \end{bmatrix}, \tag{3.8}$$

where the coordinates (x, y, z) are defined over the reference sphere, (x_0, y_0, z_0) are the dipole coordinates, d is the distance of the interface to the nominal focal plane (shown in Fig. 3.1a-b) that is used to compute the collimation of the dipole signal by the objective, $\rho = \sqrt{x^2+y^2}$ is the transversal radial spatial coordinates at the reference sphere, k_1 and k_2 are the wavenumbers in the medium with index of refraction n_0 and n_1, and r is the distance associated with the focal length of the objective. The functions Φ_1, Φ_2 and Φ_3 are given by

$$\Phi_1 = t^p \frac{n_1 k_1}{n_0 r\sqrt{k_1^2 - k_2\rho/r}}, \qquad \Phi_2 = -t^p\frac{n_1}{n_0}, \qquad \Phi_3 = t^s\frac{k_2 z}{r\sqrt{k_1^2-k_2\rho/r}}. \tag{3.9}$$

The first exponential factor in eq. 3.8 accounts for the phase and amplitude due to the propagation until the sphere of reference, the second exponential term contains the phase related to the 3D position of the dipole in the immersion medium, and the third one accounts for the phase gained by the defocused interface, if there is any, and equation (3.7) and (3.8) are used to compute the field at the reference sphere. Note that the field can have three polarization components, but once it is collimated by the objective lens only the two transverse components remain. Mathematically this can be understood by describing the far field in terms of the spherical unitary vectors and replacing the vector $\mathbf{n}_\theta \to \mathbf{n}_\rho$, as illustrated in Fig. 3.1a, where

$$\mathbf{n}_\rho = \begin{pmatrix} \cos\phi \\ \sin\phi \\ 0 \end{pmatrix}. \tag{3.10}$$

Additionally, we have to multiply the resulting field by the factor $\frac{1}{\sqrt{z}}$ to account for

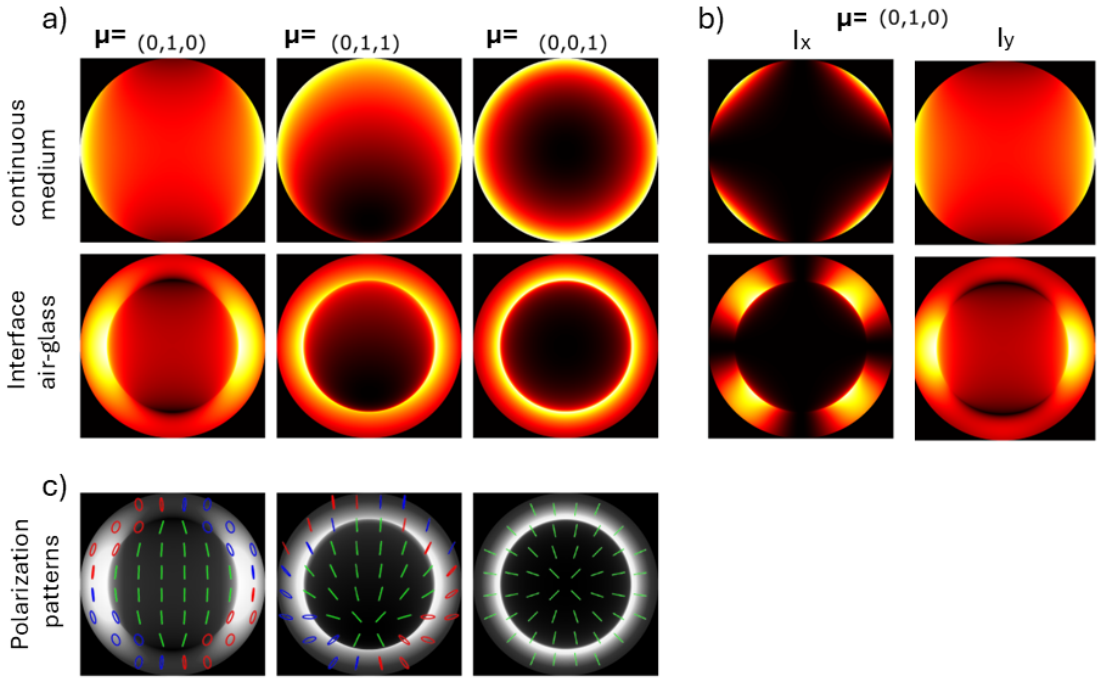

Figure 3.2.: a). Normalized intensity distributions at the pupil plane for rectilinear dipoles located at the focal plane with dipole moments $\hat{\boldsymbol{\mu}} = (0,1,0)$, $\frac{1}{\sqrt{2}}(0,1,1)$, and $(0,0,1)$. In the top and bottom lines, the results are shown both for a continuous medium and an air-glass interference, with NA=1.0 and 1.49 respectively. The interface is assumed to coincide with the focal plane and the emitter at the origin. b) The field's linear **x**-**y** polarization components are shown for the dipole $(0,1,0)$. Note that most of the energy for a dipole oriented along y is contained in the **y** linear polarization field component. c) Polarization distribution at the pupil plane. Note that elliptically polarized light can be measured in the SAF region. The red/blue ellipses are associated with left/right handedness whereas green corresponds to linearly polarized light.

energy conservation [55]:

$$\mathbf{E}(\mathbf{r})_{\text{Pup}} \propto \frac{1}{\sqrt{z}}[(\mathbf{G}_t \cdot \hat{\boldsymbol{\mu}}) \cdot \mathbf{n}_\theta]\mathbf{n}_\rho + \frac{1}{\sqrt{z}}[(\mathbf{G}_t \cdot \hat{\boldsymbol{\mu}}) \cdot \mathbf{n}_\phi]\mathbf{n}_\phi, \tag{3.11}$$

The field $\mathbf{E}(\mathbf{r})_{\text{Pup}}$ is defined at the plane located at the output of the objective. This plane is referred to as the *pupil plane* or *back-focal plane*. In Fig. 3.2 examples of intensity distributions at the pupil plane $I_{Pup} = \mathbf{E}(\mathbf{r})^*_{\text{Pup}} \cdot \mathbf{E}(\mathbf{r})_{\text{Pup}}$ for different dipole configurations are shown. In Fig. 3.2 we show examples of a dipole contained in the sample plane e.g. $\mu = (0,1,0)$, referred to as *transverse dipoles* and other two dipoles with orthogonal components to the sample plane. Emitters orthogonally oriented to the sample plane are called *longitudinal dipoles* e.g. $\mu = (0,0,1)$.

We also consider the possible presence of an interface. In particular, in conditions of a dipole immersed in a medium n_0 close to the interface with a second medium $n_1 > n_0$ (at a distance $z_0 < \lambda$), observed with an objective of NA$> n_0$, it is possible to observe contributions from the evanescent components of the dipole radiation that couple onto propagating waves after the interface. In the context of fluorescence microscopy, this radiation is referred to as *Supercritical Angle Fluorescence* (SAF) and is contained on the external ring of the pupil field, as seen in Fig. 3.2a. Those components can be seen in Eq. (3.8), specifically in the exponential term $\exp\left(i z_0 k_1 \sqrt{1-(\frac{k_2 \rho}{k_1 r})^2}\right)$, in regions of the pupil plane where the square root term becomes imaginary. The complex exponential then becomes real and decreases its amplitude with z_0.

As mentioned already, the intensity and polarization at the pupil plane contain valuable information about a single dipole configuration. As the number of dipoles increases, the information starts to intermix at the pupil plane. Hence, it is convenient to measure the signal at the image plane formed by a second lens (a tube lens) where the radiation coming from different dipoles is separated, as illustrated in Fig. 3.1. The tube lens essentially performs a 2D Fourier transform to $\mathbf{E}_{\text{Pup}}$, defined in Eq. (3.11). It is possible to show [56] that the field at the pupil plane can be seen as the matrix multiplication $\mathbf{E}_{\text{Pup}} = \mathbf{G}_{\text{Pup}} \cdot \hat{\boldsymbol{\mu}}$, where $\mathbf{G}_{\text{Pup}}$ contains the information of $\mathbf{G}_t$, the vectors $\mathbf{n}_\rho$, $\mathbf{n}_\phi$ and $\mathbf{n}_\theta$.

The field at the image plane is given by $\mathbf{E}_{\text{Pup}} = \text{FT}[\mathbf{E}_{\text{Pup}}]$ and consequently, the measured intensity at the camera plane is given by $I_{\text{Imag}} = \text{FT}[\mathbf{E}_{\text{Pup}}]^\dagger \text{FT}[\mathbf{E}_{\text{Pup}}]$, which can be simplified to

$$I_{\text{Imag}} = \hat{\boldsymbol{\mu}}^\dagger \text{FT}[\mathbf{G}_{\text{Pup}}]^\dagger \text{FT}[\mathbf{G}_{\text{Pup}}]\hat{\boldsymbol{\mu}}. \tag{3.12}$$

We can rewrite this expression as

$$I_{\text{Imag}} = \sum_{i=1}^{3}\sum_{j=1}^{3} G^{ij}_{\text{Imag}} \hat{\mu}^*_i \hat{\mu}_j. \tag{3.13}$$

The final measured intensity distribution at the camera associated with a single dipole $\hat{\boldsymbol{\mu}}$ can be expressed as a superposition of the G^{ij}_{Imag} weighted by the product of the dipole moment elements; this intensity distribution is referred to as the *Point Spread Function*, PSF. The linear relation between the PSF and the dipole moments was

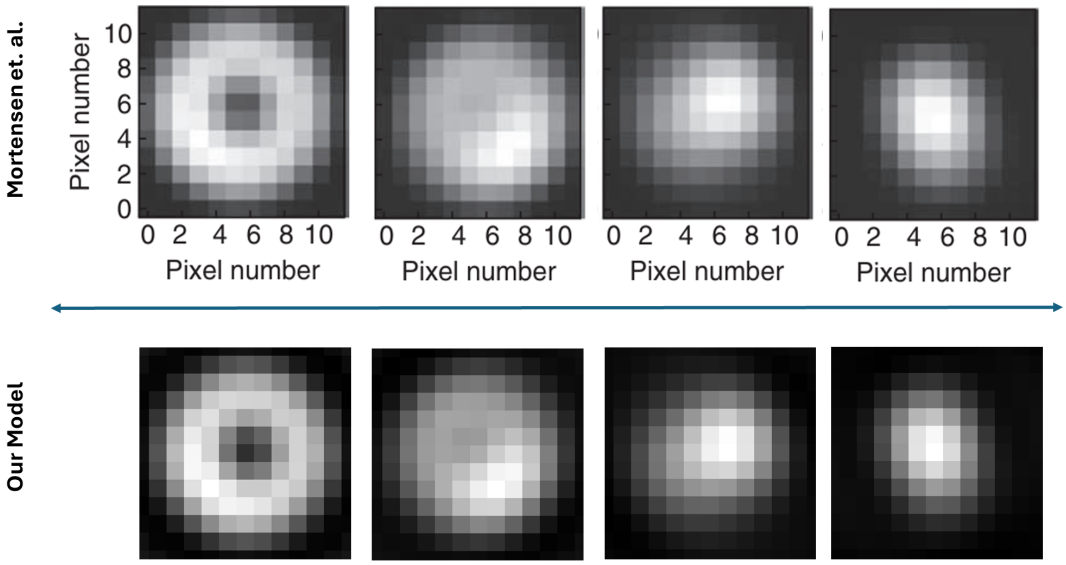

Figure 3.3.: Comparison between simulated PSFs and those in Ref. [11]. The physical parameters are: NA=1.49, Mag.=100, pixel size=44 nm, $\lambda = 578$ nm, and angles (η,ξ), from left to right: $(16°,0.4°)$,$(34°,1.3°)$,$(51°,2.1°)$,$(67°,2.8°)$. The window dimensions are 10×10 pixels.

proven for rectilinear dipoles in the context of SMOLM [57] where only six different G^{ij}_{Imag} are necessary to completely characterize the system, but is valid for the general case of elliptical dipoles [23] for which nine functions are needed.

Equation (3.12) is used to compute the intensity distribution of elliptical dipoles. For this project, a code in MATLAB was written to simulate the PSF associated with any elliptical dipole $\hat{\boldsymbol{\mu}}$ in any possible microscope characterized by $\mathbf{G}_{\text{Pup}}$. The Fourier transform is implemented by using the *fast Fourier transform* (FFT) algorithm. The typical integration mesh dimensions are $2^{10} \times 2^{10}$; what we referred to as the the pixel size corresponds to the actual pixel size of our detector divided by the magnification; in all the experiments shown in the next chapters the pixel size is 52.7 nm. In Fig. 3.4 a comparison between PSFs associated with rectilinear dipoles reported in previous work [11] and the ones computed with our algorithm are presented to show the PSF dependence on the orientation parameters and to validate our code.
It is convenient to define the *second-moments matrix* $\mathbb{m}$ as the correlation matrix of the elements of the dipole moment vector $\hat{\boldsymbol{\mu}}$:

$$\mathbb{m}_{ij} = \langle \hat{\mu}_i^\dagger \hat{\mu}_j \rangle_T = \frac{1}{T} \int_{t_0}^{t_0+T} \hat{\mu}(t)_i^\dagger \hat{\mu}(t)_j \, dt, \tag{3.14}$$

where $\langle\cdot\rangle$ indicates time averaging and T is the detection integration time; $\mathbb{m}$ and the nonparaxial polarization matrix Γ_{3D} are closely related mathematical objects: while $\mathbb{m}$ describes physical oscillations of charges, Γ_{3D} describes field oscillations.

Note that all physical quantities described for Γ_{3D} have an associated equivalent physical parameter related to $\mathbb{m}$. For instance, in the case of rectilinear dipoles representing single molecules, the 3D linear polarized field is equivalent to the 3D physical orientation of the transition dipole moment. The degree of polarization P corresponds to a degree of wobbling of the molecule (which for the simplest case of isotropic wobbling can also be quantified by the angle δ which measures the cone angle determined by the molecule rotation [18]) that quantifies its actual movement.

In the case of rectilinear dipoles, $\mathbb{m}$ is real and from its elements it is possible to recover the dipole orientation and wobble (η, ξ, δ). There are two general ways to assess this matrix (when working in imaging configuration): by *ratiometric* techniques and by *PSF engineering* methods. In ratiometric approaches, the signal from the dipole is split into different (usually polarized) channels and the relative ratio of energy contained in the channels is related to specific values of (η, ξ, δ) [58–60].

In PSF engineering techniques, a phase and/or polarization modulation is applied to the signal, typically at the pupil plane, to redistribute the orientation information contained in the PSF [11, 13, 18, 61–67]. In most of these methods, the signal is also separated in polarized channels, although some exceptions [11, 13, 61] are discussed below. The main difference between ratiometric and PSF engineering techniques is that the orientation (or second-moment matrix) information is contained in the pixelized PSF whereas in the ratiometric technique, the information is contained in the energy imbalances between the channels. Despite the accuracy reached with PSF engineering methods, their performance is limited by the complexity of the parameter retrieval process. As illustrated in Fig. 3.4, in some ratiometric methods, the orientation parameters have algebraic relations in terms of the measured quantities and the *localization* parameters can be easily found by fitting Gaussian distributions to the measured PSFs, similarly to SMLM techniques. In PSF engineering techniques, on the other hand, it is necessary to fit the data to a PSF vectorial model in which the spatial variables (x_0, y_0, z_0) are also free parameters. This is usually done by maximizing the likelihood function between the data and the model. In most PSF engineering methods, the data analysis processing time is one of the main constraints. PSF engineering is not restricted to orientation parameters; it has also been used to encode the z_0 coordinate of the emitters in several ranges. By placing a cylindrical lens at the pupil plane it is possible to perform 3D STORM [68] with an axial range of 1μm. In other works, phase modulation imprinted with a spatial light modulator has allowed to increase the accessible range in z_0 to tens of microns [69, 70].

The problem of simultaneous 3D localization and 3D orientation of rectilinear dipoles has been discussed and proven in some of the work mentioned earlier. In the next section, an alternative dipole PSF formulation is presented and its advantages are described.

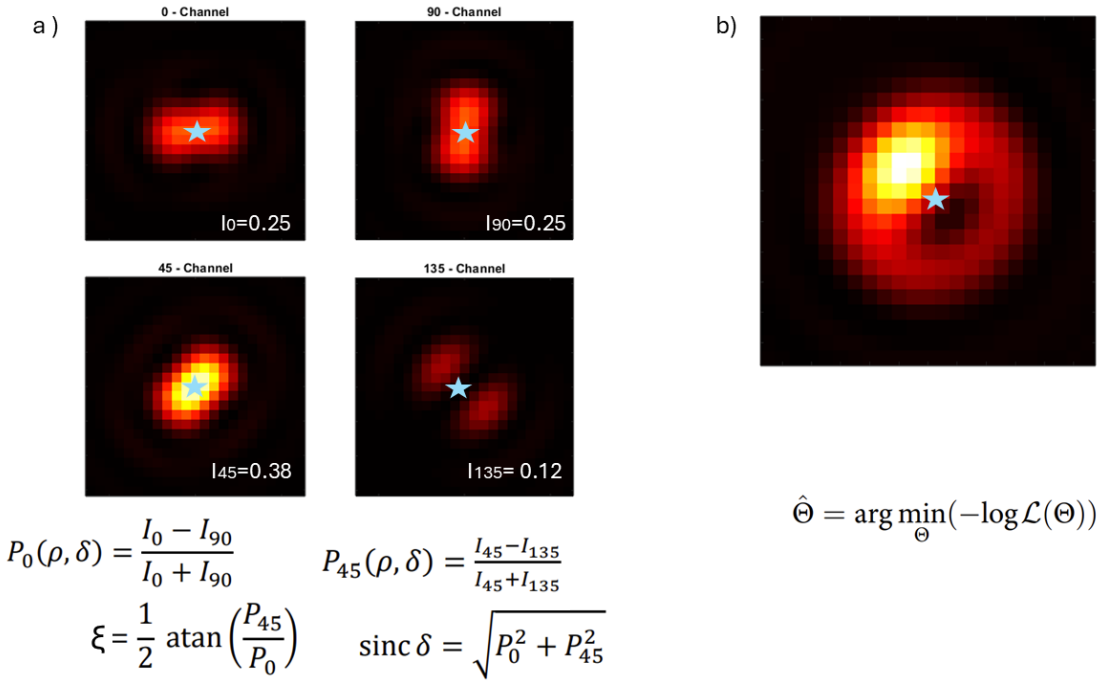

Figure 3.4.: Comparison between ratiometric and PSF engineering methods. a) Working principle of 2D-4Polar STORM microscopy [60]. The signal collected by the objective is separated into four linearly polarized channels oriented at 0°, 90°, 45° and 135°. The dipole is localized by simply finding the centroid of the 2D Gaussian distribution that best fits the PSF in each channel (shown as a star) and the angular parameters (ξ,δ) are computed from the total intensity distributions contained in each window. As discussed in Ref. [60], the expression for sincδ is obtained by assuming a flat cone. The dipole parameters are $(\eta = 45°, \xi = 45°, \delta = 0)$. The dipole is immersed in water and is above the water/glass interface located at the focal plane of an objective of NA=1.33, $\lambda = 630$ nm. b) PSF associated with the same dipole and microscope parameters. A vortex phase modulation was introduced at the pupil plane of the microscope [13]. From this single image it is possible to measure (η,ξ). The dipole localization is not as simple as in the ratiometric approach and the orientation information is spread over many pixels. Maximization of the likelihood function (or minimization of the negative logarithm of the likelihood) is routinely used to estimate not only the orientation parameters but also the spatial coordinates. All these parameters are denoted by a $\hat{\Theta}$.

3.2. Dipole PSF description in terms of Stokes-Gell-Mann basis.

Equation (3.13) describes the PSF of a dipole as a linear superposition of some functions weighted by the elements of $\mathbb{m}$. The goal of this section is to exploit this simple formulation by using a more *balanced* basis. We start by describing the matrix of second moments in terms of the Stokes-Gell-Mann parameters. As discussed earlier, $\mathbb{m}$ is equivalent to Γ_{3D} and mathematically we can simply write

$$\mathbb{m} = \frac{1}{2}\begin{pmatrix} \frac{2}{3}S_0 + S_{11} + \frac{S_{12}}{\sqrt{3}} & S_{23} - iS_{33} & S_{22} + iS_{32} \\ S_{23} + iS_{33} & \frac{2}{3}S_0 - S_{11} + \frac{S_{12}}{\sqrt{3}} & S_{21} - iS_{31} \\ S_{22} - iS_{32} & S_{21} + iS_{31} & \frac{2}{3}S_0 - 2\frac{S_{12}}{\sqrt{3}} \end{pmatrix}, \tag{3.15}$$

with

$$\begin{aligned} &S_0 = \mathrm{Tr}[\mathbb{m}] = \langle \mu_x \mu_x^* \rangle + \langle \mu_y \mu_y^* \rangle + \langle \mu_z \mu_z^* \rangle, \\ &S_{11} = \langle \mu_x \mu_x^* \rangle - \langle \mu_y \mu_y^* \rangle, \qquad S_{12} = \frac{\langle \mu_x \mu_x^* \rangle + \langle \mu_y \mu_y^* \rangle - 2\langle \mu_z \mu_z^* \rangle}{\sqrt{3}}, \\ &S_{21} = 2\mathrm{Re}\langle \mu_z \mu_y^* \rangle, \qquad S_{22} = 2\mathrm{Re}\langle \mu_x \mu_z^* \rangle, \qquad S_{23} = 2\mathrm{Re}\langle \mu_y \mu_x^* \rangle, \\ &S_{31} = 2\mathrm{Im}\langle \mu_z \mu_y^* \rangle, \qquad S_{32} = 2\mathrm{Im}\langle \mu_x \mu_z^* \rangle, \qquad S_{33} = 2\mathrm{Im}\langle \mu_y \mu_x^* \rangle. \end{aligned} \tag{3.16}$$

We can then rewrite Eq. (3.13) in terms of the Stokes-Gell-Mann parameters as

$$I_{\mathrm{Imag}} = S_0 I_0 + \sum_j I_j S_j, \tag{3.17}$$

where the index j denotes $\{11,12,21,22,23,31,32,33\}$. We can interpret each term I_j in this equation as an incoherent superposition of PSFs corresponding to different dipole configurations based on the decomposition of $\mathbb{m}$ in terms of the Gell Mann matrices, as shown in Eq. (1.16). For instance, S_0 in Eq. (1.16) multiplies the 3×3 identity matrix which can also be decomposed as

$$\begin{pmatrix} 1 & 0 & 0 \\ 0 & 1 & 0 \\ 0 & 0 & 1 \end{pmatrix} = \begin{pmatrix} 1 & 0 & 0 \\ 0 & 0 & 0 \\ 0 & 0 & 0 \end{pmatrix} + \begin{pmatrix} 0 & 0 & 0 \\ 0 & 1 & 0 \\ 0 & 0 & 0 \end{pmatrix} + \begin{pmatrix} 0 & 0 & 0 \\ 0 & 0 & 0 \\ 0 & 0 & 1 \end{pmatrix}. \tag{3.18}$$

The three matrices on the right are the second-moment matrices of rectilinear dipoles oriented along the x, y and z axes, illustrated in Fig. 3.5a. Hence, the corresponding I_0 is given by $I_0 = (I^x + I^y + I^z)/\sqrt{3}$, which is the sum of the PSFs associated with rectilinear dipoles oriented along the x, y and z axes. The second matrix in the basis, Θ_{11}, is given by

$$\begin{pmatrix} 1 & 0 & 0 \\ 0 & -1 & 0 \\ 0 & 0 & 0 \end{pmatrix} = \begin{pmatrix} 1 & 0 & 0 \\ 0 & 0 & 0 \\ 0 & 0 & 0 \end{pmatrix} - \begin{pmatrix} 0 & 0 & 0 \\ 0 & 1 & 0 \\ 0 & 0 & 0 \end{pmatrix}, \tag{3.19}$$

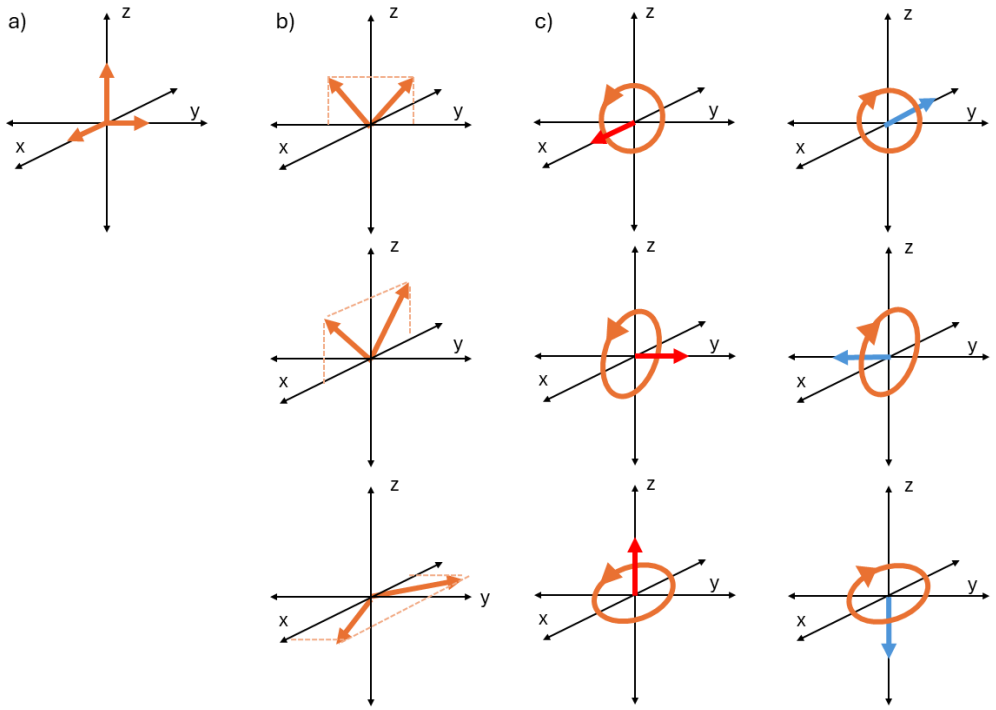

Figure 3.5.: Illustration of the fundamental dipoles used to construct the Stokes-Gell-Mann basis. a) Rectilinear dipoles oriented along the Cartesian axes. b) Rectilinear dipoles rotated 45 ° with respect to the Cartesian axes. c) Circular dipoles of opposite spin contained on the Cartesian $y-z$, $x-z$ and $x-y$ planes, respectively.

which can be interpreted as the difference of the second moments matrix for dipoles in the x and y directions. The corresponding function I_{11} is given by $I_{11} = I^x - I^y$. The third matrix in the basis is Θ_{12}, that can be written as

$$\frac{1}{\sqrt{3}}\begin{pmatrix} 1 & 0 & 0 \\ 0 & 1 & 0 \\ 0 & 0 & -2 \end{pmatrix} = \frac{1}{\sqrt{3}}\begin{pmatrix} 1 & 0 & 0 \\ 0 & 0 & 0 \\ 0 & 0 & 0 \end{pmatrix} + \frac{1}{\sqrt{3}}\begin{pmatrix} 0 & 0 & 0 \\ 0 & 1 & 0 \\ 0 & 0 & 0 \end{pmatrix} - \frac{2}{\sqrt{3}}\begin{pmatrix} 0 & 0 & 0 \\ 0 & 0 & 0 \\ 0 & 0 & 1 \end{pmatrix}. \tag{3.20}$$

Similarly to the previous case, the three matrices on the right are the second-moment matrices for dipoles in the x, y and z directions, and the corresponding function $I_{12} = (I^x + I^y - 2I^z)/\sqrt{3}$. The next element I_{21} is associated with Θ_{21}:

$$\begin{pmatrix} 0 & 0 & 0 \\ 0 & 0 & 1 \\ 0 & 1 & 0 \end{pmatrix} = \frac{1}{2}\begin{pmatrix} 0 & 0 & 0 \\ 0 & 1 & 1 \\ 0 & 1 & 1 \end{pmatrix} - \frac{1}{2}\begin{pmatrix} 0 & 0 & 0 \\ 0 & 1 & -1 \\ 0 & -1 & 1 \end{pmatrix}, \tag{3.21}$$

where the two matrices on the right are associated with rectilinear dipoles oriented 45° to the Cartesian axes y and z respectively, shown in Fig. 3.5b. I_{21} can be understood as the difference between the PSFs of these dipoles. The next two terms I_{22} and I_{23}

can be understood similarly.

Finally, the last three elements I_{3j} can be generated from the PSF of circular dipoles. For instance, Θ_{31} can be decomposed as

$$\begin{pmatrix} 0 & 0 & 0 \\ 0 & 0 & -i \\ 0 & i & 0 \end{pmatrix} = \frac{1}{2}\begin{pmatrix} 0 & 0 & 0 \\ 0 & 1 & -i \\ 0 & i & 1 \end{pmatrix} - \frac{1}{2}\begin{pmatrix} 0 & 0 & 0 \\ 0 & 1 & i \\ 0 & -i & 1 \end{pmatrix}, \tag{3.22}$$

which is the difference of the second moment matrices related to a left and right-handed circular dipole contained in the plane (y,z), shown in 3.5c-d. Similar arguments are used to describe the last two elements.

It is convenient to write the basis elements in terms of the electric fields at the image plane, i.e. $\mathrm{FT}[\mathbf{G}_{Pup}]\cdot\hat{\boldsymbol{\mu}}$. This is particularly useful for computing the elements I_{2i} and I_{31} that can be expressed in terms of the electric field E^j at the image plane associated with rectilinear dipoles oriented along the Cartesian axis j:

$$\begin{aligned}
I_0 &= \frac{E^{x*}E^x + E^{y*}E^y + E^{z*}E^z}{\sqrt{3}} \\
I_{11} &= E^{x*}E^x - E^{y*}E^y, \\
I_{12} &= \frac{E^{x*}E^x + E^{y*}E^y - 2E^{z*}E^z}{\sqrt{3}}, \\
I_{21} &= 2\mathrm{Re}[E^{y*}E^z], \\
I_{22} &= 2\mathrm{Re}[E^{z*}E^x], \\
I_{23} &= 2\mathrm{Re}[E^{x*}E^y], \\
I_{31} &= 2\mathrm{Im}[E^{y*}E^z], \\
I_{32} &= 2\mathrm{Im}[E^{z*}E^x], \\
I_{33} &= 2\mathrm{Im}[E^{x*}E^y].
\end{aligned} \tag{3.23}$$

Computationally, is convenient to write the functions I_j only in terms of three rectilinear dipoles because only three Fourier transforms must be calculated numerically. For now, let us discuss the physical meaning of each I_j and the advantages of writing the PSF in terms of what we refer to as *Stokes-Gell-Mann PSF basis*. In Fig. 3.6 some bases are illustrated for simple microscope configurations used for measuring 3D oriented fluorophores [11, 13, 61].

The first element I_0, is the PSF of a completely depolarized dipole, (i.e. $P = 0$ or $\delta = 180$), that is, an incoherent superposition of I^x, I^y and I^z in equal amounts. I_{11} and I_{23} reflect the capability of the system to determine dipole components within the transverse plane: I_{11} is the difference between the PSF of a dipole oriented along x and other along y, and I_{23} is the PSF difference between dipoles along to the axes rotated $\pm 45^\circ$ to the x,y axes. If these elements were zero the system would not be sensitive to variations on the orientations around the z axis, i.e. ξ. Note that these two basis elements only involve in-plane dipole components. I_{12} indicates the ability of the system to measure variations in η: I_{12} is the difference between the PSFs of a

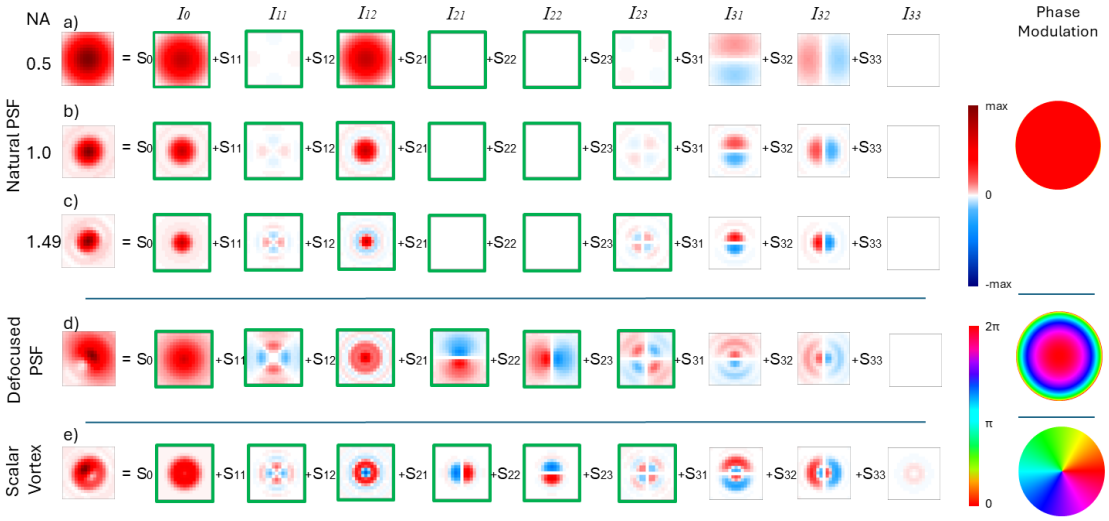

Figure 3.6.: Illustration of some Stokes-Gell-Mann PSF bases. A rectilinear dipole PSF ($\eta = 45°, \xi° = 45$) is decomposed in terms of different bases representing different experimental configurations. a)-c). Bases related to the PSF of a simple microscope configuration of: high NA microscope objective and tube lens (shown in Fig. 3.1a). We consider an aperture of NA=0.5, 1.0 and 1.49, respectively. d) Basis associated with a defocused PSF in the same microscope configuration (the simulated defocus is 300 nm) similar to Ref. [61] and e) basis associated with a vortex-phase modulation proposed in Ref. [13]. The elements necessary to measure rectilinear dipoles are shown enclosed in green. The last column shows the phase modulation (at the pupil plane) used to generate the basis. For the cases in a)-c) there is no modulation. For b), a defocused PSF can be understood as an in-focused PSF with a spherical modulation (the spherical term was computed from the exponential terms in Eq. (3.8)). In e) a vortex phase modulation was applied at the pupil plane.

longitudinal dipole aligned along z and the transverse dipoles aligned along x and y.

The examples in Fig. 3.6a-c correspond to the system illustrated in Fig. 3.1a of a high NA objective and a tube lens. The apertures used are NA=0.5, 1.0, and 1.49. The dipoles are immersed in a continuous medium of $n = 1.518$ with a wavelength $\lambda = 532$ nm. The pixel size is 52.7 nm and the window size is 17×17 pixels. Note that I_{11} and I_{23} are non negligible compared to I_0 only for the case of NA=1.49. This reflects the incapability of the simplest microscope configuration at low NA to distinguish the dipole's in-plane orientation. Furthermore, the fact that for low NA $I_{12} \approx I_0$ indicates that the system cannot differentiate between a longitudinal dipole and a completely depolarized one. Note also that when NA=1.49 the terms I_{11} and I_{23} are different from zero and orthogonal, but I_{21} and I_{22} remain equal to zero, implying that the system is sensitive to ξ only within modulus 180°. In other words, two rectilinear dipoles with components $(\pm\mu_x, \pm\mu_y, \mu_z)$ are indistinguishable. In the same case but with high NA, the term I_{12} is different from I_0 which for a rectilinear dipole means that the system can asses η. Based on this qualitative analysis of the Stokes-Gell-Mann PSF basis, it is possible to explain why from the PSFs shown in 3.3a the authors of Ref. [11] could report measurements of the angles η and ξ. The other examples shown in Fig. 3.3 illustrate two techniques in which the PSF of the rectilinear dipoles were shaped to access orientation information. In 3.3d the PSF basis associated with a defocused emitter is shown. This configuration was used to measure 3D oriented molecules [61], by inspecting the corresponding basis it is possible to notice that the six elements associated with rectilinear dipoles are all different and orthogonal (except I_{12} which is similar to I_0). This makes this approach suitable for measuring rectilinear emitters with the drawback that the PSF is enlarged by defocusing and in situations of high dipole density, the PSFs might overlap which could hamper the data analysis.

The last example in Fig. 3.3e is the basis generated by imprinting a vortex phase modulation at the pupil plane [13]. We observe that the basis elements are similar to the ones associated with the defocused PSF, shown in Fig. 3.3d, with the advantage that the associated PSF is smaller, but slightly bigger than the diffraction limited one in Fig. 3.3c.

We speculate that the examples illustrated in Fig. 3.3d-e could be the *simplest* configurations to measure the matrix of second moments of rectilinear dipoles with a high NA microscope objective. By simple configuration, we mean that the complete information of the emitter is contained in one PSF so there's no need to split the signal into more channels. Another aspect to consider is the modulation itself. In one case, the information can be accessed through a simple defocus, shown in Fig. 3.6d, while in the other, the vortex phase shown in Fig. 3.6e can be introduced using a transparent element that has to be carefully aligned.

Note that we have not addressed the measurement of elliptical dipoles. From the basis elements shown in 3.3, it is clear that the PSFs of these configurations do not provide complete information regarding the spin of elliptical dipoles. However, the presence of non-zero I_{31} and I_{32} suggest that the systems are sensitive to transverse elliptical dipoles (i.e. dipoles whose spin vector is perpendicular to z). Finally, for the examples shown in Fig. 3.6 qualitatively I_{21}, I_{22} presents similar features to I_{31},

I_{32}, which suggests that the corresponding Stokes-Gell-Mann parameters could be correlated if these configurations are used to measure elliptical dipoles.

3.3. Stokes-Gell-Mann basis for polarized measurements.

As mentioned in the previous section, several approaches recently proposed to measure the dipole orientation parameters involve splitting the signal into polarized channels. In this section, we discuss a group of these methods and describe the properties of the associated Stokes-Gell-Mann PSF bases. Let us start by explaining how to generate the basis of different polarized channels.

The electric field at the image plane of the dipole is given by $\mathbf{E}_{\text{Pup}} = \mathbf{G}_{\text{Pup}} \cdot \hat{\boldsymbol{\mu}}$. The dipolar emission descriptions described in section 3.8 and the PSF formation implied that the electric field was described in Cartesian coordinates. Therefore, the x/y-component of $\mathbf{E}_{\text{Pup}}$, denoted by $E^{x/y}_{\text{Pup}}$, correspond precisely to its linear polarization component along the x/y axis. This field can be also decomposed into its circular polarization components $E^{L/R}_{\text{Pup}} = \left(E^{x}_{\text{Pup}} \pm i E^{y}_{\text{Pup}}\right)/\sqrt{2}$. In practice, this is achieved by placing a linear polarizer and a QWP in the detection path as illustrated in Fig. 3.1b.

So far, we have only considered phase modulation to the signal at the back focal plane. However, it is possible to consider amplitude, phase and polarization modulations that could be described in terms of the *Jones Matrix*, **J**:

$$\begin{pmatrix} E^{x}_{\text{Mod}} \\ E^{y}_{\text{Mod}} \end{pmatrix} = \begin{pmatrix} J_{xx} & J_{xy} \\ J_{yx} & J_{yy} \end{pmatrix} \begin{pmatrix} E^{x}_{Pup} \\ E^{y}_{Pup} \end{pmatrix}. \tag{3.24}$$

In general, each component of this matrix can be complex representing an amplitude and phase modulation. In the special case where this transformation conserves energy, **J** is a unitary matrix. The electric field of the different polarization components, denoted by σ, of the modulated PSF can be written as $E^{\sigma} = \text{FT}(E^{\sigma}_{\text{Mod}})$. We use this expression to compute the basis elements I^{σ}_{j} shown in Eq. (3.23).

In Fig. 3.7 we illustrate four different configurations used to measure rectilinear dipoles in the context of SMOLM. Their corresponding Jones matrices are also shown. We merge the two polarization projections into a single array to analyze the system in terms of one basis.

The first example illustrates the simple separation of the signal into its horizontal and vertical linear polarization components [58]. In this work the authors performed ratiometric measurements. Nevertheless, from the basis it is possible to deduce some features of this scheme. Note that I^{V}_{11} is the negative of I^{H}_{11} and that, regardless of the dipole orientation, any combination of Stokes-Gell-Mann parameters should lead to positive PSFs. This is only possible by canceling out this negative contribution with I_0 or I_{12}, which have almost the same form and sign in both polarization channels. Consequently, there can be zero-value PSFs in one of the polarization channels. In

particular, the signal from horizontal/vertical dipoles will be sent mostly to the horizontal/vertical channel. This is not exclusive from this basis: whenever $I_j^{\sigma_1} \approx -I_j^{\sigma_2}$, where σ_i denotes the polarization channels, there will be an imbalance in the measured PSFs related to the dipole configuration. This energy imbalance is the working principle of ratiometric measurements, where the total energy contained in the different polarization channels is compared to deduce the orientation of rectilinear dipoles [58, 60].

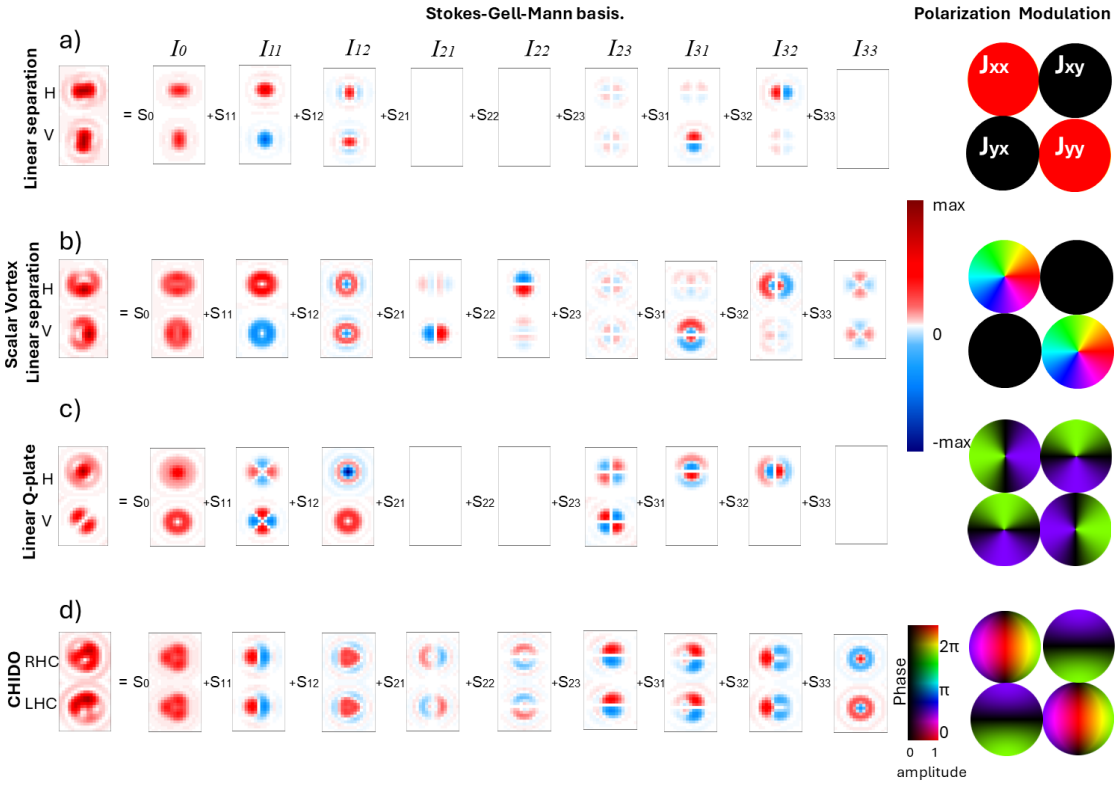

Figure 3.7.: Illustration of the Stokes-Gell-Mann basis for polarized channel configurations. The same rectilinear dipole PSF ($\eta = 45°, \xi° = 45$) is decomposed as a superposition of different basis elements representing different experimental configurations. a) Basis associated with the PSF of a simple microscope configuration with two linear polarization projections. b) Basis associated with a vortex phase modulation followed by two orthogonal linear polarization projections, based on the proposed method in Ding *et al.* [71]. c) Basis associated with modulation by a Q-plate followed by linear polarization projection [65, 66]. d) Basis associated with modulation by a SEO, with $c = \pi$, followed by the separation into the circular polarization channels [18].

The second example shown in Fig. 3.7b is a modified version of the system shown in Fig. 3.6e. The vortex phase plate is placed at the pupil plane of the microscope followed by a polarization separation into the linear horizontal and vertical channels. Note that the same features discussed for I_{11} in the previous basis are also valid for

this case. Similarly to the single-channel version, the elements I_{21} and I_{22} are different from zero and mutually orthogonal. In Ref. [71] the authors used this experimental configuration to measure the rotational mobility of single molecules. This information is only available if the complete matrix $\mathbb{m}$ is measured. We can notice that the basis elements related to rectilinear dipoles are all different (and qualitatively, they are also mutually orthogonal), which explains why it is possible to measure rotational mobility with this configuration.

The last two examples correspond to systems where polarization modulations at the pupil plane were performed. Fig. 3.7c illustrates the basis and the corresponding Jones Matrix associated with a vortex half-wave plate, also known as a Q-plate. This configuration has been implemented to measure the in-plane orientation of nanorods [66] and the rotational dynamics of single molecules [65]. This mask can be understood as an array of half-wave plates whose axis rotates as 1/2 of the azimuthal angle. Note that in this case S_{21} and S_{22} are inaccessible, despite the great contrast between I_0, I_{12} and I_{23} in the horizontal channel. This last condition implies that a longitudinal dipole is expected to be distinguishable from a fully depolarized dipole.

Finally, in Fig. 3.7d we illustrate the characteristic basis related to Coordinate and Height super-resolution imaging with Dithering and Orientation (CHIDO) microscopy [18]. The modulation is achieved by placing an element referred to as a stressed-engineered optic (SEO) [18] followed by the separation of the modulated signal into its circular polarization components. This element is characterized by the following Jones Matrix

$$\mathrm{J}(u)_{SEO} = \cos\frac{cu}{2}\begin{pmatrix} 1 & 0 \\ 0 & 1 \end{pmatrix} + i\sin\frac{cu}{2}\begin{pmatrix} \cos\varphi & -\sin\varphi \\ -\sin\varphi & -\cos\varphi \end{pmatrix}, \tag{3.25}$$

where (u,φ) are the normalized radial (such that $u = 1$ at the pupil's edge) and azimuthal polar coordinates at the pupil plane, and c coefficient that depends on the used pupil radius. Compared to all the previous systems, we notice that the basis elements associated with the spin are different from zero and their amplitudes are comparable with the rest of the elements. Due to the parity and symmetries present in each element, we can qualitatively infer that those functions form a linearly independent basis for the PSFs of elliptical dipoles. This last feature is discussed in the next section.

Note that it is possible to compute the Stokes-Gell-Mann PSF basis for systems where the measurement is performed at the pupil plane or for ratiometric techniques. In the first case, the basis would describe the pupil patterns (for instance those in Fig. 3.2) as a superposition of nine different pupil functions. In ratiometric methods, the signal in each channel can be seen as a superposition of nine numbers weighted by the Stokes-Gell-Mann parameters. The complete Stokes basis can be constructed by merging the basis of each channel. We do not discuss in detail these or other configurations, because the scope of this thesis is to perform measurements at the image plane and extract physical information from the measured PSF. However, it is important to note that the Stokes-Gell-Mann formalism is inherent to the study of 3D oriented optical dipoles regardless of the experimental configuration, and can be

used to evaluate the sensitivity of optical systems to specific physical quantities of 3D oriented dipoles. In the next section, we discuss the Stokes-Gell-Mann formalism in the context of the Fisher information matrix.

3.4. Fisher Information Matrix

In this section, we use the Fisher Information Matrix (FIM) formalism to quantify the capabilities of a microscope to access the Stokes-Gell-Mann parameters. One of the main advantages of decomposing the PSF in terms of the Stokes parameters is that we have a linear relation between the physical parameters of interest and the intensity I^σ measured in the camera:

$$I^\sigma = I_b^\sigma + S_0 I_0^\sigma + \sum_j S_j I_j^\sigma, \tag{3.26}$$

where σ denotes the polarization channel, I_b^σ is the background, I^σ is the probability distribution of detecting a signal photon in the camera. This distribution depends on the dipole $\hat{\boldsymbol{\mu}}$ (or equivalently the Stokes-Gell-Mann parameters) and its position in the sample volume. Let us assume we have in-focus dipoles localized at the origin in the sample plane and a constant background I_b. The measured intensity distribution in the polarized channel σ over the pixel $\mathbf{x}$ is $I(\mathbf{x},\sigma,\vec{S}) = I_b + S_0 I_0(\mathbf{x},\sigma) + \vec{S}\cdot\vec{I}(\mathbf{x},\sigma)$, where we wrote the previous sum as the dot product between a vector $\vec{S}$ containing the Stokes-Gell-Mann parameters (except S_0) and $\vec{I}$ containing the corresponding PSF basis elements. Therefore, the probability of photon detection in the polarized channel σ over the pixel $\mathbf{x}$ is given by

$$P(\mathbf{x},\sigma,\vec{S}) = \frac{I(\mathbf{x},\sigma,\vec{S})}{\langle I(\mathbf{x},\sigma,\vec{S})\rangle_{\mathbf{x},\sigma}}, \tag{3.27}$$

where the $\langle\cdot\rangle_{\mathbf{x},\sigma}$ represents a sum over all the pixels $\mathbf{x}$ and polarization channels σ. In other words, $\langle\cdot\rangle_{\mathbf{x},\sigma}$ is the total number N of captured photons. We can notice that this quantity depends on the values of the Stokes parameters. One might wonder if there are experimental conditions for which the total captured power is independent of the Stokes- Gell-Mann parameters. In the case of rectilinear non-wobbly dipoles, this is equivalent to asking the experimental conditions under which the total captured power is independent of the dipole's 3D orientation.

An interesting case, especially in SMOLM where the fluorophores are usually immersed in water and observed with an oil immersion objective, is the situation of a dipole in a medium of index $n_0 = 1.33$ close to the interface with a second medium of index $n_1 = 1.518$. To answer this question we utilize Eq. (3.11) to compute the electric field at the pupil plane for the same dipole $\hat{\boldsymbol{\mu}}$ varying the angle η from 0 to 90° and compute the total captured power over the pupil plane $\Phi = \langle \mathbf{E}^* \cdot \mathbf{E}\rangle_{\text{Pup}}$. In Fig. 3.8 we show the dependence of Φ as a function of both η and NA. In the case of rectilinear dipoles immersed in water, the optimal NA that captures the power is NA$\approx$ 1.336 slightly above the limit with the region containing the *supercritical angle*

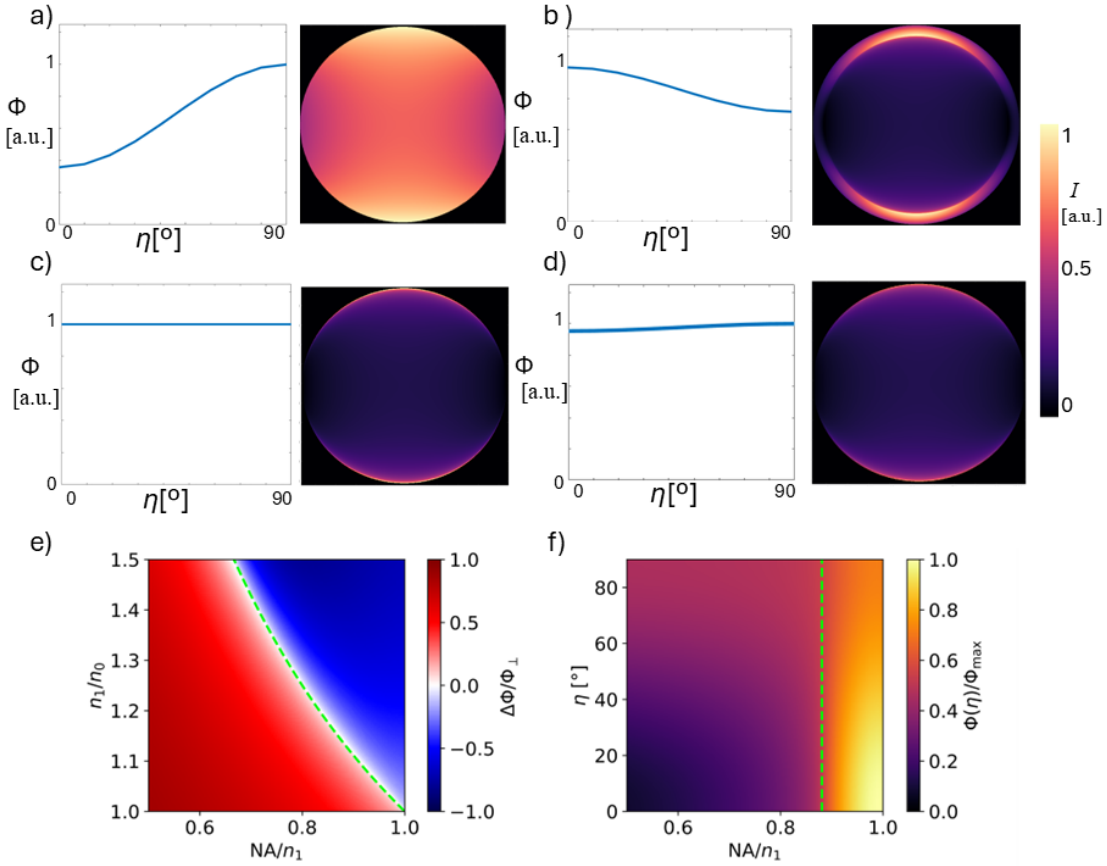

Figure 3.8.: a) Right, Φ as a function of η normalized to the maximum captured value. We consider a water-oil interface with NA=1.0. Left, intensity distribution at the pupil plane of a dipole $\hat{\boldsymbol{\mu}} = (1,0,0)$ under the same physical conditions. b) Same as in a) considering NA=1.49. Notice how there is an asymmetry in the behavior of Φ due to the efficiency of the transmission of the evanescent contributions for different orientations. c) Same as a) and b) but with NA=1.336 corresponding to a constant power captured by the objective. In d), the case where the supercritical angle contributions are removed is shown. This is equivalent to having an NA=1.33, leaving Φ fairly constant. e) Relative difference between the powers captured by the microscope for a transverse and a longitudinal dipole ($\Phi_\perp, \Phi_z$, respectively), as a function of the normalized NA with respect to the immersion liquid's refractive index and the index mismatch between the embedding medium and the immersion liquid. f) Total power for a non-wobbling emitter with an off-plane angle η for different numerical apertures given an index mismatch corresponding to oil/water. (e)-f)) The green line corresponds to NA = n_0.

emission (SAE). In experimental conditions it is easier to remove those contributions by placing an iris diaphragm at the pupil plane. We also show Φ as a function of η in those conditions and observe that the maximum variation on the power around 5%.

In a more general scenario, we consider the case of arbitrary n_0, n_1 and NA. It is easy to see by symmetry arguments that this power depends only on the angle η following the simple sinusoidal relation $\Phi = \Phi_\perp \sin^2\eta + \Phi_z \cos^2\eta$, where $\Phi_\perp$ and Φ_z correspond to the two extreme cases of a dipole oriented transversely to the axis of the microscope, say, in the x direction, and one oriented parallel to the microscope axis.

Let us assume that we are in conditions where the total power is independent of the Stokes-Gell-Mann parameters and constant background $I_b = 0$. This implies that $S_0\langle I_0^\sigma\rangle_{\mathbf{x},\sigma} + \sum_j S_j\langle I_j^\sigma\rangle_{\mathbf{x},\sigma}$ is constant and equals the total power. From the definition of I_j^σ is clear that I_0 is always positive and $S_0\langle I_0^\sigma\rangle_{\mathbf{x},\sigma}$ is proportional to the total radiated power. Therefore, $\langle I_j^\sigma\rangle_{\mathbf{x},\sigma} = 0$ except for I_0. This is illustrated in Fig. 3.6a-c, where I_{12} seems to be positive for low NA, but, as the NA increases the total captured power becomes independent of $\vec{S}$ due to the secondary rings with negative values that contribute to fulfill the condition $\langle I_j^\sigma\rangle_{\mathbf{x},\sigma} = 0$ except for I_0. Note that this condition is independent of the modulation performed to the signal or the polarization splitting. It is therefore convenient to use the normalized Stokes-Gell-Mann parameters ($s_j = (\sqrt{3}/2)S_j/S_0$) to describe the probability distribution of photon detection:

$$P(\mathbf{x},\sigma|\vec{s}) = \frac{I(\mathbf{x},\sigma)}{\langle I(\mathbf{x},\sigma)\rangle_{\mathbf{x},\sigma}} \approx \frac{I_b/N_s + I_0(\mathbf{x},\sigma) + \vec{s}\cdot\vec{I}(\mathbf{x},\sigma)}{N/N_s}, \tag{3.28}$$

where $N = \langle I_b\rangle_{\mathbf{x},\sigma} + N_s$ is the total measured number of photons (since I_b is the average number of background photons per pixel). To simplify the equation we integrated the factor $\frac{\sqrt{3}}{2}$ in the term $\vec{I}$, and we used the relations $S_0\langle I_0\rangle_{\mathbf{x},\sigma} = N_s$, the condition $\langle I_0\rangle_{\mathbf{x},\sigma} = 1$ and $\langle I_j\rangle_{\mathbf{x},\sigma} = 0$, the latter resulting from using NA = n_0. That is, the use of NA = n_0 makes this probability approximately a linear function of $\vec{s}$ (the vector containing the normalized Stokes-Gell-Mann parameters), which simplifies the analysis that follows.

Finally, the elements of the Fisher information matrix $\boldsymbol{J}^{(\vec{s})}$ for the Stokes Gell Mann parameters are given by [72]

$$J_{jk}^{(\vec{s})} = N\left\langle \frac{\partial_{s_j}P\,\partial_{s_k}P}{P}\right\rangle_{\mathbf{x},\sigma} \approx N_s\left\langle \frac{I_jI_k}{I_b/N_s + I_0 + \vec{s}\cdot\vec{I}}\right\rangle_{\mathbf{x},\sigma} = N_s\langle\langle I_jI_k\rangle\rangle, \tag{3.29}$$

where $\langle\langle I_jI_k\rangle\rangle$, denotes an inner product between two PSF components I_j and I_k, defined as the sum over all pixels and polarization channels with a non-negative weight function given by $1/(I_b/N_s + I_0 + \vec{s}\cdot\vec{I})$ (which depends on the Stokes Gell Mann parameters to be retrieved and on the level of background intensity). In the previous definition of the Fisher information matrix, we have considered the Poissonian nature of photon statistics. In the regime of a large photon number, we can consider Gaussian statistics and consequently, the definition of the Fisher information matrix changes to

$$J_{jk}^{(\vec{s})} = N\left\langle \frac{\partial_{s_j} P \partial_{s_k} P}{\sigma^2(\mathbf{x})} \right\rangle_{\mathbf{x},\sigma} \approx \frac{N_s^2}{N}\left\langle \frac{I_j I_k}{\sigma^2(\mathbf{x})} \right\rangle_{\mathbf{x},\sigma}, \tag{3.30}$$

where $\sigma^2(\mathbf{x})$ is the variance at each pixel $\mathbf{x}$.

In both regimes, the FIM elements are proportional to the inner product between the basis elements $\langle\langle I_j I_k\rangle\rangle$; if this quantity is zero for $j = k$, it would be impossible to extract any information about the corresponding Stokes-Gell-Mann parameter. On the other hand, if $\langle\langle I_j I_k\rangle\rangle = 0$, for $j \neq k$, i.e. if the FIM is a diagonal matrix, the Stokes-Gell-Mann parameters are not correlated, and the inverse of the diagonal elements correspond to the precision limits to which we can estimate the corresponding parameters.

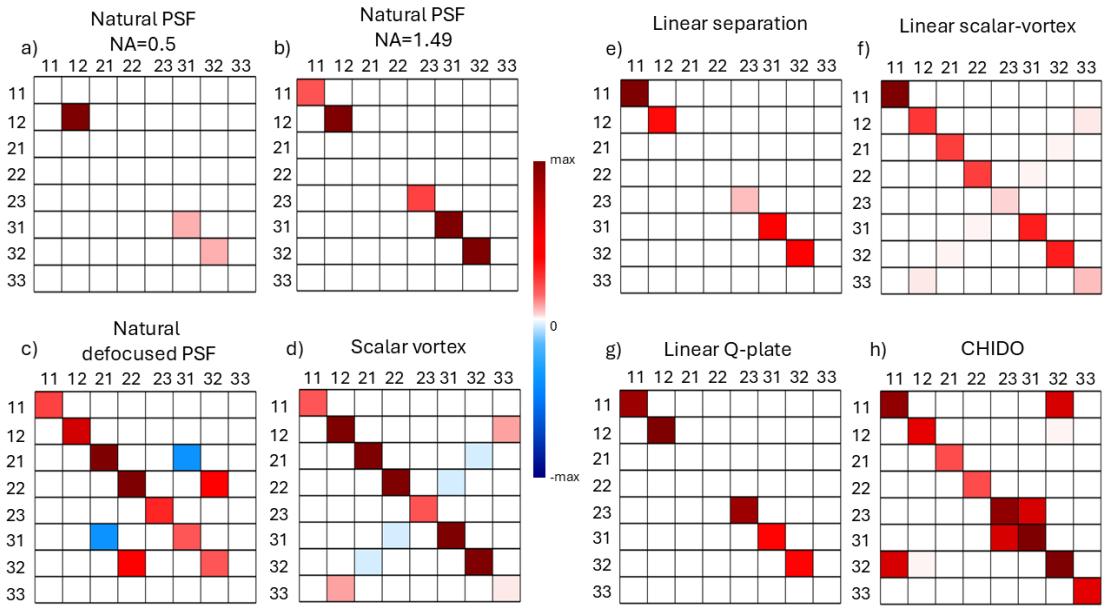

Figure 3.9.: Fisher Information Matrix. From a) to d) we illustrate the FIM associated with the configurations shown in Fig 3.6 a), c) d) and e) respectively. From e) to h) we show the FIM describing the systems illustrated in Fig. 3.7 a), b), c) and d), respectively.

In Fig. 3.9 we show examples of the FIM computed with Eq. (3.29) (considering $I_b = 0$ and $\vec{s} = \vec{0}$). As mentioned earlier, the FIM depends on $\vec{s}$; however, from the specific case $s = \vec{0}$ we can discriminate experimental configurations suitable for measuring all the Stokes-Gell-Mann parameters or a subset of them.

We corroborate that the simple configuration of high NA objective (NA=1.49) and tube lens can only measure S_{11}, S_{12}, S_{23}, S_{31}, and S_{32}. For the low NA case (NA=0.5) only three Stokes Gell Mann parameters are accessible, the corresponding FIM being shown in Fig. 3.9a-b. On the other hand we can see that the defocused PSF can give access to all Stokes-Gell-Mann parameters except S_{33}. Note that S_{21} and S_{31} are anti-

correlated whereas S_{22} and S_{32} are correlated. However, the rest of the variables are uncorrelated, which makes this method the simplest configuration to measure rectilinear dipoles, at the price of a large PSF. A similar performance is observed for the phase vortex where small correlations are present while providing *little information* on the s_{33} parameter. In this case, however, the PSF is smaller compared to the defocused one. In the case of the FIM associated with polarization channel configurations, the only two configurations that can provide full information are the linear polarized vortex phase and CHIDO with some correlated parameters. Interestingly, the unmodulated high-NA PSF (with or without polarization separation) and the polarized Q-plate PSF perform, in theory, similarly. It is important to recall that this simple expression of the FIM is valid only in situations without supercritical angle emission. The FIM could change depending on the specific dipole $\vec{s}$ in the presence of those contributions.

3.5. Final remarks

We described the dipole emission captured with a microscope, illustrated the numerical computation of the dipole's vectorial PSF and showed numerical results that agree with the literature. We defined the concept of Stokes-Gell-Mann PSF basis to characterize the capabilities of any microscope for measuring elliptical dipoles. We explained how to compute and interpret the elements of the Stokes-Gell-Mann PSF basis. We defined the Fisher information matrix associated with the Stokes-Gell-Mann parameters and showed that the special case of NA= n_0 and $\vec{s} = 0$ provides insights about the limitations of different microscope configurations for measuring dipole sources. We applied this formalism to explain and study previous works measuring rectilinear dipoles. These results are discussed in a recent publication [23].

Contrary to the common PSF formation models (for rectilinear dipoles), where the parameters of interest are the angles (η, ξ, δ) describing the dipole orientation, here we propose a linearized form that relates the Stokes-Gell-Mann parameters to a basis of functions that are linked to specific physical properties of dipolar sources. There is an alternative formulation [33, 57] that linearly relates the second-moment matrix elements $\mathbb{m}_{ij}$ to the PSF. However, that model does not account for elliptical dipoles and is not based on the natural decomposition of the second-moment matrix in terms of an orthogonal basis of matrices. In Chapter 4, we exploit the mathematical properties of the Stokes-Gell-Mann PSFs basis (inherited from the decomposition into an orthogonal basis of matrices) to construct a parameter retrieval algorithm used to analyze data efficiently.

4. C-3POL: circular polarization decomposition for measuring 3D oriented dipoles.

Sommaire

4.1. Introduction. 71
4.2. Circular vs Linear polarization separation. 72
4.3. Stokes-Gell-Mann Basis and FIM for the circular projection configuration. 76
4.4. Implementation. 77
4.4.1. Registration. 79
4.4.2. Initial 2D localization of dipole emitters. 82
4.4.3. Background estimation. 82
4.4.4. Stokes-Gell-Mann parameter estimation. 83
4.4.5. Accurate Stokes-Gell-Mann parameter estimation and correction to the initial 2D location. 84
4.4.6. 3D localization of dipole emitters. 86
4.5. Numerical studies. 90
4.5.1. Continuous medium and fully polarized rectilinear dipoles. . . . 90
4.5.2. Continuous medium and fully polarized elliptical dipoles. 94
4.6. Final remarks 97

4.1. Introduction.

In this chapter, we show that dipoles with any ellipticity can be measured by simply separating the dipole's signal into its circular polarization components and measuring their PSFs. We start by showing some features of the circular polarization components of dipole radiation. We explain the general experimental configuration for the dipole detection, the data processing which is based on the linear relationship between the PSFs and the Stokes-Gell-Mann parameters, and the expected accuracy and bias based on Monte Carlo simulations. We discuss both the advantages and limitations of this approach.

4.2. Circular vs Linear polarization separation.

Recent PSF engineering approaches in SMOLM and SMLM used spatial light modulators to imprint arbitrary phase modulations to the dipole signal at the pupil plane. In particular, some phase masks have been proposed based on optimization algorithms that maximize the Fisher information associated with the axial dipole coordinate for 3D localization [69, 73] or the directional and spatial coordinates for simultaneous 3D localization and orientation of fluorophores [67]. In those experiments, one or two orthogonal linear polarization components are modulated. One might wonder if modulating the linear components is advantageous over imprinting a phase pattern on the circular polarization components or vice versa. In Fig. 4.1 we show amplitude and phase distributions of the linear and circular components at the pupil plane for different rectilinear dipoles.

Note that the characteristic presence of a doughnut-like shape (clearly seen in the amplitude associated with a longitudinal dipole) is explained by the presence of two optical vortices of opposite signs (naturally linked to zeros on the field's amplitude) of the circular polarization components. In the linear basis, this zero can be seen as the result of the two polarization components having orthogonal lines of zeros in the amplitude and a phase discontinuity of π. These zeros are caused only by the projection on a linear basis, but they are not present in the dipole radiation pattern. From this point of view, the circular projection represents a more natural separation of the dipole field components.

All the PSFs were simulated assuming that the geometrical array's center corresponds to the actual 2D location of the emitter. It is clear that the maximum intensity of the PSF is not located at that position, especially for a small value of η. The problem of precise 2D localization of the emitters is discussed in the next section.

From now on we restrict the analysis to separation in the circular components. Note that the position of the optical vortex at the pupil plane depends on the rectilinear dipoles' orientation. For longitudinal dipoles, this vortex is at the center, whereas for transversal dipoles it is at the border. Another feature of this decomposition is that for a given off-plane angle η, any change in the azimuthal angle ξ can be seen as a rotation of this vortex around the pupil center. Therefore, the pattern components at the pupil and at the image plane depend only on the value of η. In contrast, variations on ξ can be seen as rotations of these intensity pattern.

Note that variations on the axial coordinate of the dipole can be seen as counter-rotations in the PSF pair. This counter-rotation is a consequence of the difference between the signs of the vortices in the circular components and provides axial localization information. Needless to say, in the PSFs corresponding to linear separation those features are not present. Furthermore, the presence of π phase jumps at the pupil plane as well as lines of zero amplitude in the linear polarization components makes it difficult to intuitively think of a phase pattern that could increase the amount of directional and axial position information in the PSF for all the 3D configurations. On the other hand, the presence of a single vortex phase pattern in the circular components naturally leads to the question of whether a phase mask with similar symmetries

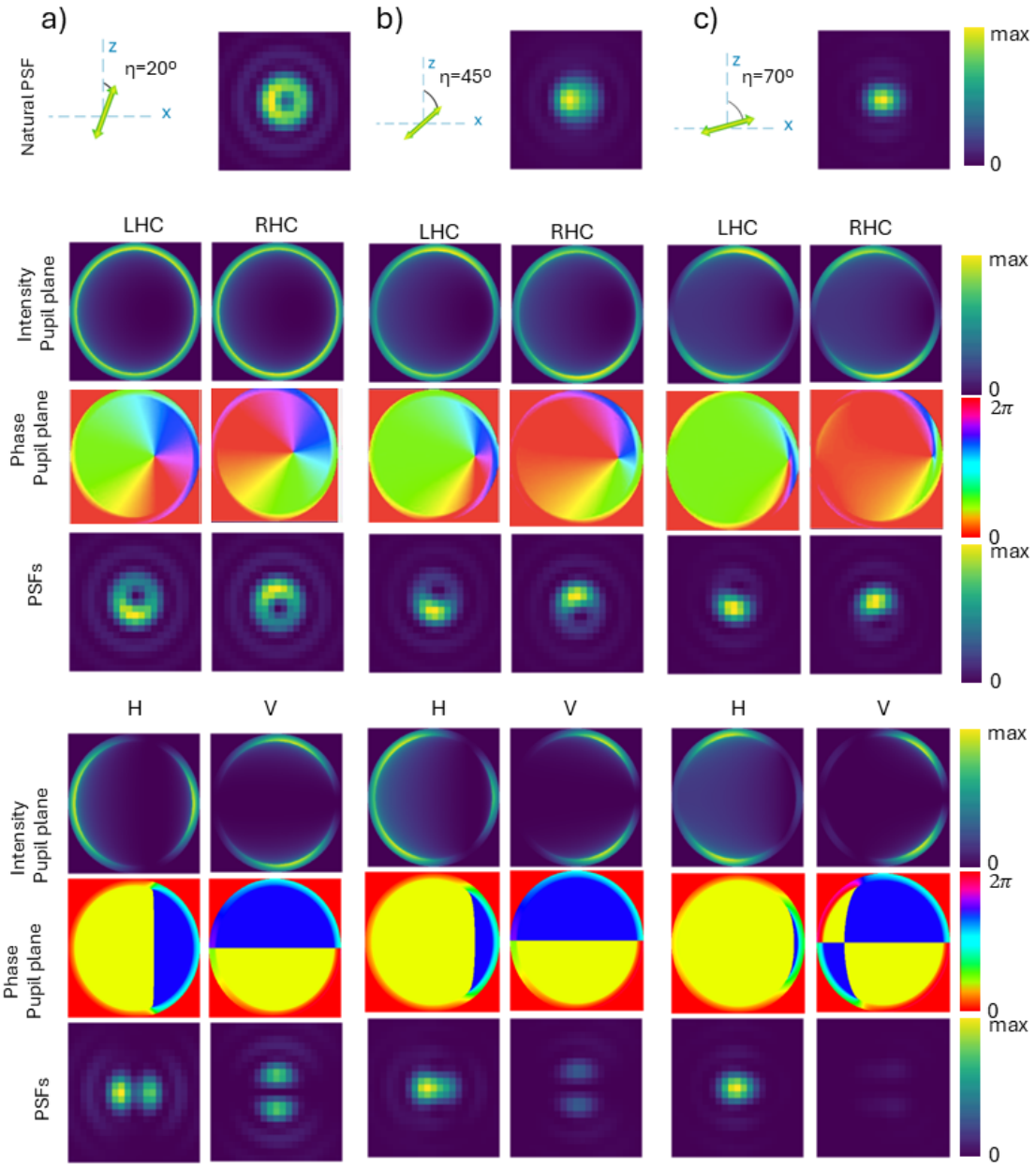

Figure 4.1.: Top line: Dipole representation and natural PSF for a rectilinear dipole with an angle η of a) 20°, b) 45° and c) 70°. Second group of images: Amplitude and phase at the pupil plane and PSF in the LHC and RHC polarization channels. Third group of images: Amplitude and phase at the pupil plane and PSF in the H and V polarization channels.

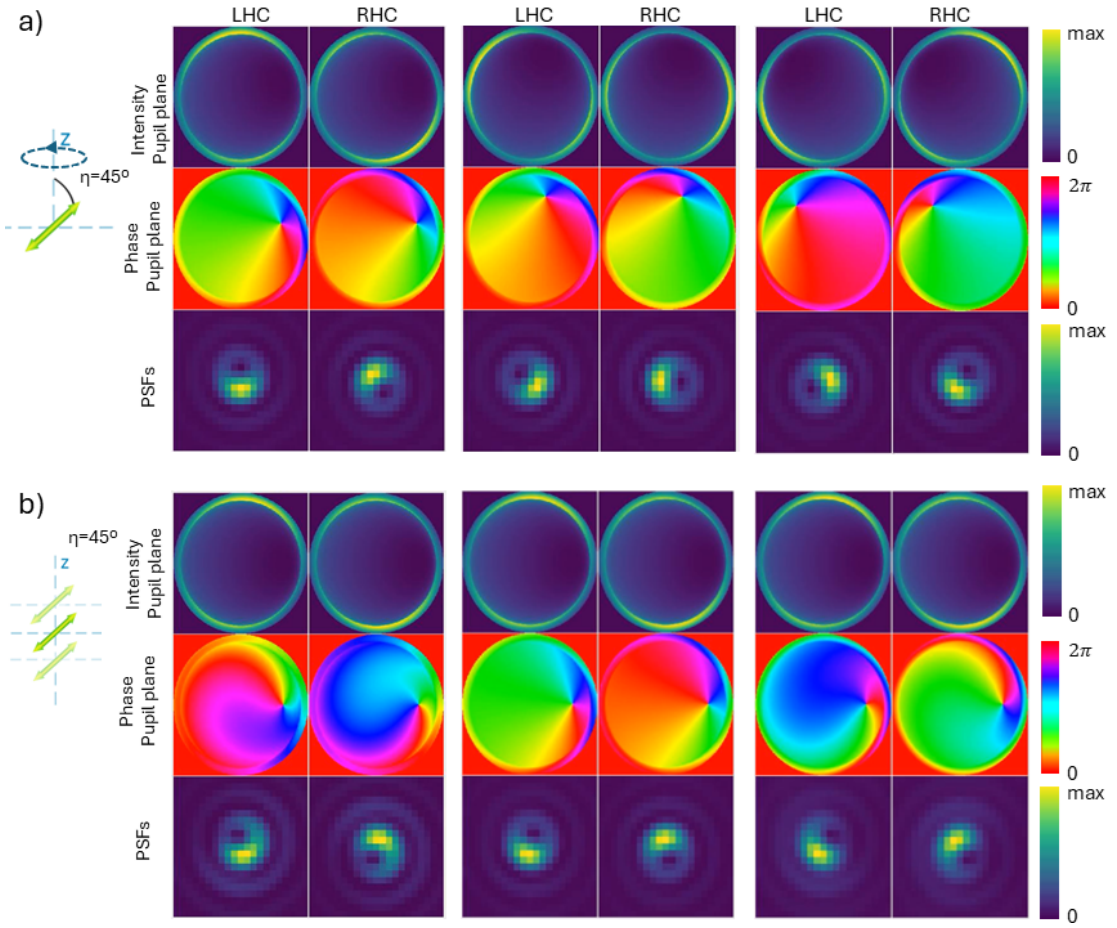

Figure 4.2.: Illustration of a) the rotation of the PSF (projected on the LHC/RHC basis) according to variations of ξ for a constant off-plane angle $\eta = 45°$: from left to right $\xi = 20°, 70°, 130°$. b) Illustration of the counter-rotation of the PSF pair with a defocus of, from left to right $z = -200\text{nm}, 0\text{nm}, 110\text{nm}$. In both cases, we consider a dipole deposited on a water-glass interface.

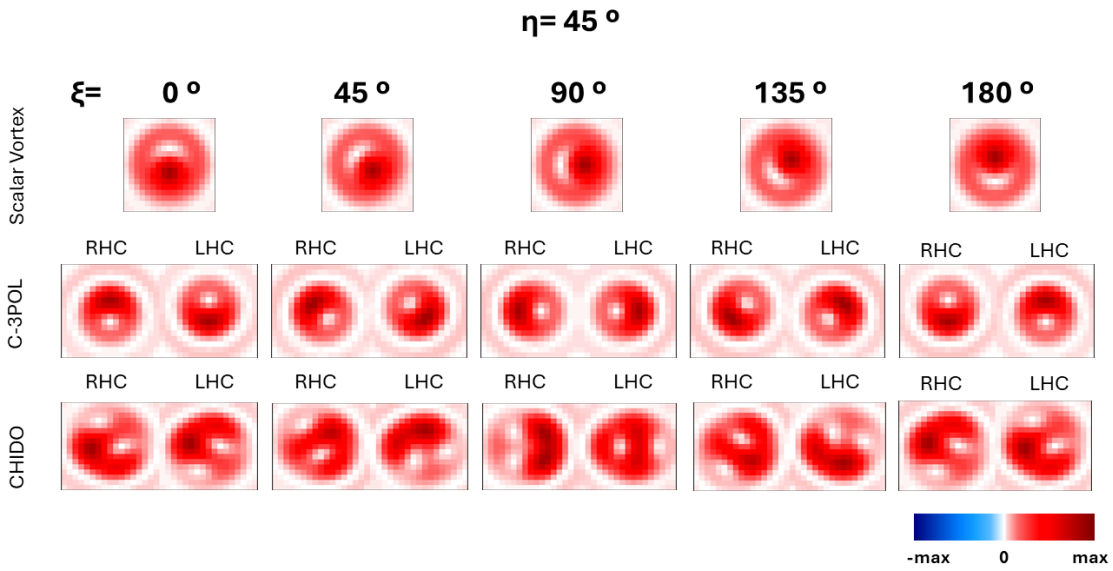

Figure 4.3.: PSF comparison. The PSF of a rectilinear dipole with $\eta = 45°$ and in-plane angle of $\xi = 0°, 45°, 90°, 135°$, and $180°$ is simulated for the cases of scalar vortex modulation, C-3POL and CHIDO. The dipole at $\lambda = 532$ nm is on a water-glass interface located at the focal plane of an objective of NA=1.33. The pixel size is 52.7 nm.

could increase the amount of directional and axial information while keeping the PSF's size small and with similar features like the ones illustrated in Fig. 4.1 and 4.2. From now on, we refer to as Circular 3D polarimeter (or C-3POL for short) to the circular component separation of the dipole PSF. The simplest modulation that leads to PSFs with the same symmetries present in C-3POL is the scalar vortex modulation applied to both polarization components [13]. Another configuration where the presence of optical vortices leads to PSFs whose shape depends mostly on η is CHIDO [18]. We present an example of these features in Fig. 4.3. In scalar vortex and C-3POL configurations, the PSF shape only depends on η and it rotates according to the angle ξ. In CHIDO, the PSF does not depend only on η, but it is clear that the PSFs associated with $\xi = 180$ can be obtained by applying a horizontal reflection to the PSF associated with $\xi = 0$. The same property can be seen for PSFs related to $\xi = 45$ and $\xi = 135$. An important feature shared by C-3POL and CHIDO is the equal distribution of power in the RHC and LHC channels. Contrary to other PSF engineering techniques proposed to measure rectilinear dipoles, there is no energy exchange between the polarized detection channels. This property is important in the presence of background, where the information contained in low-intensity PSFs may be compromised by noise. In Fig. 3.7 presented in Chapter 3, we illustrate the Jones Matrix associated with the SEO expressed in the linear polarization basis. If we now include the QWP in the Jones matrix we observe a matrix with vortex phase modulation

in all its components, as shown in Fig. 4.4. We speculate that these types of symmetries in the phase/polarization modulation might explain why CHIDO and the scalar vortex are the only schemes (among the configurations discussed in the previous chapter) that can encode the complete dipole 3D orientation information in the PSF. Since the circular components of the natural PSF already seem to contain all the directional information and axial dipole position, we speculate that any routine that seeks to maximize the amount of directional information should be performed on the circular components. We now study in more detail the properties of C-3POL.

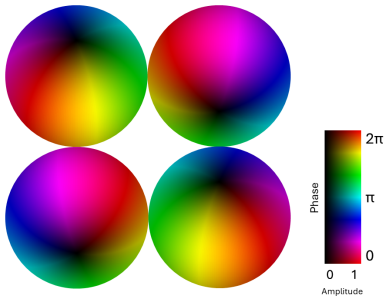

Figure 4.4.: Jones matrix representation of the SEO + QWP at the pupil plane. Note the presence of optical vortices in all the components.

4.3. Stokes-Gell-Mann Basis and FIM for the circular projection configuration.

The computed Stokes-Gell-Mann basis and FIM (considering the nine Stokes-Gell-Mann parameters) associated with the circular polarization components are shown in Fig. 4.5. This simulated basis accounts for the experimental conditions described in the following section and in the next chapter: the emitters are assumed to be in-focus and immersed in a continuous medium of $n = 1.518$, with an effective collection aperture of NA= 1.26, a wavelength of $\lambda = 532$ nm. The basis elements are rectangular arrays that represent the camera pixels, with a pixel size of 52.7 nm.

Surprisingly all the basis elements associated with C-3POL are different from zero and almost all are orthogonal (except I_0 and I_{12} as illustrated in the FIM). We show the basis corresponding to the natural vectorial PSF, and the natural PSF separated in the linear components. We also show the corresponding FIM computed with Eq. (3.29) including the term S_0 to show that there is some correlation between S_{11} and S_0. Note that in the other configurations capable of measuring elliptical dipoles (discussed in Chapter 3) there are more than two pairs of strongly correlated Stokes parameters. Despite this possible source of bias, we decided to experimentally explore the circular separation, mainly due to the intrinsic simplicity of the implementation. It is sufficient to place a QWP and linear polarizers along the detection path. This represents a significant simplification compared to the use of phase or polarization modulation: there is no need to consider extra aberrations due to those elements and

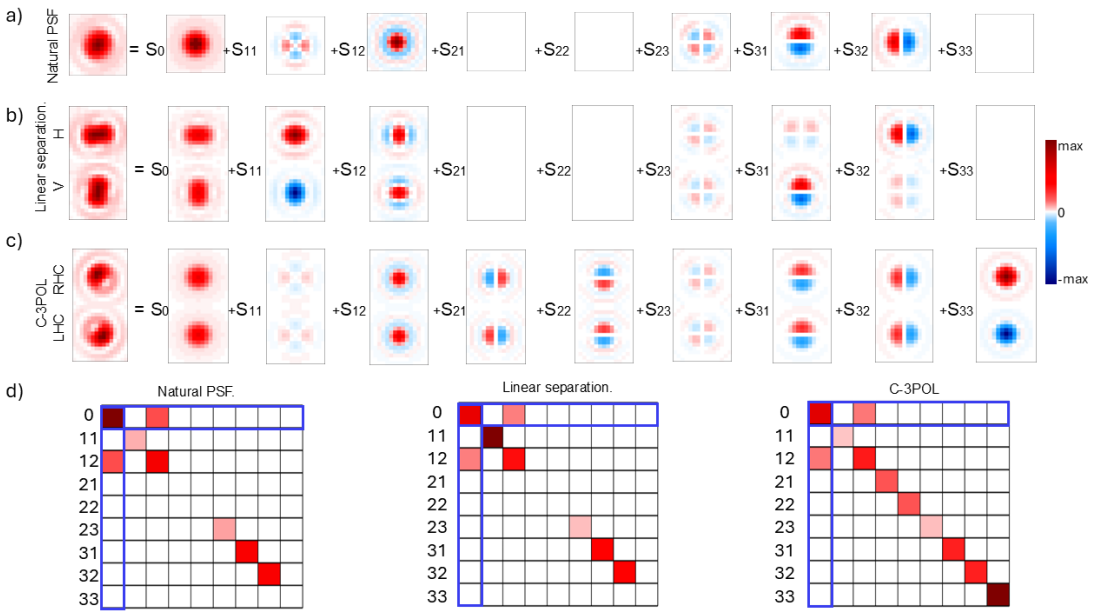

Figure 4.5.: Comparation between the simplest microscope configurations. a) Basis related to the natural PSF basis, b) to the separation in linear polarization channels and c) to the separation in circular polarization channels. d) Corresponding FIM. We assume in-focus emitters in a medium of index $n = 1.518$, a collection aperture NA= 1.26, a wavelength $\lambda = 532$ nm and a pixel size of 52.7 nm.

the setup is also robust to misalignment because the QWP is a thin optical element with no spatial variation. As far as we know this is the first time this scheme is used to measure 3D oriented elliptical dipoles in imaging configuration. Some simulations of the circular separation were made in a work comparing the performance of some configurations for SMOLM [74].

4.4. Implementation.

In this section, we explain the detection part of the optical setup that we use for measuring optical dipoles. The illumination part and the particularities of the different applications (nonparaxial polarimetry and single molecule fluorescent orientation microscopy) are discussed in the following chapters. For now, let us focus only on the measurement part illustrated in Fig. 4.6.

The signal from the sample is collected by a high NA objective ×100 and then magnified by a factor of 1.25 with a telescope, so that the object at the sample plane is being magnified by a factor ×125. The separation into the circular polarization components occurs close to the Fourier plane of the telescope with a combination of a QWP and a Wollaston prism (WP). This prism separates any incoming beam into its linear polarization **x**-**y** components. The QWP fast axis is oriented 45° to the **x** axis. The two signals diverge from the WP with an aperture angle of 1°. The use of the WP

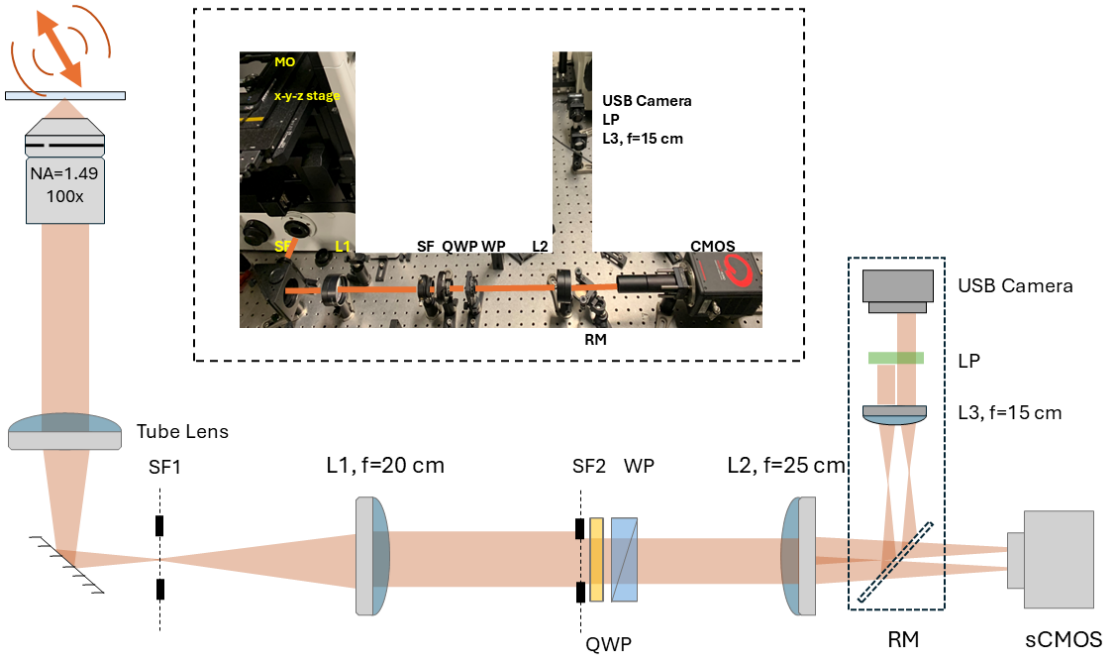

Figure 4.6.: Photography and schematic of the detection path. A microscope objective (MO) of NA=1.49 is placed in a reflection configuration in a commercial optical microscope. It collects the signal from a sample mounted in an x-y-z piezo stage. In the image plane, (right in front of the microscope exit) a spatial filter (SF1) is placed to limit the field of view (FOV). The signal is reflected by a 2 in mirror and redirected to a telescope of magnification $M = 1.25$ (L1 and L2 have focal lengths of f=20 cm and L2 f= 25 cm respectively). A second spatial filter (SF2) is placed at the Fourier plane that coincides with the focal plane of L1 and L2. SF2 controls the effective collection NA of the system. Close to the Fourier plane, a QWP and a WP are placed to separate the signal into its circular polarization components. Between L2 and the camera, a retractable mirror is placed to redirect the signal to a USB camera used to image the Fourier plane.

with a small aperture angle allows the measurement of two replicas of the same FOV in one camera, the effective FOV diameter being ~ 36 μm. The FOV diameter strongly depends on the focal lengths of the telescope lenses and the WP aperture angle, in this case L1 has a focal length of f = 20 cm and L2 has a focal length of f = 25 cm. The total extension of the detection path, measured from the first image plane to the sCMOS sensor is 90 cm.

Between L2 and the camera, a retractable mirror is placed to send the signal towards a second USB camera used to image the Fourier plane. This part is composed of a lens L3 of f = 15 cm and a linear polarizer to filter one of the components. This second part is only for calibration purposes. By imaging the pupil plane, it is possible to quantify the effective numerical aperture of the system, which can be controlled with the second spatial filter (SF2).

4.4.1. Registration.

Before imaging the sample of interest, we perform calibration measurements to compute the relation between the coordinates of the PSFs associated with the same emitter in both polarization channels. For methods in SMLM and SMOLM using multichannel measurements, it is well known that the linear transformation that best describes the relation between the coordinates of the same emitter in those channels is an *affine transformation*. This transformation accounts for relative translation, rotation, magnification and shearing of the two replicas of the same FOV [60]. The origin of those distortions can be related to the separation by the WP which modifies the actual trajectory of the two polarization components that L2 redirects to the camera. As we are restricted to measuring a reduced part (~ 36 μm of diameter) of the complete FOV associated with our microscope, we do not expect to observe strong distortions such as FOV-dependent aberrations that could require considering higher-order transformations [75].

To characterize the affine transformation we place a sample of sparse emitters whose PSFs' geometical centers can be associated with the actual (x, y) position of the emitters. In Fig. 4.7a we illustrate two replicas of the same FOV captured by the camera. Those PSFs are associated with fluorescent beads (568 nm) of 100 nm in diameter deposited on a coverslip and immersed in water.

To compute the affine transformation we independently localize emitters in the two regions $\mathbf{r}_1$ and $\mathbf{r}_2$ shown in Fig. 4.7a. Both coordinate systems have the same origin at the upper left corner of the complete image. We binarize each region according to the intensity values to only take into account the brightest emitters. Then, we find the position of each emitter with the *regionprops* function in Matlab and a homemade algorithm that discards multiple localizations related to the same PSF (since it can happen that small variations of the intensity pattern around a PSF, such as diffraction rings or nearby PSFs, cause spurious localizations, especially for low SNR measurements). Based on the relative differences of the (x, y) coordinates for both regions, we can match the pair of measured coordinates. Note in Fig. 4.7c-d the computed PSF centroid. With the set of matched pairs of coordinates, we can invert the matrix

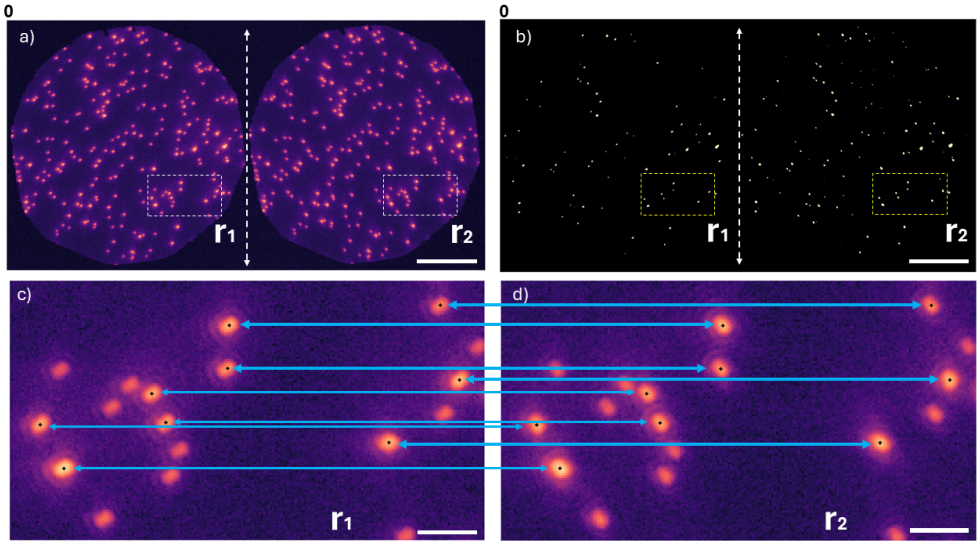

Figure 4.7.: Calibration of the affine transformation. a) Sparse sample of fluorescent beads. We independently localize the emitters in each region $\mathbf{r}_1$ and $\mathbf{r}_2$ (scale bar 9.3 μm). b) Binarized image showing the brightest emitters. c)-d) Zoomed-in regions showing the same emitters and the corresponding estimated centroid (where the intensity is in logarithmic scale and the scale bar corresponds to 1.4 μm).

multiplication problem:

$$\begin{pmatrix} \mathbf{x}_2 \\ \mathbf{y}_2 \end{pmatrix} = \begin{pmatrix} a & b & c \\ d & e & f \end{pmatrix} \begin{pmatrix} \mathbf{x}_1 \\ \mathbf{y}_1 \\ \mathbf{u} \end{pmatrix}, \tag{4.1}$$

where $\mathbf{x}_i$, $\mathbf{y}_i$ are the row vectors of M elements containing the (x, y) coordinates of each region i, $\mathbf{u}$ is a vector whose M elements are 1. Hence, the left side is a $2\times M$ matrix, the affine transformation is a 2×3 matrix and the last element of the right side is a $3 \times M$ matrix. We invert this problem by computing the $M \times 3$ pseudoinverse matrix associated with the matrix containing the coordinates in $\mathbf{r}_1$:

$$\begin{pmatrix} a & b & c \\ d & e & f \end{pmatrix} = \begin{pmatrix} \mathbf{x}_2 \\ \mathbf{y}_2 \end{pmatrix} \begin{pmatrix} \mathbf{x}_1 \\ \mathbf{y}_1 \\ \mathbf{u} \end{pmatrix}^{-1}. \tag{4.2}$$

The retrieval of the affine transformation takes $\sim$ 0.6 s, (when we consider only one image with $\sim$ 100 localizations) so it is possible to take calibration images each time we measure a new sample without compromising the computation speed of our measurements.

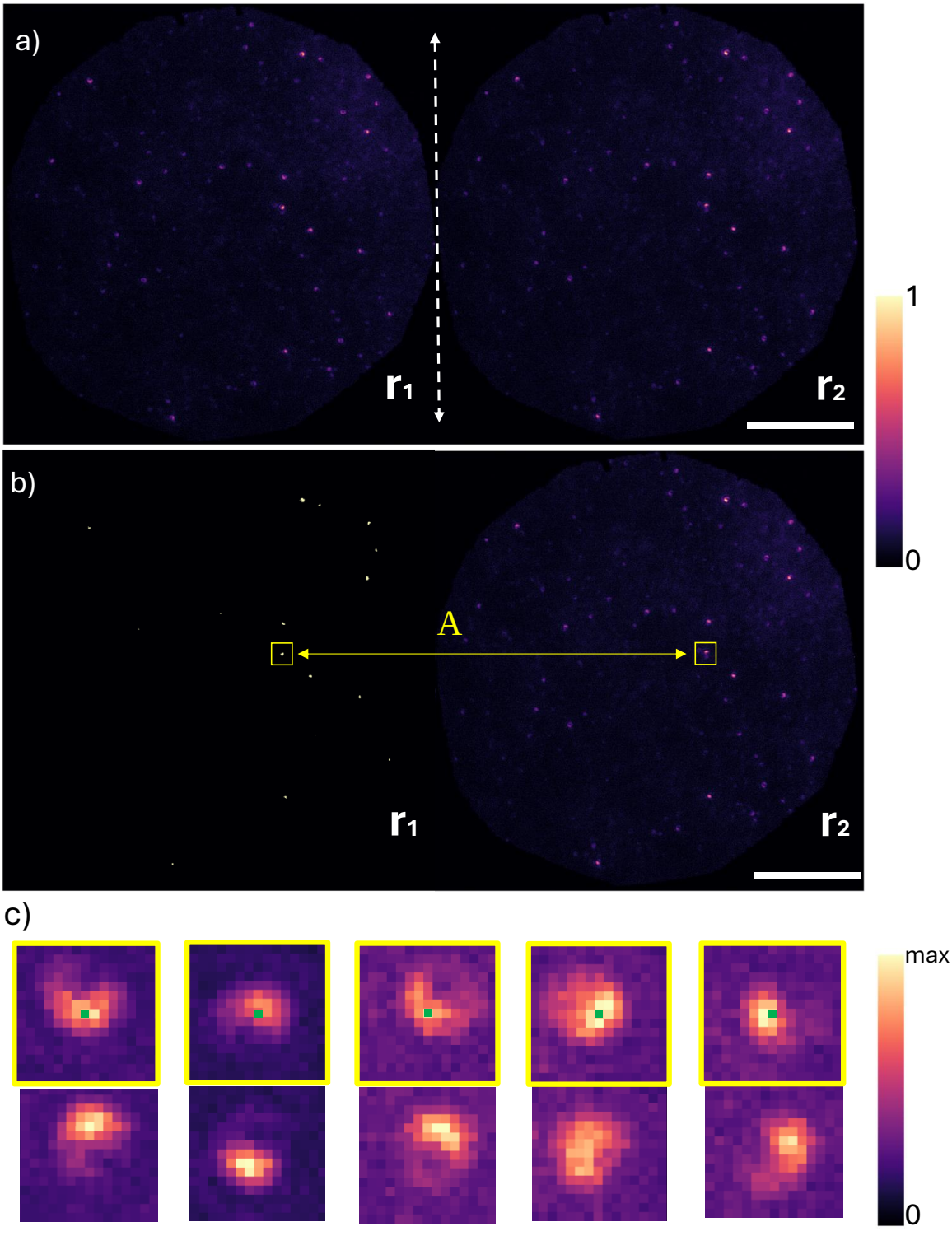

Figure 4.8.: Initial 2D localization of dipole emitters (in this case single Alexa 568 molecules deposited on a coverslip immersed in water fixed with PLL). a) Raw image of a sample of sparse 3D oriented rectilinear dipoles (scale bar 9.3 μm). b) Illustration of the PSF pairing. c) Examples of PSF pairs in an array. Note that they all present different shapes and background levels (pixel size 52.7 nm). Enclosed in yellow one the 15×15 arrays extracted from $\boldsymbol{r}_1$ and in green the geometrical centers of these arrays.

4.4.2. Initial 2D localization of dipole emitters.

A typical experimental image of a sample with sparse dipole sources is shown in 4.8a. In this section, we explain how to construct 2D arrays containing the data used to measure the Stokes-Gell-Mann parameters of the corresponding dipole. The steps to construct the arrays are:

- Binarizing the region $\mathbf{r}_1$.
- Locating the centroid (x_1, y_1) of the binarized PSFs in $\mathbf{r}_1$ (with the same algorithm used to localize the reference PSFs explained in the previous section).
- Applying the affine transformation $\mathbf{A}$ to every pair (x_1, y_1) to find the corresponding position (x_2, y_2) in the region $\mathbf{r}_2$.
- Defining a 15×15 pixel area around (x_1, y_1) and (x_2, y_2).

The previous steps are illustrated in Fig. 4.8b. With this algorithm, PSF pairs related to the same emitter can be saved. In our algorithm, we save also the coordinate of the 15×15 array's center in the region $\mathbf{r}_1$. This coordinate is measured with respect to the origin located in the upper-left corner of the complete image. Examples of common experimental PSF pairs are shown in 4.8c. Note the diversity in shapes and relative position of the PSF pairs with respect to the array's geometrical center. Note also that the intensity maximum of the PSF in $\mathbf{r}_1$ (surrounded in yellow) seems to be close to the array's geometrical center (green pixel). However, the PSF pairs seem to be decentered. This is expected because, as discussed earlier, the maximum of intensity does not correspond to the actual emitter position. These arrays of 15×30 are the starting point of the inversion problem explained in detail in the next sections. We have coded an algorithm to localize and pair PSFs. As an example of the algorithm performance, we acquired 10k frames of single fluorescent molecules data and observed a speed of 25 PSF/s or 2.5 frames/s, and a total number of detections of 103571 PSF pairs. The speed highly depends on the number of detections per frame as well as on the number of spurious detections. The lower the threshold used to binarize the region $\mathbf{r}_1$ the larger the number of spurious detections, and this threshold depends on the SNR. Fluorescence data is expected to have low SNR, hence we expect an improvement in the speed in situations of high SNR.

4.4.3. Background estimation.

In some PSFs engineering techniques, the background is included in the likelihood function as another parameter to be estimated. Here, we avoid this step by estimating it before the inversion. In Fig. 4.8a it is clear that in the complete FOV there are variations in the background. However, we observe that in the combined PSFs array (which is the data to be analysed) the background can be considered as uniform. We observe that a good estimation of the background is given by averaging the lowest values of intensity inside the $15 \times 15 \times 2$ array. We therefore subtract this value from

the raw data. It might happen that after the subtraction some pixels contain negative values, in which case we replace these negative values with zero. Figure 4.9 shows an example of the background estimation and removal procedure. The peak in the histogram is associated with the background contributions. Note that the mean intensity value in the raw data (red line) is not a good estimation of the background level as includes contributions of the brightest pixels.

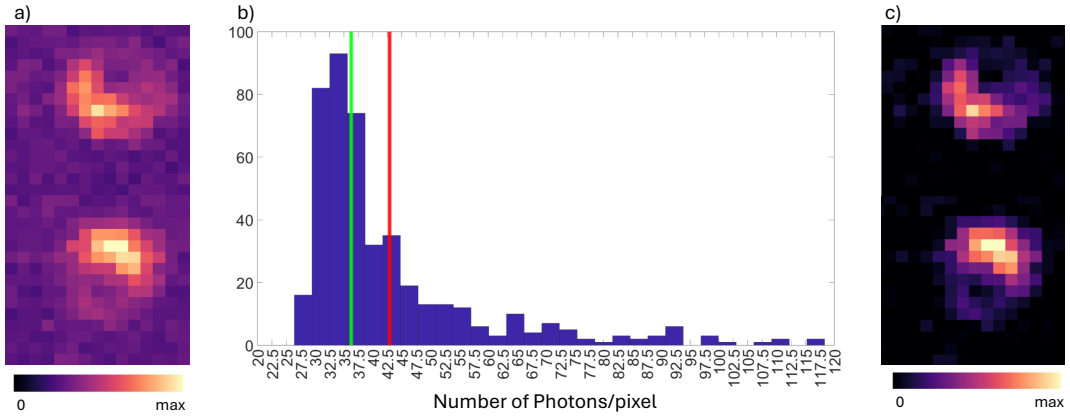

Figure 4.9.: Example of background estimation with experimental PSFs. a) Raw PSF pair. b) Intensity histogram corresponding to the array in a), the mean intensity value is in red, whereas the mean value of the lowest 360 intensity values is in green. c) PSF array with no background. Pixel size 52.7 nm.

4.4.4. Stokes-Gell-Mann parameter estimation.

The new array I with no background can be written in terms of the Stokes-Gell-Mann PSF basis:

$$I(x,y;\boldsymbol{S},x_0,y_0,z_0,d) \approx S_0 I_0 + \sum_{j=1}^{8} S_j I_j(x,y;x_0,y_0,z_0,d), \tag{4.3}$$

where (x,y) are the spatial coordinates at the array, $\boldsymbol{S}$ is the Stokes-Gell-Mann vector, (x_0,y_0,z_0) are the position coordinates of the emitter in the sample volume, and in case of having an interface, d is its distance to the focal plane. Let us focus on the estimation of $\boldsymbol{S}$, the dependence on (x_0,y_0,z_0) will be discussed below. We can concatenate the columns of the $15\times15\times2$ array I to have a vector $\boldsymbol{I}$, of dimension 450×1. The same can be done with all basis elements I_j to form a matrix $\boldsymbol{I}_S$ of dimension 450×9. Therefore, the problem is reduced to the inversion of the expression: $\boldsymbol{I}=\boldsymbol{I}_S\cdot\boldsymbol{S}$. We numerically verified that the columns of $\boldsymbol{I}_S$ are linearly independent, (qualitatively this can be seen in the basis elements in Fig. 4.5c). This property is important when inverting rectangular matrices because the corresponding *Penrose pseudoinverse* has a simple expression [76],

$$\boldsymbol{I}_S^{-1} = \left(\boldsymbol{I}_S^T\boldsymbol{I}_S\right)^{-1}\boldsymbol{I}_S^T. \tag{4.4}$$

where $\mathbf{I}_S^T$ is the 9×450 traspose matrix of $\mathbf{I}_S$, and $\left(\boldsymbol{I}_S^T \boldsymbol{I}_S\right)^{-1}$ is the 9×9 inverse matrix of $\boldsymbol{I}_S^T \boldsymbol{I}_S$. Therefore, the Stokes-Gell-Mann parameters can be written in terms of the matrix product between the pseudoinverse and the data $\boldsymbol{I}$:

$$\boldsymbol{S} = \left(\boldsymbol{I}_S^T \boldsymbol{I}_S\right)^{-1} \boldsymbol{I}_S^T \cdot \boldsymbol{I}. \tag{4.5}$$

The estimation of the Stokes-Gell-Mann parameters seems to be now reduced to the problem of pre-calculating the basis $\boldsymbol{I}_S$ that best describes the system and multiplying the vectorized data $\boldsymbol{I}$ by the correct pseudoinverse.

It is well-known that the estimation of $\boldsymbol{S}$ by using the pseudo-inverse estimator $\boldsymbol{I}_S^{-1}$ reaches the Cramer-Rao lower bounds and it is an unbiased estimation in the presence of *Gaussian* noise. However, we are in the presence of *Poissonian* noise. Previous work in paraxial polarimetry [77] and astronomy [78] has discussed the practical convenience of using Eq. (4.5) (which is a matrix multiplication) compared to implementing maximum likelihood estimation, that can be computationally expensive and offer similar results. In this work we aim to handle a large amount of data (from thousands to hundreds-of-thousands of localizations), so we employ Eq. (4.5) to estimate $\boldsymbol{S}$ at the cost of introducing bias in our measurements. We discuss this bias in the next sections.

4.4.5. Accurate Stokes-Gell-Mann parameter estimation and correction to the initial 2D location.

Equation (4.5) is only valid when the basis $\boldsymbol{I}_S$ is computed taking into account the correct spatial coordinates (x_0, y_0, z_0, d) associated with the dipole emitter generating the PSF pair in $\boldsymbol{I}$. Let us assume that the dipole is in focus and that there is no interface, so that $z_0 = d = 0$. Let us also assume that the PSFs are perfectly matched through the affine transformation. We observe in Fig. 4.8 that the PSF pairs seem to be equally decentered with respect to the green pixel that labels the geometrical center of the array corresponding to $\mathbf{r}_1$. We can then compute different bases $\boldsymbol{I}_S^k$ that account for the apparent displacement in x and y. We then multiply the vector data $\boldsymbol{I}$ by all the pseudoinverse matrices $\left[\left(\boldsymbol{I}_S^T \boldsymbol{I}_S\right)^{-1} \boldsymbol{I}_S^T\right]^k$ and obtain a set of estimated Stokes-Gell-Mann parameters $\boldsymbol{S}^k$. This process is illustrated in Fig. 4.10. With the estimated $\boldsymbol{S}^k$ a set of PSFs is computed as $\boldsymbol{PSF}^k = \boldsymbol{I}_S^k \cdot \boldsymbol{S}^k$. Then we quantify the similarity of these PSFs and the data with the normalized cross-correlation function:

$$Q = \frac{\boldsymbol{I} \cdot \boldsymbol{PSF}^k}{\sqrt{|\boldsymbol{I}||\boldsymbol{PSF}^k|}}. \tag{4.6}$$

If $\boldsymbol{I} = \boldsymbol{PSF}^k$, then $Q = 1$, hence we identify the $\boldsymbol{PSF}^k$ that maximizes Q and associate the corresponding $\boldsymbol{S}^k$ (and the corresponding displacement from the geometrical center) as the set of parameters that better describe our measurements $\boldsymbol{I}$.

One of the advantages of using the Stokes-Gell-Mann parameters is that we can

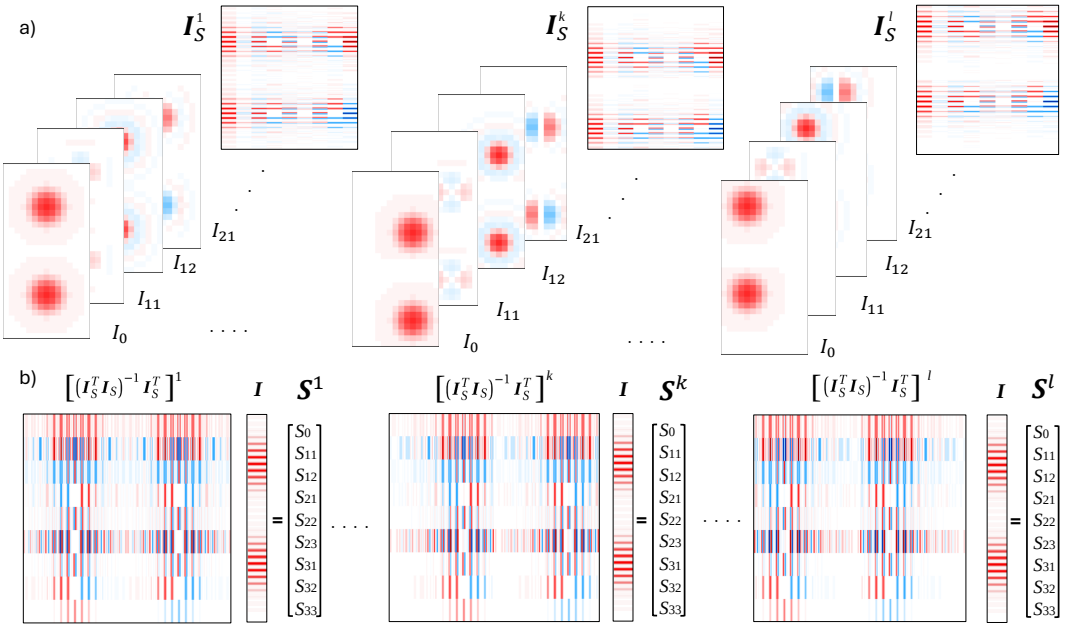

Figure 4.10.: Stokes-Gell-Mann parameter estimation. a) Illustration of the construction of the set of matrices $\boldsymbol{I}_S^k$ from the columns of the basis elements. b) Illustration of the Stokes-Gell-Mann parameters estimation by multiplying the vectorized data $\boldsymbol{I}$ by the corresponding pesudoinverse $\left[\left(\boldsymbol{I}_S^T \boldsymbol{I}_S\right)^{-1} \boldsymbol{I}_S^T\right]^k$.

directly construct the matrix Γ_{3D} with Eq. (1.13), or equivalently $\mathbb{m}$, and verify if the estimated parameters correspond to a *physical* polarization matrix. By definition Γ_{3D} is Hermitian, hence the set of eigenvalues are real. We can always decompose Γ_{3D} in terms of the correlation matrices $\boldsymbol{e}_j \boldsymbol{e}_j^\dagger$ associated with its eigenvectors $\boldsymbol{e}_j$, with the eigenvalues Λ_j as coefficients of this expansion:

$$\Gamma_{3D} = \sum \Lambda_j \boldsymbol{e}_j \boldsymbol{e}_j^\dagger. \tag{4.7}$$

We can interpret this expression as a decomposition into different polarization matrices, and each Λ_j as the corresponding energy contained in those contributions, hence $\Lambda_j \geq 0$. Note that the trace of Γ_{3D} is given by $\mathrm{Tr}(\Gamma_{3D}) = \Lambda_1 + \Lambda_2 + \Lambda_3$. When we use the normalized Stokes-Gell-Mann parameters, $\mathrm{Tr}(\Gamma_{3D}) = 1$.

These conditions are useful when one or two eigenvalues resulting from the measured data are negative. In those cases, we estimate the *closest physical state* to the measurements. We numerically compute the eigenvalues and eigenvectors of the measured Γ_{3D} and replace with zero the negative Λ_j in Eq. (4.7). We then re normalize the calculated Γ_{3D} such that $\mathrm{Tr}(\Gamma'_{3D}) = 1$. Finally, from the physical Γ_{3D} we compute the physical Stokes-Gell-Mann parameters with Eq. (1.14). From now on, we assume that every time we estimate the Stokes-Gell-Mann parameters we always verify if they correspond to physical states, and otherwise we compute the closest physical parameters. The main origin of the non-physical parameters is associated with noise

in the signal. This algorithm is illustrated in the workflow in Fig. 4.13 at the end of this section.

4.4.6. 3D localization of dipole emitters.

Let us now assume that $z_0 \neq 0$, $d = 0$ and the set of parameters $\boldsymbol{S}^k$ and the corresponding basis $\boldsymbol{I}^k$ correspond to the best fit (calculated as in the previous section). We can assume an error on the emitter coordinates and interface position of $\boldsymbol{\delta r_0} = (\Delta x_0, \Delta y_0, \Delta z_0)$. We write the Taylor expansion of the measured intensity distribution I:

$$I(x,y;\boldsymbol{S}^k,\boldsymbol{\delta r_0}) \approx \sum_{j=1}^{9} S_j^k I_j^k(x,y;\boldsymbol{r}_0) + \nabla_0 \left[\sum_{j=1}^{9} S_j^k I_j^k(x,y;\boldsymbol{r}_0)\} \right] \cdot \boldsymbol{\delta r_0}, \tag{4.8}$$

where ∇_0 is the gradient on the spatial coordinates of the dipole. We can then rewrite the previous expression as

$$I(x,y;\boldsymbol{S}^k,\boldsymbol{\delta r_0}) - \sum_{j=1}^{9} S_j^k I_j^k(x,y;\boldsymbol{r}_0) \approx \left[\sum_{j=1}^{9} S_j^k \nabla_0 I_j^k(x,y;\boldsymbol{r}_0)\} \right] \cdot \boldsymbol{\delta r_0}. \tag{4.9}$$

Similarly, as in the previous section, we can form vectors with the arrays and define as $\boldsymbol{\Delta I}^k$ the left hand side of the previous equation, which is the difference between the vector data and the best fit obtained as in the previous section. We can bring the gradient inside the sum and the terms $\nabla_0 I_i^k$ are computed numerically (as explained in the Appendix A2.), and we can write:

$$\boldsymbol{\Delta I}^k \approx \nabla_{\boldsymbol{0}} \boldsymbol{I}^k \cdot \boldsymbol{\delta r_0} \tag{4.10}$$

where $\nabla_{\boldsymbol{0}} \boldsymbol{I}^k$ is the matrix of dimensions 450×3 that has as columns the vectorized form of $\sum_{j=1}^{9} S_j \partial_{r0_i} I_j^k(x,y;\boldsymbol{r}_0)$. If the columns of $\nabla_{\boldsymbol{0}} \boldsymbol{I}^k$ are linearly independent, we can write a simple expression for $\boldsymbol{\delta r}_0$:

$$\boldsymbol{\delta r_0} \approx \left((\nabla_{\boldsymbol{0}} \boldsymbol{I}^k)^T \nabla_{\boldsymbol{0}} \boldsymbol{I}^k \right)^{-1} (\nabla_{\boldsymbol{0}} \boldsymbol{I}^k)^T \boldsymbol{\Delta I}^k, \tag{4.11}$$

where the term $((\nabla_{\boldsymbol{0}} \boldsymbol{I}^k)^T \nabla_{\boldsymbol{0}} \boldsymbol{I}^k)^{-1} (\nabla_{\boldsymbol{0}} \boldsymbol{I}^k)^T$ is the pseudo inverse of $\nabla_{\boldsymbol{0}} \boldsymbol{I}^k$. Therefore, we have reduced both the estimation of the Stokes-Gell-Mann parameters and the spatial coordinates (at least for small displacements from the basis position and from $z_0 = 0$) of the emitter to a sequence of multiplications of the data vectors by precomputed arrays. We can insert the term $(\boldsymbol{\delta r_0})^T$ estimated from Eq. (4.11) in Eq. (4.8) and rewrite it as

$$\boldsymbol{I}(x,y;\boldsymbol{S},\boldsymbol{\delta r_0}) = \left[\boldsymbol{I}^k + \partial_{x0} \boldsymbol{I}^k \Delta x0 + \partial_{y0} \boldsymbol{I}^k \Delta y0 + \partial_{z0} \boldsymbol{I}^k \Delta z0 \right] \cdot \boldsymbol{S}, \tag{4.12}$$

where the term inside the square brackets is a 450×9 matrix containing the *partial derivatives Stokes-Gell-Mann PSF basis* multiplied by the corresponding spatial coor-

dinate displacement. We calculate the pseudoinverse matrix of this term and obtain a new estimation for the Stokes-Gell-Mann parameters as

$$\boldsymbol{S} \approx \left[\boldsymbol{I}^k + \partial_{x0}\boldsymbol{I}^k \Delta x0 + \partial_{y0}\boldsymbol{I}^k \Delta y0 + \partial_{z0}\boldsymbol{I}^k \Delta z0\right]^{-1} \cdot \boldsymbol{I}, \tag{4.13}$$

Although simple, we need to take special care when applying the Taylor expansion. In Eq. (4.8) the data $\boldsymbol{I}$ is expressed as a linear superposition of the basis elements I^k and its spatial derivatives $\partial_{x0} I^k$. Hence, all these elements should be linearly independent to avoid coupling between the spatial and the Stokes parameters. Let us assume that we can neglect the corrections Δx_0 and Δy_0 and that the only important contribution comes from Δz_0. This assumption is valid once we find the best fit $\boldsymbol{S}^k$ and $\boldsymbol{I}^k$. In Fig. 4.11 we show the basis I^k and the $\partial_{z0_j} I^k$. Note that if we only restrict ourselves to the elements associated with rectilinear dipoles (enclosed in green), all the elements are different and orthogonal. However, when we consider the complete basis for elliptical dipoles, we observe that some terms are approximately proportional: $I_{21} \sim -\partial_{z0} I^k_{31}$, $I_{22} \sim \partial_{z0} I^k_{32}$, $I_{31} \sim \partial_{z0} I^k_{21}$ and $I_{32} \sim -\partial_{z0} I^k_{22}$.

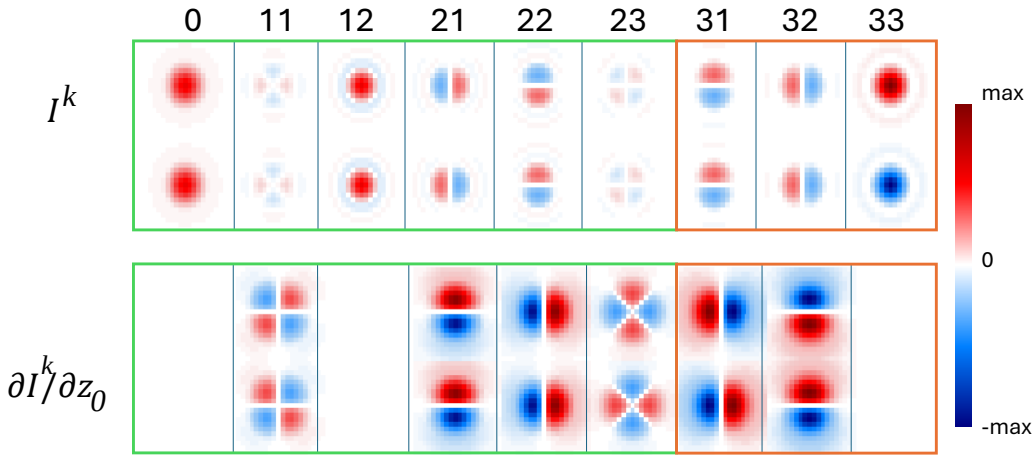

Figure 4.11.: Axial localization and ellipticity coupling. Note that $I_{21} \sim -\partial_{z0} I^k_{31}$, $I_{22} \sim \partial_{z0} I^k_{32}$, $I_{31} \sim \partial_{z0} I^k_{21}$ and $I_{32} \sim -\partial_{z0} I^k_{22}$.

This means that if we analyze data of rectilinear dipoles (for instance fluorescent molecules) using the complete Stokes-Gell-Mann PSF basis we could measure false ellipticity due to axial variations of the emitter. Similarly, when measuring elliptical dipoles, it is possible to measure a false defocus due to the presence of transverse ellipticity. A solution to avoid inaccuracies induced by such property is to introduce a pre-knowledge on either the absence of ellipticity (for instance when measuring fluorescent rectilinear dipoles) or on the defocus (for instance when measuring elliptic dipoles at known axial positions). This aspect is discussed in the experimental Chapters 5 and 6.

Let us now discuss the possible corrections to the 2D localization achieved by associating the position of the best fit $\boldsymbol{I}^k$ to the measured emitters. Similarly to the

previous discussion on axial localization, we can see in the basis element shown in Fig 4.12 that only those elements associated with rectilinear dipoles are uncorrelated. These observations suggest that we must remove the last three terms from the basis when measuring rectilinear dipoles. In the case of elliptical dipoles, we must avoid correcting the spatial coordinates with the Taylor expansion and rely on the best fit.

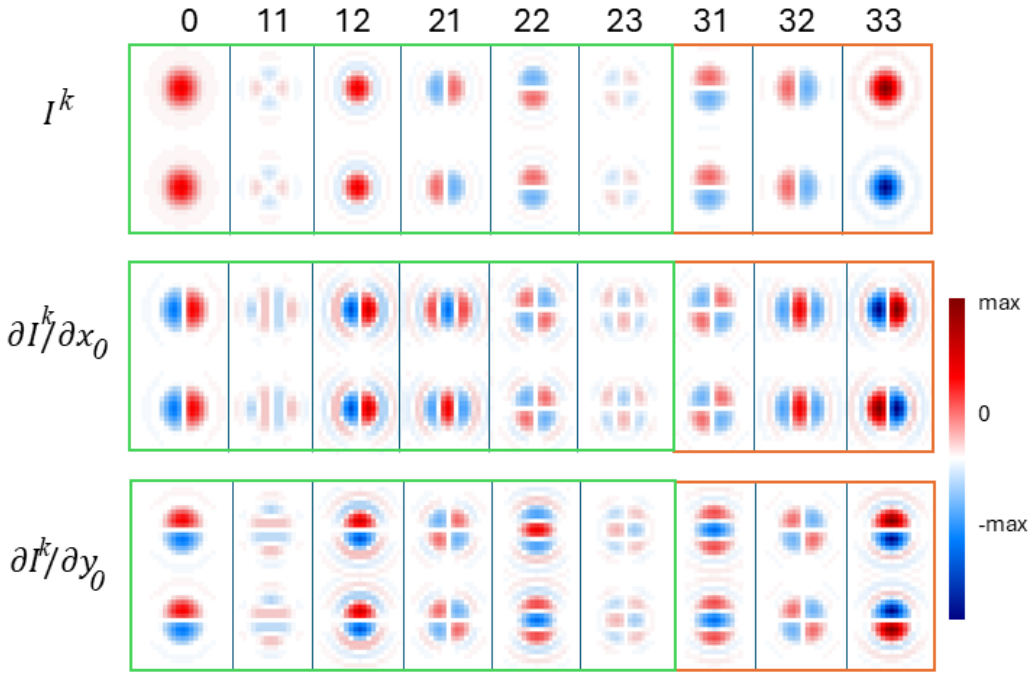

Figure 4.12.: 2D localization and ellipticity coupling. Note that $I_{21} \sim \partial_{x0} I^k_{33}$, $I_{22} \sim -\partial_{y0} I^k_{33}$, $I_{23} \sim \partial_{x0} I^k_{31}$, $I_{23} \sim -\partial_{y0} I^k_{32}$, $I_{31} \sim \partial_{y0} I^k_0$ and $I_{32} \sim -\partial_{x0} I^k_0$.

We speculate that C-3POL is the simplest experimental configuration to decouple the Stokes parameters of rectilinear dipoles and their spatial information. As shown in Ref. [18], the corresponding Stokes-Gell-Mann PSF basis and the partial axial derivatives basis for CHIDO present similar correlations between the elliptical basis elements and the spatial derivatives elements. It could be interesting to answer the question of whether there is a simple experimental configuration (where the signal is only separated into a maximum of two polarization channels) that effectively decouples the polarization parameters of elliptical dipoles and the localization information.

In practice, we typically compute 289 bases accounting for displacements in (x, y) in the central area of 9×9 pixels. They are separated by half a pixel size i.e. 26.35 nm. As the computational time increases with the number of bases, in cases where the number of measurements is $\sim 10^4$ PSFs we can afford computing bases separated by a distance of a quarter-of-pixel size.

As part of this thesis project, we coded a routine in Matlab to analyze the data based on the previous discussions. We present a workflow of the complete algorithm in Fig. 4.13.

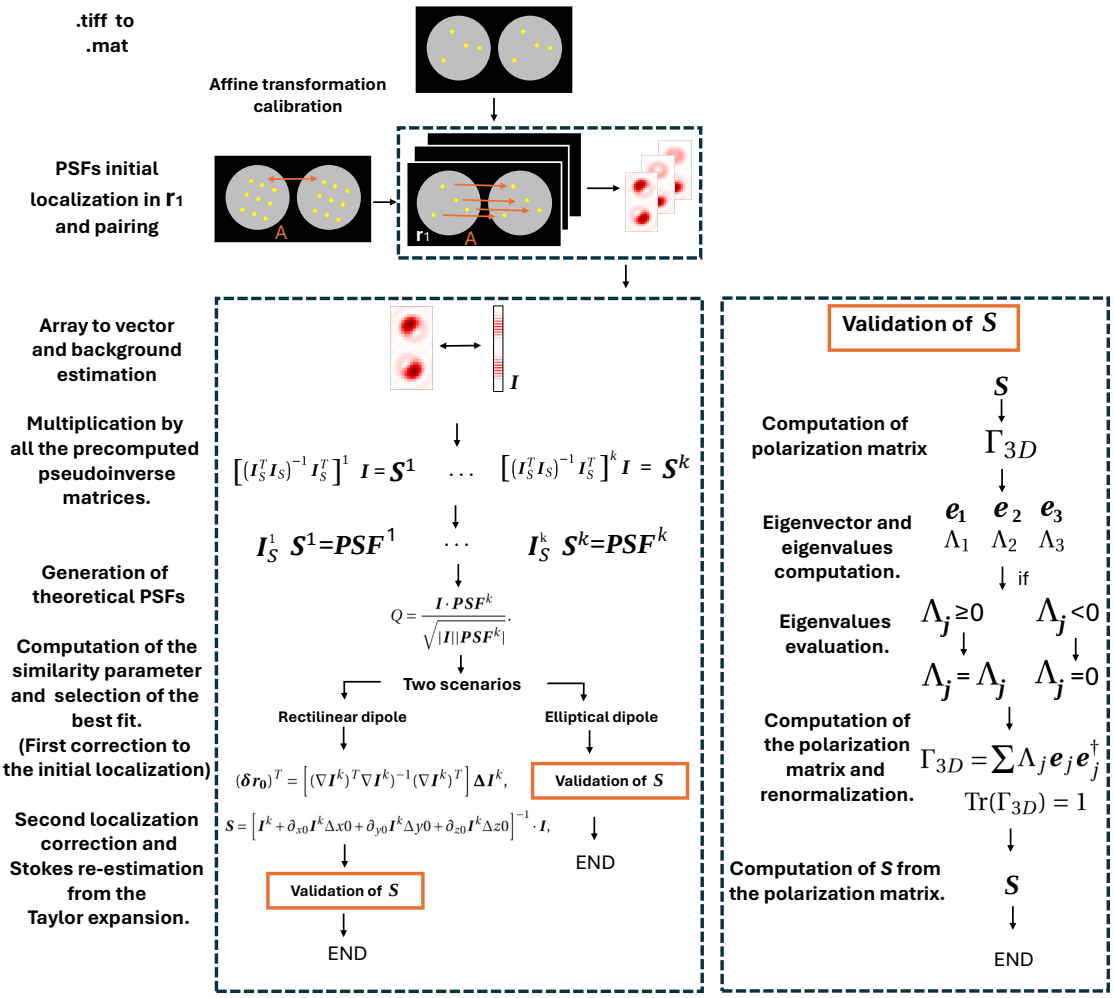

Figure 4.13.: Data analysis workflow. The sections enclosed in different boxes can be executed independently. Each time we estimate the Stokes-Gell-Mann parameters we corroborate that they correspond to a physical dipole, otherwise; we compute the closest physical set of parameters. We also test if $\delta\mathbf{r_0}$ is consistent with the expected corrections. We discard the correction if $|\Delta x0_j| \geq 300$ nm for at least one j.

The computational speed of the complete data analysis depends on several factors such as the number of frames, number of emitters per frame, and SNR. As illustrated in the workflow, the analysis of all the PSF pairs can be done independently, when analyzing a large amount of data (~ 900k pairs) we observe a computational speed of ~ 200 PSF pairs/s. Note that this speed is approximately constant as the parameter retrieval is based on deterministic operations. Note also that during the previous discussion, we only referred to the nature of the detection configuration when we discussed the limitations in the Taylor expansion. Hence, we expect that the same algorithm can be applied to other PSF-based techniques where the complete basis elements are linearly independent (or a subset of them), e.g. CHIDO, defocused PSF, scalar vortex, or other techniques with a maximum of two polarized channels.

4.5. Numerical studies.

We performed Monte Carlo simulations to quantify the precision of our method. We start by generating pairs of PSFs corresponding to rectilinear dipoles that are perfectly matched but displaced from the array's geometrical center. We also introduce a small amount of defocus. In practice, fluorescent data offer the lowest SNR, and hence the lowest precision. We simulate PSFs considering Poissonian noise and photon numbers similar to situations in fluorescence data, as well as PSFs with higher SNR similar to data from scattering particles. We generate the data with Eq. (3.12) to have control of the 3D position and orientation parameters. We analyze the simulated data using the algorithm described in the previous section.

4.5.1. Continuous medium and fully polarized rectilinear dipoles.

We study numerically the situation where monochromatic dipole emitters of $\lambda = 532$ nm are immersed in a medium of index $n = 1.518$, placed close to the focal plane of an oil immersion objective with effective collection aperture of NA= 1.49.

We perform 100 realizations of the same dipole $\hat{\boldsymbol{\mu}} = (\cos\xi\sin\eta, \sin\eta\sin\xi, \cos\eta)$. In each realization the dipole is located at a random 3D position inside a volume of $260 \times 260 \times 125$ nm^3 around the focus. We sample the hemisphere of 3D directions, illustrated in Fig. 4.14, considering $\eta \in [0, 90]$ in steps of 6°, $\xi \in [0, 345]$ in steps of 15° and $P = 1$. For each dipole configuration, we compute the expected

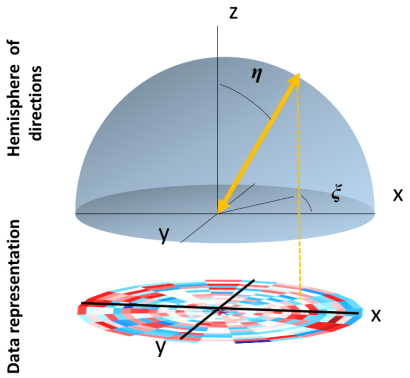

Figure 4.14.: Hemisphere of directions and data representation.

accuracy of the variables (η, ξ, P, x_0, y_0, and z_0) as the mean value of the difference between the ground truth θ and the estimated parameter $\langle\Delta\theta\rangle = \langle\theta - \hat{\theta}\rangle$ and the precision as the standard deviation denoted by σ_θ. We show the accuracy and the precision in polar graphs representing the projection of the orientations hemisphere to a plane. The radial position of each data point is proportional to η and the azimuthal angle of each data point is ξ, as shown in Fig. 4.14.

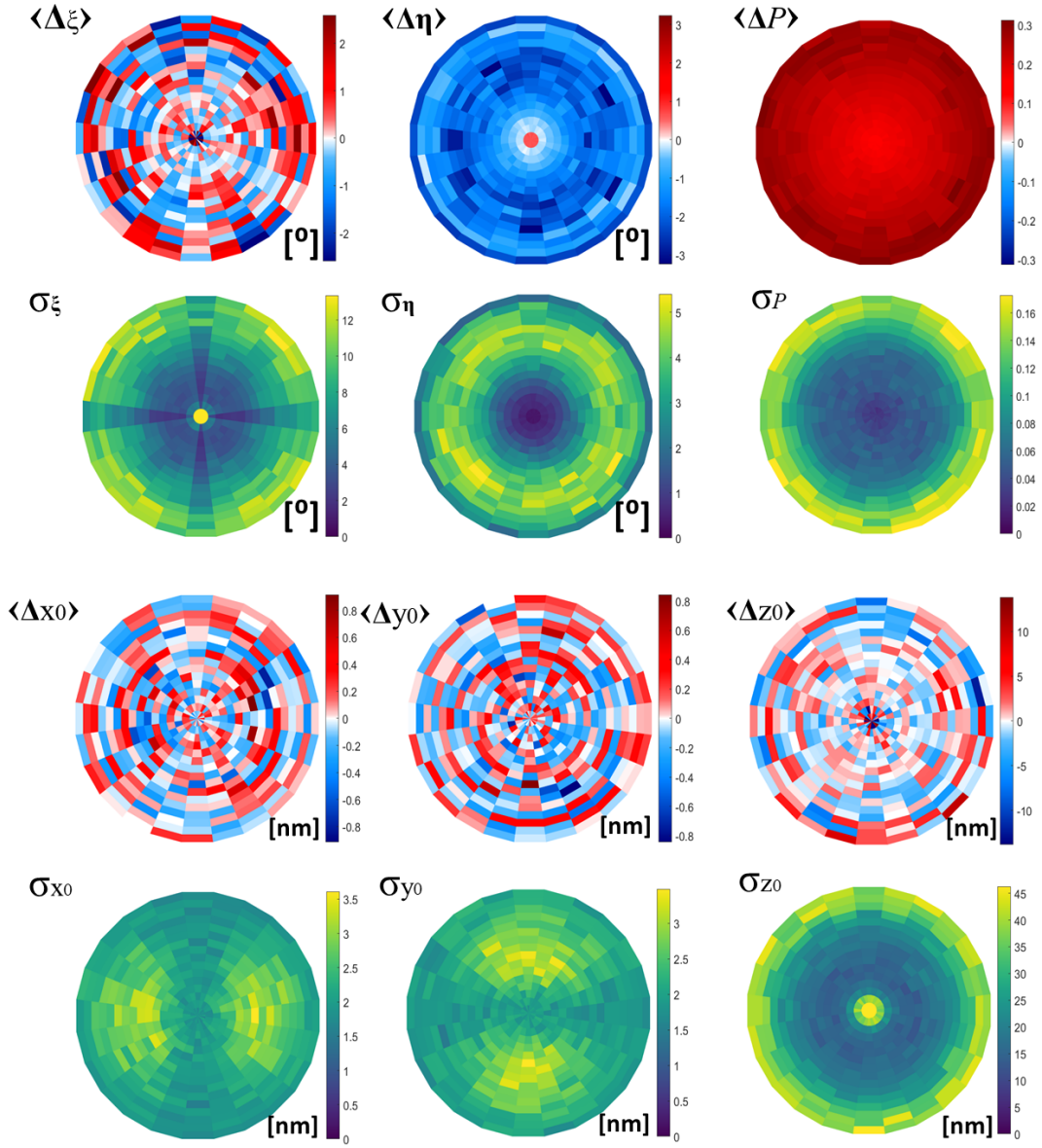

Figure 4.15.: Accuracy and precision for the in-plane ξ and off-plane η angles, the degree of polarization P and the spatial coordinates x_0, y_0, z_0. We consider 3500 signal photons with no background.

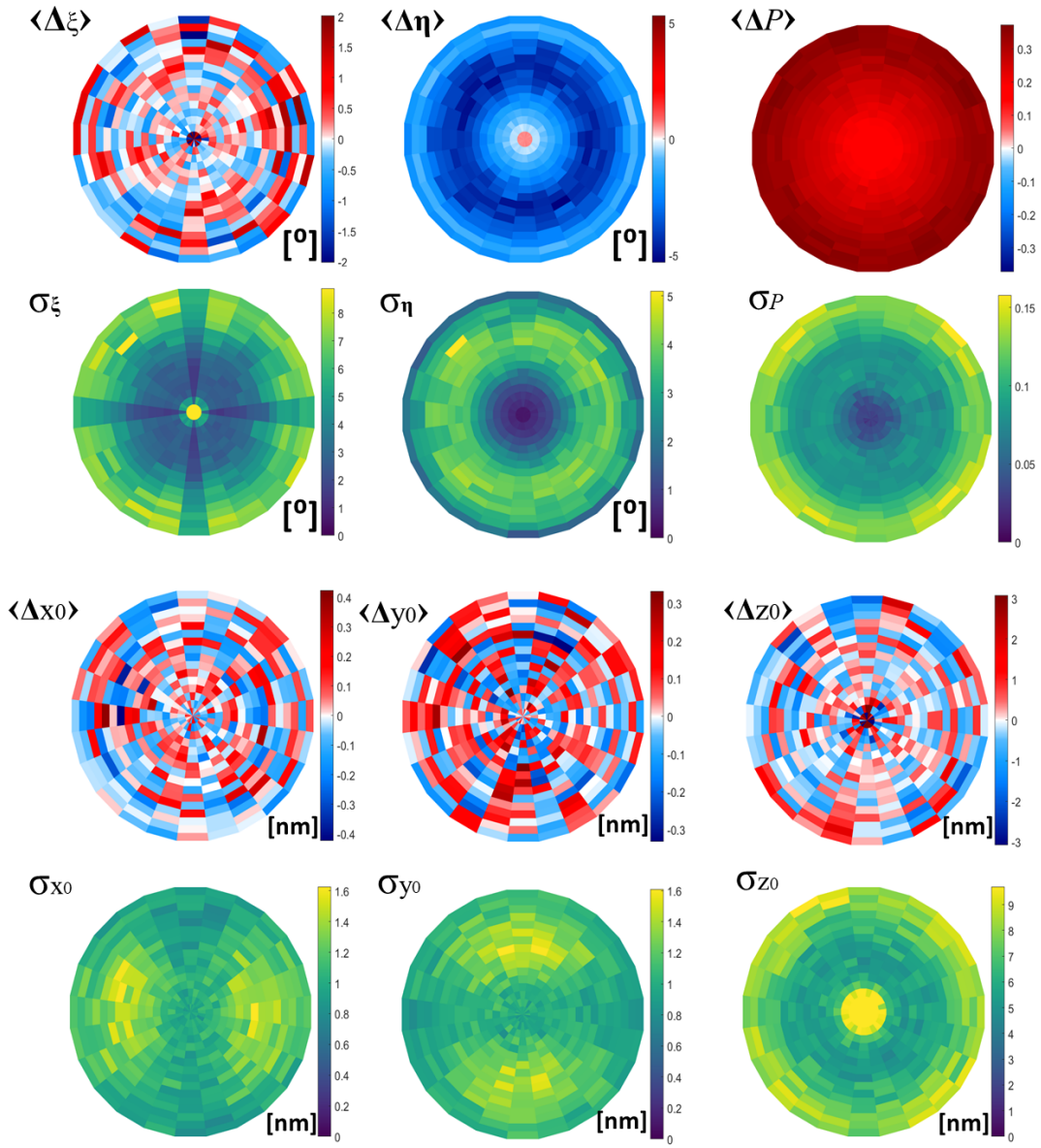

Figure 4.16.: Accuracy and precision for the in-plane ξ and off-plane η angles, the degree of polarization P and the spatial coordinates x_0, y_0, z_0. We consider 10000 signal photons with no background.

We explore the situations of 3500 and 10000 signal photons with no background (i.e. total intensity of the emitter summed over both LHC and RHC channels). In both cases, we notice that the accuracy for all the variables appears to be independent of ξ. This independence is expected since the shape of the PSF does not depend on ξ. We observe a bias of $\sim 30\%$ for the degree of polarization, which can be explained by the similarity between the basis elements I_0 and I_{21}. We also observe a bias in η of $\sim 5°$. These values are very close to accuracy performances obtained in other PSF engineering methods [13, 18, 33]. The precision depends mostly on η, except for σ_ξ, σ_{x0}, σ_{y0} where there are subtle asymmetries along the horizontal and vertical axes, these features perhaps being related to the pixel-based detection. Based on the low photon regime, we expect a precision of about $\sigma_\xi \approx 12°$ and $\sigma_\eta \approx 5°$. The precision on η is very close to performances obtained with other PSF engineering methods [13, 18, 33]. In the spatial parameters, we observe a precision for the 2D localization of $\leq 3.5nm$ (in the low photon number regime), a standard theoretical value in SMLM and SMOLM techniques [6, 13, 18]. As expected, the axial coordinate z_0 estimation is less precise and there is a clear incapability of measuring longitudinal dipoles, notice that the graph for σ_{z0} diverges at the center. This is explained by the fact that the PSF of those dipoles has a perfect doughnut-like shape and hence it is not possible to distinguish the axial position by the counter-rotation effect.

From the data used for the Monte Carlo simulations, we extract some fabricated PSFs and present comparisons of the corresponding fit in Fig. 4.18. Note that we can resolve a variety of shapes and 2D positions in the regime of large and low photon numbers.

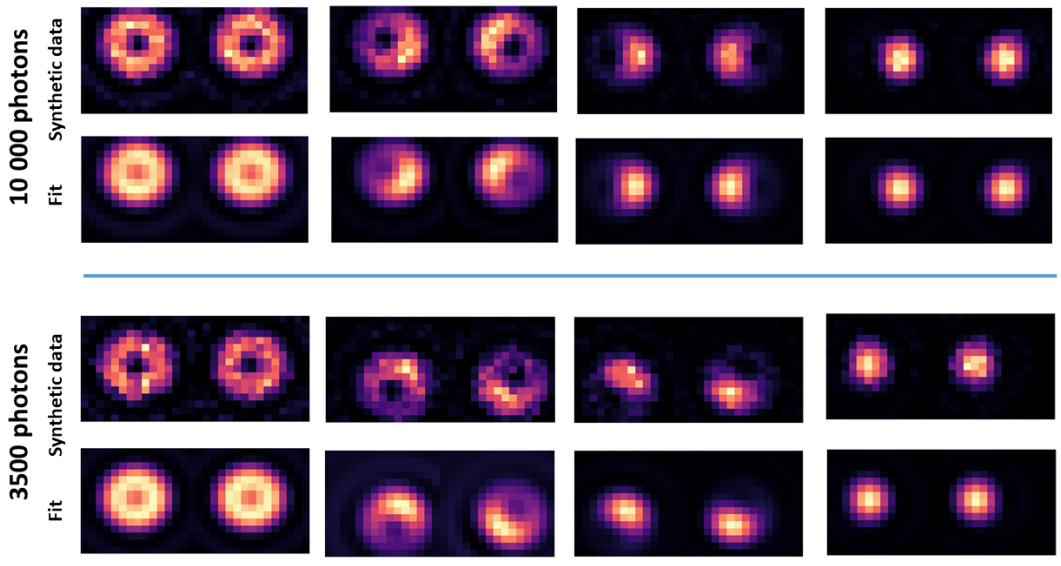

Figure 4.17.: Comparison between synthetic data and the best fit for the case of 3500 and 10000 photons. Note that we can account for displacements from the array geometrical center.

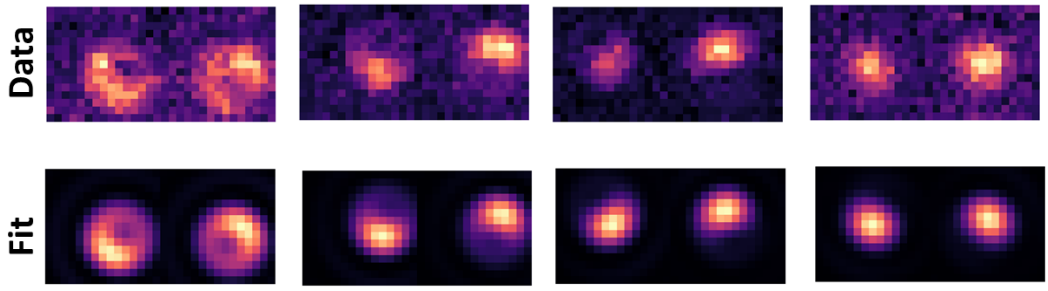

Figure 4.18.: Comparison between experimental data and the best fit for the PSFs of single fluorescent molecules. Note in the second set of PSFs that the algorithm can fit PSFs that are not fully contained in the array.

As a last example, we show a comparison between experimental PSFs and the best fit. Those PSFs correspond to fluorescent molecules. Despite the presence of background noise it is possible to fit PSFs that are qualitatively similar to the measurements and positioned at similar locations of the array. In the next chapter, we discus the experimental configuration associated with those PSFs.

4.5.2. Continuous medium and fully polarized elliptical dipoles.

We present accuracy and precision graphs for elliptical dipoles located in the focal plane of a high NA objective. The dipoles are randomly positioned in 2D. We show the results of fully polarized elliptical dipoles with opposite spin vectors oriented in 3D as illustrated in Fig. 4.19. The spin vector is contained in the $y-z$ plane and the ellipse orientation is defined by the angle η_a between the major axis and the z axis.

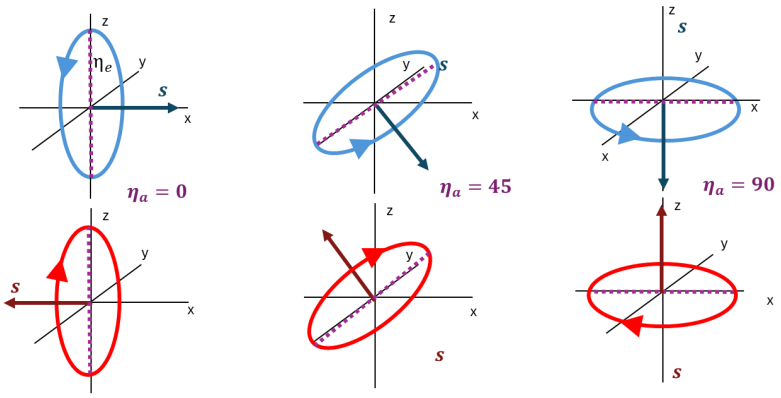

Figure 4.19.: Illustration of elliptical 3D oriented dipoles with opposite handedness. The ellipse major axis (dotted line) has different angles η_a with respect to the z axis. The spin vector is contained in the $y-z$ plane.

We generate 3D elliptical dipoles by using the expression $\hat{\boldsymbol{\mu}} = \mathbf{a} \pm i\mathbf{b}$, where $\mathbf{a}$ and $\mathbf{b}$

are the major and minor axes. The sign determines the handedness of the ellipse. We compute different ellipses characterized by the ratio between the minor b and major a axis lengths $r_{ba} = b/a$. We show accuracy and precision graphs for r_{ba} as a function of r_{ba} and the angle η_a. Since $\mathbf{b}$ is, by construction, orthogonal to $\mathbf{a}$ we only quantify the similarity between the recovered major axis $\mathbf{a}_e$ and the ground truth $\mathbf{a}_{0e}$. We show the accuracy and precision of the angle $\theta_a = \text{acos}(\mathbf{a}_e \cdot \mathbf{a}_{0e})$ between those two vectors.

We also quantify the similarity between the recovered normalized spin vector $\mathbf{s}_e$ and the ground truth spin vector $\mathbf{s}_{0e}$ by showing the accuracy and precision of the angle $\theta_s = \text{acos}(\mathbf{s}_e \cdot \mathbf{s}_{0e})$ between them. The vector $\mathbf{s}_e$ contains the recovered normalized Stokes-Gell-Mann parameters $\mathbf{s}_e = (s_{13}, s_{23}, s_{33})$.

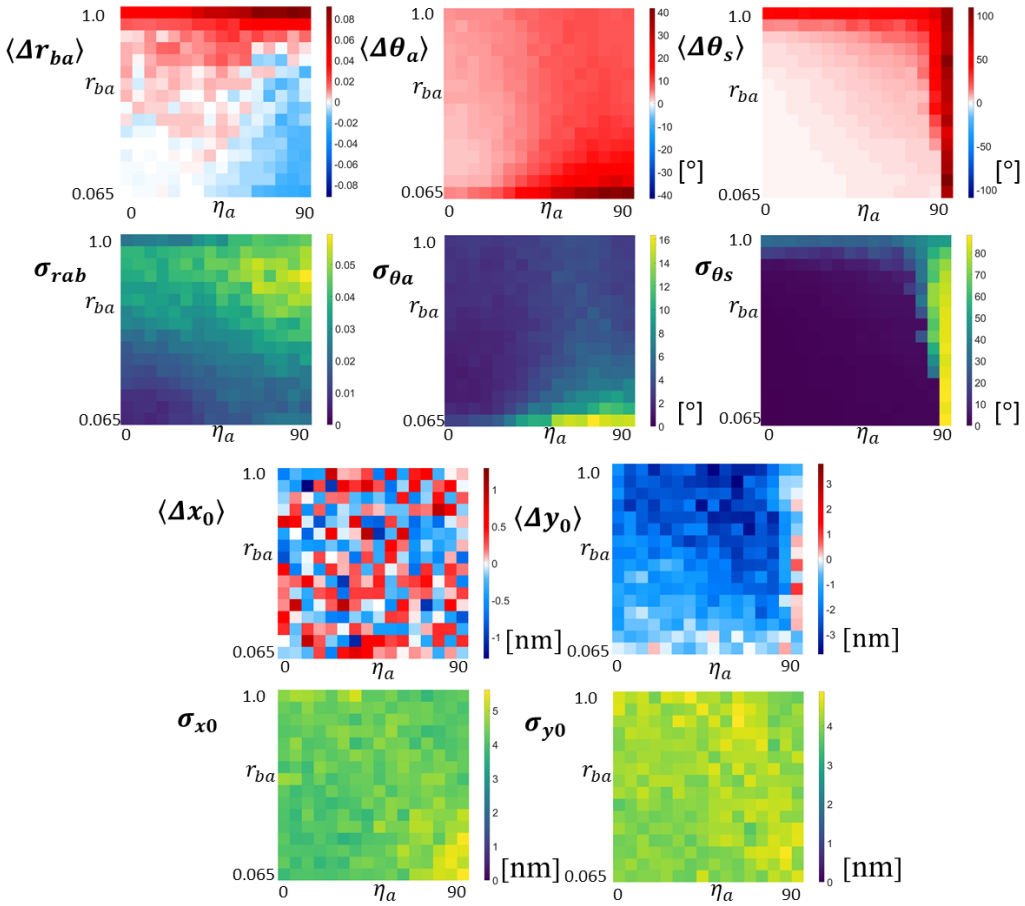

Figure 4.20.: Accuracy and precision for elliptical dipoles as functions of r_{ba} and η_a. We consider the situation of 10000 signal photons with no background.

We explore the situation of high photon number by considering 10,000 photons and elliptical dipoles, $\lambda = 532$nm, with $r_{ba} \in [0.0625, 1]$ in steps of 0.0625. The extreme value $r_{ba} = 1$ corresponds to circular dipoles and $r_{ba} = 0.0625$ corresponds to a narrow ellipse. We explore angles $\eta_e \in [0°, 90°]$ in steps of 6°. We perform 100 realizations of each dipole defined by (r_{ba}, η_e). The dipoles are located at the focal plane of an objective with NA=1.49 in random (x_0, y_0) positions inside an area of 500×500 nm^2.

We generate a set of PSF bases for emitters at the focal plane spatially separated by 1/4 of pixel size, equivalent to 13.17 nm. We do not use the Taylor expansion to improve the 3D localization.

In both cases presented in Fig. 4.20 and 4.21, we observe significant bias for r_{ba}, θ_a and θ_s at the limit cases of circular and linear dipole. For η_s, we also observe bias in the high η_a limit. However, even in the high bias regime $\langle \Delta\theta_s \rangle \leq 180$ which implies that is possible to measure the main direction of spin related to the dipoles. If we restrict ourselves to the regions of low bias, the precision graphs for the major axis and spin orientation show precisions of the order of $\sim 10°$.

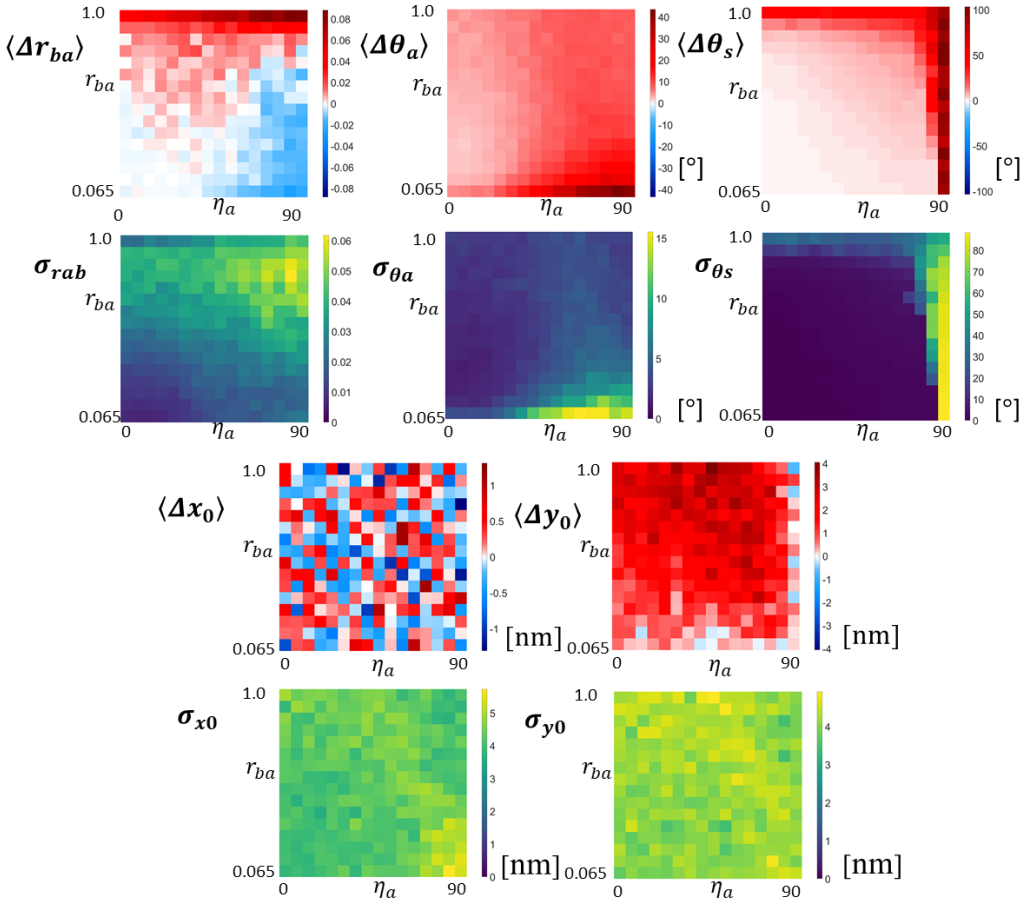

Figure 4.21.: Accuracy and precision for elliptical dipoles as functions of r_{ba} and η_a. We consider 10000 signal photons with no background. Same conditions as in Fig. 4.20 considering the opposite spin.

In the graphs for spatial variable accuracy, we observe different behavior in those for x_0 and y_0, whereas x_0 seems to be unbiased, y_0 presents a constant bias ~ 4 nm, except for the limit cases of linear dipole and $\eta_a = 90$. This is consistent with the discussion about the correlation between the Stokes-Gell-Mann parameters associated with the spin and the spatial coordinates. The ground truth spin vector is given by $\mathbf{s} = \pm(-\cos\eta, 0, \sin\eta)$. The only value that can be correlated with a spatial coordinate is

s_{31}. In Fig. 4.12 we observe similarity in the basis elements $I_{31} \sim \partial_{y0} I_0^k$ and $I_{31} \sim \partial_{y0} I_{12}^k$, which is consistent with the observed bias in y_0. Note that signs of this bias change according to the spin handedness. The precision graphs for variables σ_{x0} and σ_{y0} have values of ≤5 nm which are consistent with values found for rectilinear dipoles.

4.6. Final remarks

In this Chapter we introduced C-3POL, a simple configuration to measure 3D-oriented rectilinear and elliptical dipoles in a single shot. We discuss its capabilities for measuring the complete set of 9 generalized Stokes-Gell-Mann parameters. By computing the Fisher information matrix of the system we show that only two sets of variables are correlated, contrary to other simple systems (discussed in the previous chapter) where more variables can be correlated. We commented on the presence of optical vortices in the right and left polarization components of dipole radiation and how this feature can be associated with experimental systems that are capable of measuring 3D oriented dipoles, in particular CHIDO, phase vortex modulation and C-3 POL. These configurations present symmetries on the phase or polarization modulation that preserve the natural features of dipole radiation.

We introduced a methodology based on the linearity of the PSF shape to the Stokes-Gell-Mann basis to analyse the data. We decouple the problem of measuring the nine Stokes-Gell-Mann parameters and the 3D position of the emitters by creating a set of precomputed bases that account for the 2D localization and selecting the one associated with the best fit. We estimate the axial coordinate via a Taylor approximation. In both cases (Stokes-Gell-Mann parameter retrieval and 3D localization) the inversion is based on matrix multiplication operations, hence the algorithm can be used to analyse large data sets. We also discuss the compatibility of this algorithm with other methods based on measuring PSFs. For the case of rectilinear dipoles, we show that it is possible to measure without ambiguity the 3D position of the emitters based on a Taylor expansion. For elliptical dipoles, we show that there is a correlation between the spin terms S_{3j}, S_0 and the spatial variables. Future work could involve finding a system of two polarized channels that completely decouples the spatial and polarization parameters.

We presented Monte Carlo simulations for the case of 3D-oriented rectilinear dipoles and showed the performance in the regimes of high and low photon numbers. We observed similar performance in retrieving localization and orientation information compared to state-of-the-art SMLM and SMOLM techniques. With the advantages of having a small PSF (as we are separating the natural PSF into its circular polarization components, the resulting PSFs being in the diffraction limit) that allow us to use this method in samples with high emitter density. Also, the energy is equally distributed in each polarization channel (for rectilinear dipoles), which for PSF-based methods is desirable since background noise can undermine the information contained in the PSF. Among PSF-based methods to perform orientation microscopy (where the signal is separated into polarization channels), C-3POL is the simplest to implement,

requiring only the addition of a QWP, which is a thin element robust to misalignment.

We also present Monte Carlo simulations for the case of 3D-oriented elliptical dipoles and show that, in situations of high photon number, it is possible to retrieve the spin direction and the ratio between the minor and major axes of the ellipse. We show the bias on the localization parameters induced by the correlation between the spin components and the spatial parameters. The Monte Carlo results are valid in situations of a perfect matching of the PSF pair. Future work can be dedicated to studying the effect of possible errors during the matching process and how to correct them. In the next chapters, we discuss the application of C-3POL in non-paraxial polarimetry and single molecule orientation microscopy.

5. Nonparaxial polarimetry.

Sommaire

5.1. Introduction 99
5.2. Generating nonparaxial fields. 100
5.3. Experimental results. 101
5.3.1. Measurements of constant linearly polarized fields exhibiting 3D orientations. 101
5.3.2. Measurements of 3D-oriented ellipses of polarization with opposite handedness. 106
5.3.3. Measurement of the interference pattern of two p-polarized waves. 107
5.4. Final remarks. 109

5.1. Introduction

In this chapter, we explain a method to perform nonparaxial polarimetry of electric fields with nanometric resolution in a single shot. We start by explaining the experimental setup, the field generation and finally the experimental results. In Chapter 1 we presented experimental methods based on the interaction of a Mie scatterer with a complex polarized electric field at nanoscales and the measurement of the scattered signal at the pupil plane.

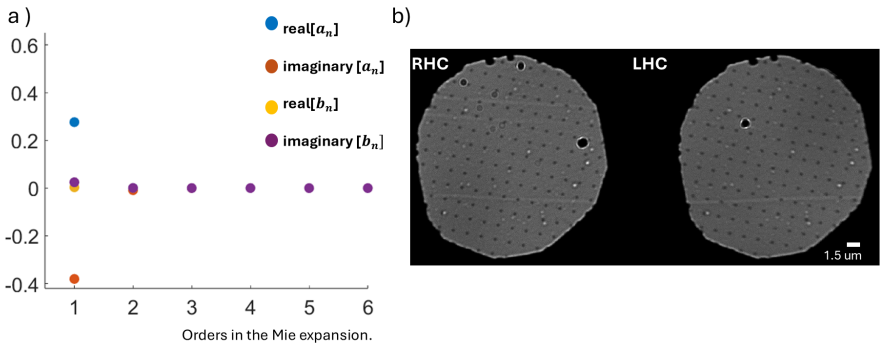

Figure 5.1.: a) Mie coefficients of a nanogold sphere of 80 nm of diameter immersed in an index $n = 1.518$ at $\lambda = 532$ nm We observe that the dominant contributions come from the dipolar electric terms a_n. The coefficients were computed with the algorithm presented in Ref. [79]. b) Duplicated image of the array of gold nanospheres observed in transmission mode illuminated with white light.

Here we propose to encode in the radiation from dipole scatterers the field's ($\lambda = 532nm$) polarization information. Instead of a single dipole, we propose to use a square array of gold nanospheres of 80 nm of diameter, as shown in Fig. 5.1a at this wavelength and in a surrounding medium of index $n = 1.518$, the dominant coefficients in the Mie expansion are the ones corresponding to electric dipolar contributions [79]. The spheres can then be regarded as Rayleigh scatterers. This allows us to assume that the induced dipole on each particle is proportional to the external electric field $\hat{\boldsymbol{\mu}} \propto \mathbf{E}_{\text{ext}}$. The sample of nanospheres is deposited on a coverslip and it was fabricated by the nano and microfabrication platform PLANETE of the Interdisciplinary Center of Nanoscience of Marseille (CINaM). For the experimental results presented in this Chapter, the distance between the particles can be 1.5μm or 2μm. As linear scattering is a coherent process, the PSFs of neighbouring particles can interfere coherently, leading to PSFs that cannot be described by the model proposed in Chapter 6. Hence, these separations were chosen to avoid crosstalk between the particles' PSFs.

Figure 5.1b shows the duplicated image of the array observed with the detection system described in Chapter 4 when the particles are illuminated with white light in transmission mode.

5.2. Generating nonparaxial fields.

In Chapter 2 we described a setup used to generate arbitrarily polarized paraxial fields. This unit is also used to generate polarization distributions at nanoscales. With two 4f systems, we project the SLM Fourier plane at the entrance of an ×100, NA 1.49 oil-immersion objective (Nikon, CFI Apochromat). In this configuration, we have control of the angular spectrum of the nonparaxial field. The beam preparation unit and the detection path were built during this thesis project.

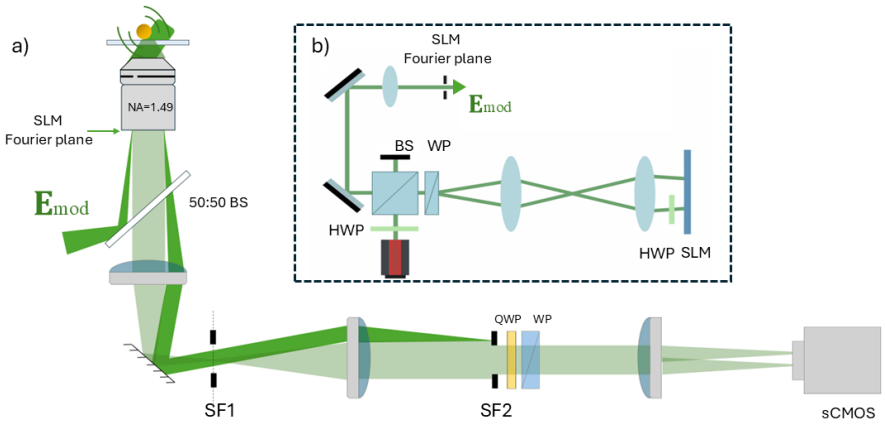

Figure 5.2.: a) Observation of gold nanoparticles in dark-field configuration and b) illumination unit.

The modulated field $\mathbf{E}_{\text{mod}}$ ($\lambda = 532$ nm, Oxxius LCX-532L) is typically focused at the

objective back focal plane. The particles are surrounded by immersion oil to match the refractive index of the cover slip. The incoming beam and the scattered field are separated with a 50:50 beam splitter (Thorlabs, BSW4R-532). We experimentally verified that this element does not add significant polarization distortions to the reflected and transmitted beams. The signal is sent to the detection unit described in Chapter 4. Despite the index matching in the sample, there are some specular reflections of $\mathbf{E}_{mod}$ that are removed at the Fourier plane in the detection path with a spatial filter (SF2).

5.3. Experimental results.

5.3.1. Measurements of constant linearly polarized fields exhibiting 3D orientations.

To show the capabilities of C-3POL to distinguish 3D-oriented dipoles we generate transverse dipoles (contained in the sample plane, with $\eta = 90°$) and dipoles with a significant longitudinal component ($90° > \eta > 0°$). In both cases, we explore 8 different in-plane orientations ξ =0 °, 45°, 90°, 135°, 180°, 225°, 270° and 315°. With the illumination unit, we generate focused beams at the entrance of the objective at 8 different locations. Each wave is linearly polarized in the radial (p) or azimuthal (s) direction. This polarization is controlled with a HWP placed in the illumination path. The objective then collimates the beam that uniformly illuminates the particle sample: s-waves generate in-plane dipoles, whereas p-waves generate dipoles with longitudinal components. Depending on the position of the focused beam at the pupil

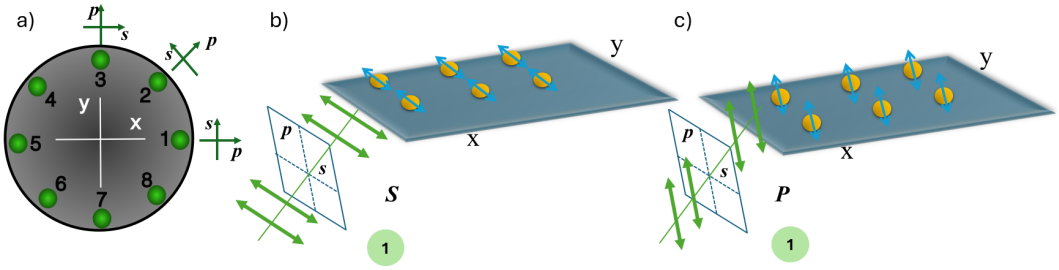

Figure 5.3.: a) Representation of the focusing of a beam at eight different locations in the back focal plane and the possible polarizations s and p. b) Generation of in-plane dipoles by illuminating the particles with a s-polarized wave. c) Generation of dipoles with a significant longitudinal component by illuminating the particles with a p-polarized wave.

plane, we could generate eight different in-plane orientations at the sample plane. The representation of the polarization and location of the waves at the objective entrance is shown in Fig. 5.3. We illuminate sequentially the sample with one wave and one polarization. Before starting the acquisition we perform calibration measurements.

We measure the diameter of the pattern at the pupil plane before and after removing the high NA contributions that contain the reflected illumination, as shown in Fig. 5.4a. By computing the ratio between the two diameters we estimate an effective collection aperture of NA ~ 1.26.

As expected, we observe in the PSFs corresponding to s-polarized illumination, that the resulting PSFs resemble simple 2D Gaussian distributions slightly elongated along the illumination polarization. We use these patterns to perform the affine transformation calibration. In the intensity distributions corresponding to p-polarized illumination, we observe the expected deformed PSFs with a clear zero of intensity. Similar PSF shapes are observed for the other illuminations.

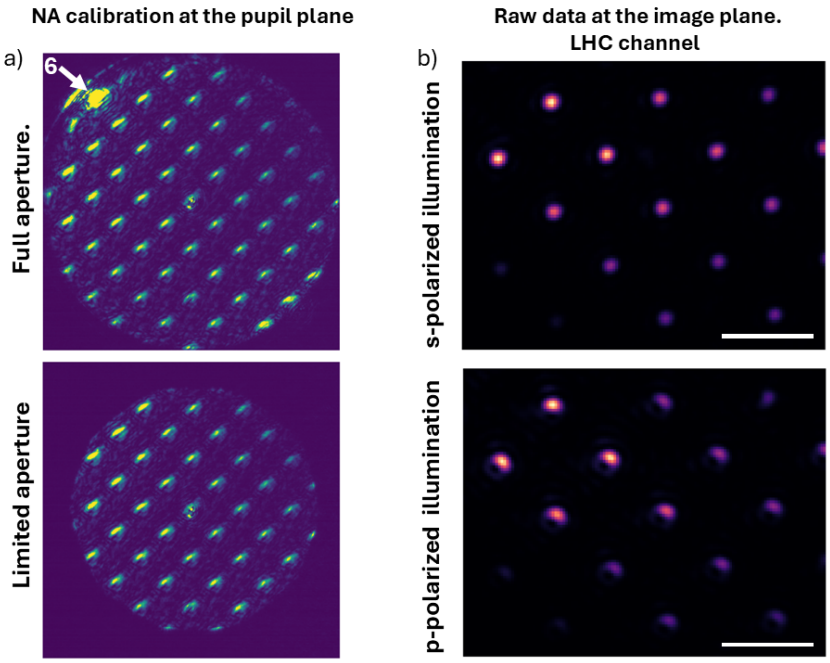

Figure 5.4.: a) The top image shows the intensity distribution at the pupil plane of the LHC component when SF2 is fully open. The brightest spot (at the upper left corner) corresponds to the reflected illumination beam. The image at the bottom shows the aperture after removing the high NA contributions. The array of spots does not correspond to the particle array, it is an interference pattern at the pupil plane with a periodic structure due to the periodic array of particles. b) Raw data showing the same FOV under different polarized illuminations. Note the high SNR. (Scale bar 1.7 μm)

In Fig. 5.5 we show images and statistics corresponding to the dipoles generated with sequential s-polarized illuminations. In this case, we project our measurements on the complete Stokes-Gell-Mann basis calculated for emitters placed at the focal plane as explained in Chapter 4. The dipole is then represented with a 3D-oriented ellipse calculated from the estimated electric field $\hat{\boldsymbol{E}}$, defined in Eq. (1.17) corresponding to the largest eigenvector of Γ_{3D}. Note that most of the ellipses are significantly narrow.

In Fig. 5.5c we present the histogram of the ratio between the minor and major axes of this ellipse r_{ba}. We measure an average value of $\langle r_{ba}\rangle = 0.18$ and $\sigma_{r_{ba}} = 0.15$. Notice that the peak of the distribution is around ~0.1. We also present the histogram of the major axis' off-plane angle η_A. We measure a mean value of $\langle \eta_A\rangle = 76.27\ ^\circ$ and $\sigma_{\eta_A} = 10.7^\circ$, although the peak is at 90°. This reveals that the ellipses are mostly contained within the plane. Finally, we present the degree of polarization P centered at $\langle P\rangle = 0.47$ with $\sigma_P = 0.14$. These values are consistent with the precision calculated in Chapter 6 where a high bias on P was observed. Those simulations, however, did not consider possible errors in the PSF pairing or distortions of the illumination polarization due to its transmission through the microscope. Despite these possible sources of bias, our measurements are consistent with a linearly polarized field, parallel to the sample plane illuminating the sample. We can also observe that the in-plane orientation follows, on average, the expected direction. We select data from four different illuminations, denoted in Fig. 5.6 as ξ_j, and plot the corresponding polar histogram displayed in Fig. 5.6d. We can see that the distributions are centered approximately along the vertical, anti-diagonal, horizontal and diagonal axes. The corresponding mean values are $\langle \xi_1\rangle = 90.7^\circ$, $\sigma_1 = 32.0\ ^\circ$, $\langle \xi_2\rangle = 129.7\ ^\circ$, $\sigma_2 = 27.6\ ^\circ$, $\langle \xi_3\rangle = 0.3\ ^\circ$, $\sigma_3 = 22.7\ ^\circ$, $\langle \xi_4\rangle = 44.4\ ^\circ$, $\sigma_4 = 29^\circ$. Notice that for rectilinear dipoles such as $\eta \approx 90^\circ$, small fluctuations could lead to significant changes in the value of ξ. This angle is defined from $[0^\circ, 360^\circ]$, hence if $\eta = 90^\circ$, ξ and $\xi + 180^\circ$ represent the same physical situation. This is why we show $\xi = \mathrm{mod}(\xi, 180^\circ)$. If we now analyze the situation where the eight illumination waves are p-polarized we can notice that the measured distribution of η_A changes significantly, its average value being now centered at 29.4° with $\sigma_{\eta A} = 16^\circ$ and the peak being at ~ 25°. This value is consistent with the illumination beams being focused almost at the edge of the aperture, which induces a significant longitudinal component of the excitation field. In the case of a perfect plane wave illumination, the expected angle is given by $\eta = \mathrm{asin}(\mathrm{NA}_0/1.518)$, where NA_0 is the associated aperture to the position of the focused beam. For an angle or $\eta = 25^\circ$ this corresponds to 1.37 which represents 0.9 of the complete aperture. In the distribution of r_{ba}, shown in Fig. 5.6b we corroborate that most of the measured ellipses are narrow. We notice in Fig. 5.6a,d that in this situation where $\eta < 90$ it is possible to identify the angle ξ in the complete range $[0^\circ, 360^\circ]$, the color associated with the measured angle matching the expected distribution. This proves that we can measure the 3D orientation of rectilinear dipoles with no ambiguity. We notice that the distribution of the measured P is now closer to the value of a fully polarized beam, which is consistent for dipoles with small η. This change is consistent with the expected bias due to the similarity between I_0 and I_{12}, as illustrated in Fig. 4.5c . In d) we show polar distributions of ξ corresponding to the labeled regions in Fig 5.6a. The corresponding mean values are consistent with the expected in-plane orientations with $\langle \xi_1\rangle = 182.60^\circ$, $\sigma_1 = 31.7\ ^\circ$, $\langle \xi_2\rangle = 220.7\ ^\circ$, $\sigma_2 = 37.24\ ^\circ$, $\langle \xi_3\rangle = 264.1\ ^\circ$, $\sigma_3 = 25.24\ ^\circ$, $\langle \xi_4\rangle = 297.9\ ^\circ$, $\sigma_4 = 48.0^\circ$.

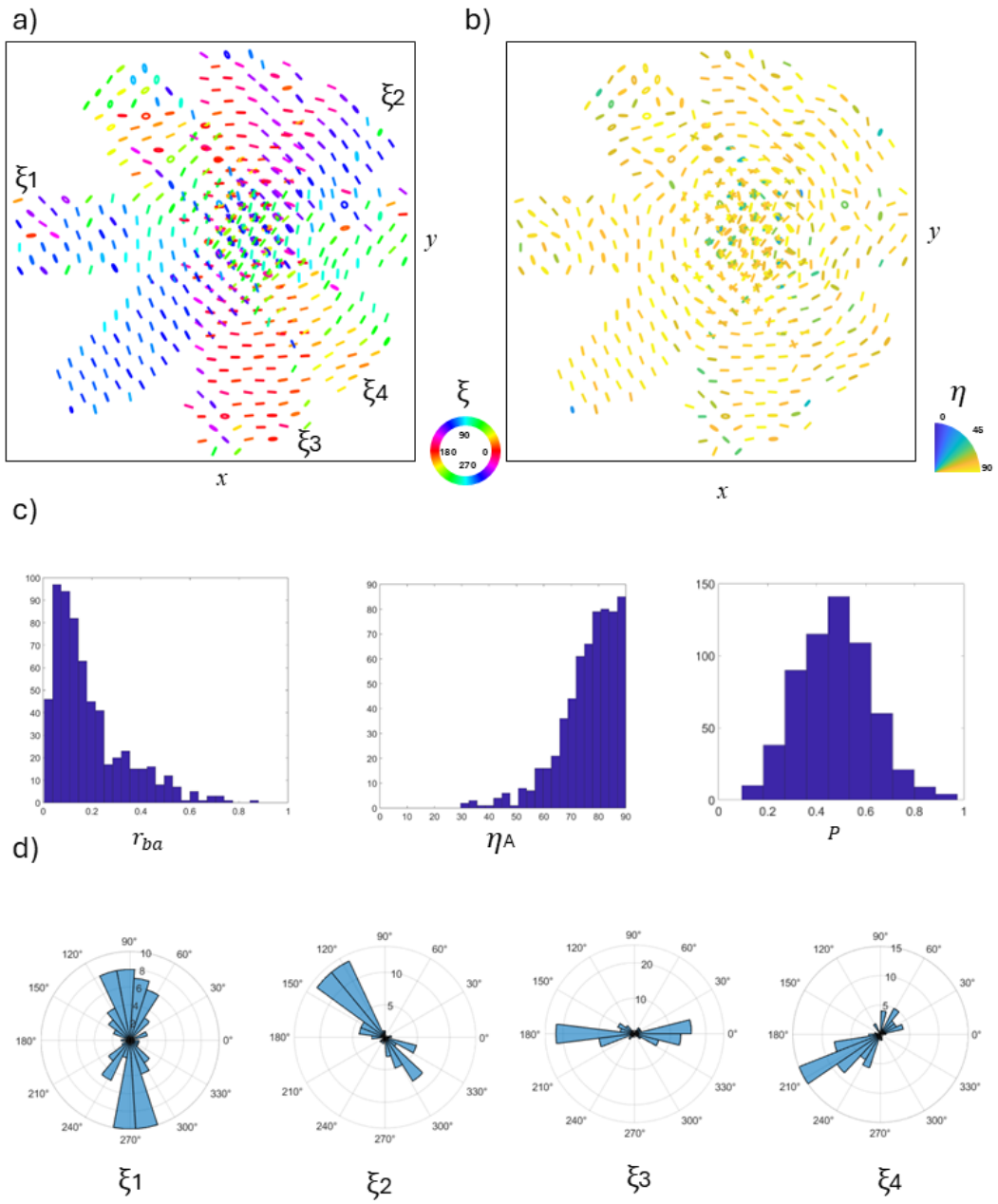

Figure 5.5.: Compound image of measured dipoles generated with s-polarized waves. a) 2D localized ellipses, where the color represents the angle ξ of the ellipse major axis. b) Same as in a) but the color now represents the off-plane angle of the major axis. c) Histograms of the ratio between the minor and major ellipse axes, the angle η associated to the largest axis and the recovered degree of polarization. d) Polar histograms of the in-plane angle of the ellipse's major axis corresponding to the label regions in a).

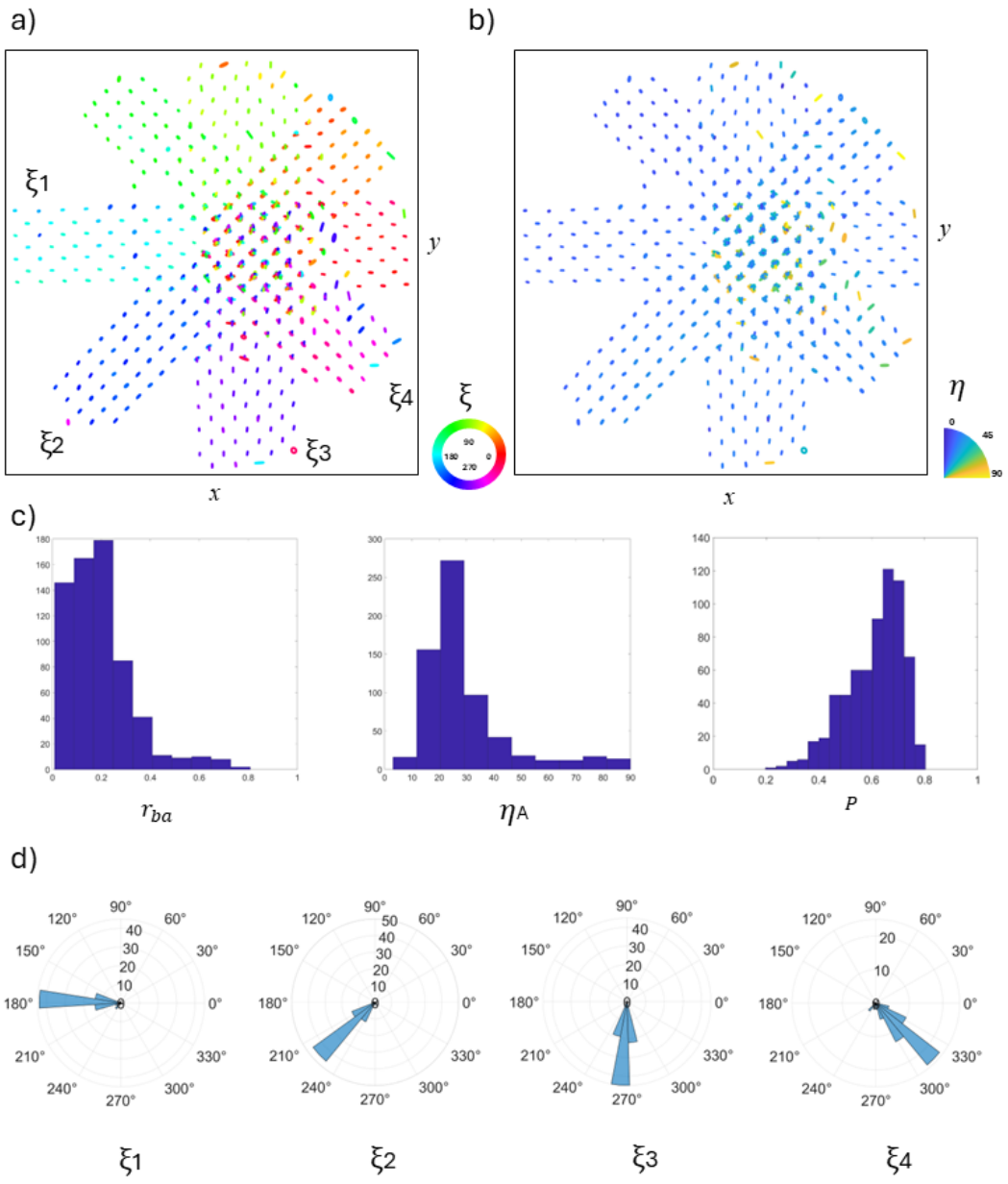

Figure 5.6.: Compound image of measured dipoles generated with p-polarized waves. a) 2D localized ellipses, where the color represents the in-plane angle ξ of the ellipse major axis. b) Same as in a) but the color now represents the angle η of the major axis. c) Histograms of the ratio between the minor and major ellipse axes, the angle η associated with the largest axis and the recovered degree of polarization P. d) Polar histograms of the angle ξ of the ellipse's major axis corresponding to the labeled regions in a).

5.3.2. Measurements of 3D-oriented ellipses of polarization with opposite handedness.

We now present the results of 3D-oriented ellipses. An elliptically polarized beam is focused close to the border of the objective back aperture. In each measurement, we change the handedness of the illumination to generate different directions of the spin vector in the sample plane.

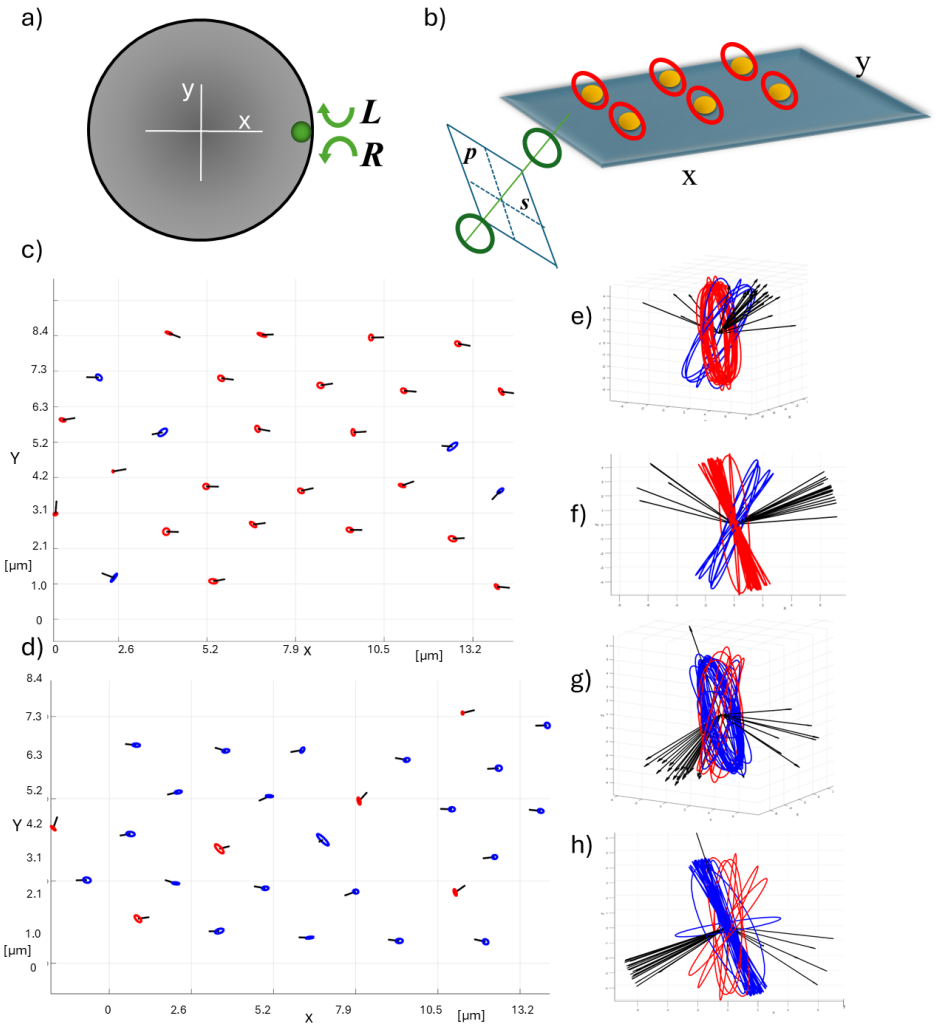

Figure 5.7.: 3D ellipse of polarization. a) Generation of a 3D-oriented polarization ellipse by focusing an elliptically polarized beam at the entrance of an objective b) Illumination of the particles with an elliptical beam with significant longitudinal component. c)-d) Spatially distributed measurements. e)-h) Compound image with all the ellipses.

The experiment is illustrated in 5.7a-b and the results are shown in 5.7c-h. First, we show the measured spatially distributed polarization ellipses in Fig. 5.7c-d. Figure

5.7c shows the ellipses resulting from illuminating the particles with a left-polarized beam and 5.7d shows the ellipses produced by a right-polarized illumination.

Unlike the previous experiments with s- and p-polarized waves, we observe that the ellipses are no longer narrow. The black arrow represents the spin vector calculated using Eq(1.18). The ellipse color indicates the sign of the s_x component of the spin vector. For the ellipses in red, we measure an average normalized spin vector $\langle \mathbf{s} \rangle = (0.57, 0.03, -0.34)$ with $\sigma = (0.69, 0.27, 0.11)$, and for the blue ellipses, $\langle \mathbf{s} \rangle = (-0.49, 0.14, 0.33)$ with $\sigma = (0.68, 0.33, 0.26)$. Hence, on average, the two mean vectors are pointing in opposite directions, which is consistent with the change in the handedness of the illumination. This is illustrated in Fig. 5.7e,g showing the overlapped ellipses in 3D and projected on the $y-z$ plane in 5.7f,h.

5.3.3. Measurement of the interference pattern of two p-polarized waves.

So far, we have only described the measurement of fields that exhibit a constant polarization pattern across the sample plane. In this section, we explain how to generate and measure subwavelength variations of polarization.

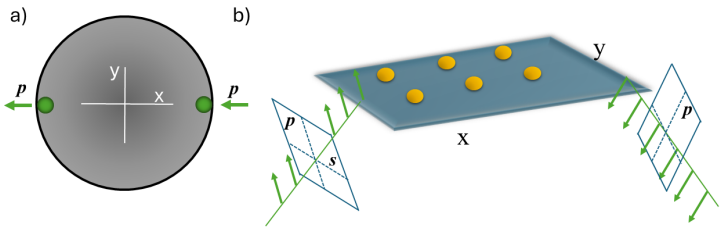

Figure 5.8.: Interference of two p-polarized waves by focusing two p-polarized beams at the edges of the objective back aperture.

With the illumination unit described earlier, we generate two linearly polarized beams focused at opposite extremes of the objective entrance as illustrated in Fig. 5.8a. Since the particles are immersed in a medium of index $n = 1.518$ that matches the coverslip index, we can neglect the effects of the interface and approximate the resulting pattern as the interference between two plane waves at the sample plane. Mathematically, this can be written as

$$\mathbf{E}_{Int}(x,y) \approx e^{ik_x x}(\cos\theta, 0, -\sin\theta) + e^{-ik_x x}(\cos\theta, 0, \sin\theta), \tag{5.1}$$

where θ is the angle between the wave vector and the z axis, and the minus sign in the z-component of the first term is a consequence of the locations of the focused beams at the pupil plane. The field can be simplified as $\mathbf{E}_{Int}(x,y) = (i2\sin k_x x\cos\theta, 0, 2\cos k_x x\sin\theta)$. This expression describes an elliptically polarized field contained in the $x-z$ plane with two extreme cases: $\sin k_x x = N_s\pi$, with N_s an integer, corresponding to a purely

linear longitudinal polarization and $\cos k_x x = N_c \pi/2$, with N_c an odd integer, corresponding to a purely linear transverse polarization. Note that for points such as $k_x x \in [0\,, \pi/2)$ and $k_x x \in [\pi\,, 3\pi/2)$ the two components have the same sign whereas for the points such as $k_x x \in [\pi/2\,, \pi)$ and $k_x x \in [3\pi/2\,, 2\pi)$ there is a sign difference between them. This means that the direction of the spin vector changes spatially and the regions of constant spin direction are limited by the points of linear polarization. Hence, in the domain $k_x x \in [0, \pi]$ the field explores all possible ellipticities. To have an approximation of the spatial variations in the interference pattern it is useful to compute the value of x such as $k_x x = \pi$. Let us assume that we focus the beams exactly at the border of the objective aperture such as $\theta = \text{asin}(NA/n_0) \approx 78.9°$. The term k_x is given by $k_x = n_0 k_0 \sin\theta$. From the previous equation, $x = \lambda/(2n_0 \sin\theta)$, for the extreme case of $\theta = 78.9$, $x \approx 178.6$ nm. Given the particle separation in the array (1.5 μm, 2.0 μm), it is impossible to resolve these subwavelength variations in a single shot. We propose then to displace the particle array along the x-direction with an $x-y$ piezo stage (Physik Instrumente) in steps of 100 nm, and to measure the signal in video mode at 10 frames/s, to capture the particle during its displacement.

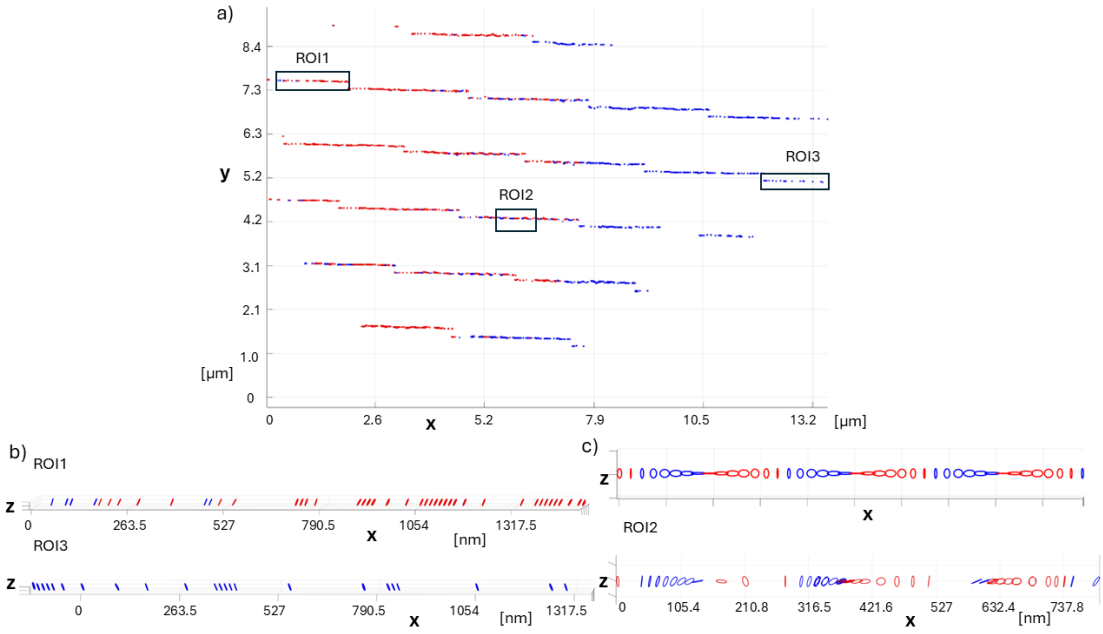

Figure 5.9.: Measurement of sub-wavelength variations of the electric field by displacing the particle with a $x-y$ piezo stage. a) Complete FOV, b) ROIs at the extremes of the interference region presenting only linear polarizations, with opposite in-plane angles. c) Comparison between simulation and measurements. The ellipses' color indicates the sign of the y-component of the spin vector.

The reconstructed polarization ellipse distribution is shown in Fig. 5.9a. We resolve the interference in an area of $\sim 8.4 \times 13.2 \mu m^2$. In the central part of the interference pattern, we expect to observe the earlier described polarization variations whereas at the extremes we expect to observe a constant linear polarization. We use this pre-

knowledge on the expected field at the extremes of the interference pattern to select the Stokes-Gell-Mann basis associated with the correct amount of defocus (in this case $z_0 = 100$nm) such as we measure linear polarization at the extremes.

In Fig. 5.9b we show the recovered polarization ellipse at the left and right sides of the FOV, with parameters $r_{ba} = 0.09$, $\sigma_{rba} = 0.03$, and $r_{ba} = 0.09$, $\sigma_{rba} = 0.05$ respectively, showing that the field is polarized as a narrow ellipse. In Fig. 5.9c we show a comparison between the simulated polarization ellipses and the measurements. Note that we can resolve the spin sign, encoded by the color, and changes from longitudinal to transverse linear polarization. The intermediate polarization ellipses are also resolved, although there is an inclination of the major axis orientation, which can be explained by the natural bias described by the coupling between the spin and the spatial parameters discussed in the previous chapter. The measured distance between two longitudinal ellipses is ≈ 210 nm, which is equivalent to an angle $\theta = 56.5^\circ$ (note that the angle can be higher since the particle array moves in a rectilinear trajectory with an small angle to the x-axis). This value of θ is related to the situation where the two beams are focused at a diameter that represents 0.85 of the complete aperture, which is consistent with our illumination configuration. We acquired 200 frames resulting in a total acquisition time of 20 seconds. We precalculate 1024 bases accounting for displacements in $x - y$ of 1/4 pixel size. The initial PSF localization takes ~ 30 s whereas the Stokes-Gell-Mann parameters estimation time is around ~ 1 min for 3398 PSFs.

5.4. Final remarks.

We have applied C-3POL to the measurement of the dipole moment induced on an array of gold nanospheres by 3D polarized illuminations. We have tested the performance of the method in situations of linear and elliptical polarizations. We show that we can resolve the full hemisphere of 3D orientations by inducing in-plane and off-plane dipoles aligned to the positive and negative directions of the **x**, **y**, **p** and **m** axes. We also show that we can distinguish between in-plane and off-plane dipoles with an accuracy in agreement with the simulations presented in the previous chapter. We also prove that we can measure the 3D oriented spin vector of elliptical dipoles. Our method is the first among all the previous approaches to completely describe the measurement process and the data analysis in terms of a set of nine parameters. This is a generalization of the widely known Stokes parameters used to describe paraxial states of polarization.

Compared to other methods measuring the local electric field at nanoscales with nanoprobes, our approach is capable of measuring simultaneously at different points the electric field polarization in a larger FOV. We can generate images that resemble the ones obtained in paraxial polarimetry where at every single pixel on the camera there is a measurement of the polarization ellipse. Here the array of gold nanoparticles is equivalent to the camera pixel, with the difference that we can resolve 3D-oriented ellipses of polarization.

We prove that, when the particle is displaced with a piezo-stage and the camera is in video mode, it is possible to resolve subwavelength ($\leq$ 100 nm) variations of polarization. It is possible to reconstruct spatially variant polarization maps of the 3D oriented polarization ellipses at nanoscales, that resemble the 2D polarization maps presented in Chapter 2. As discussed in Chapter 4, there is a source of bias in the estimation of the localization and Stokes-Gell-Mann parameters. In the measurement of the interference pattern, we use the basis associated with the amount of defocus that is consistent with having linear polarization at the extremes of the interference pattern. However, this is a solution only for this specific pattern. Future work on this technique can involve designing optimal calibration measurements of the amount of defocus. This calibration can allow not only to improve the estimation of nonparaxial fields constrained in a plane but also to perform volumetric polarization measurements.

6. Stokes-Gell-Mann formalism applied to SMOLM.

Sommaire

6.1. Introduction. 111
6.2. Photoselection of single 3D-oriented fluorophores on a coverslip by varying the excitation polarization. 111
6.3. C-3POL applied to STORM. 114
6.4. Final remarks 117

6.1. Introduction.

In this chapter, we present examples of C-3POL applied to fluorescence microscopy. We show measurements of sparse AlexaFluor 532 fluorophores deposited on a cover slip exhibiting random 3D orientation under s- and p- polarized illumination configurations and super-resolved images of fixed actin in cells labelled with phalloidin Alexa 568 (sample provided by Charitra Kummar and Shizue Omi-Massieau).

6.2. Photoselection of single 3D-oriented fluorophores on a coverslip by varying the excitation polarization.

Fluorescence is a two-step process that involves the dipole absorption moment $\hat{\boldsymbol{\mu}}_{abs}$, the external excitation $\mathbf{E}_{ext}$ and the emission dipole moment $\hat{\boldsymbol{\mu}}_{em}$. The probability of a dipole to absorb is given by $P_{abs} = |\mathbf{E}\cdot\hat{\boldsymbol{\mu}}_{abs}|$. For the measured fluorescent molecules in this work, we can assume that the absorption and emission dipoles are aligned [80]. This suggests that if we restrict the excitation field to a specific direction of oscillation, then those molecules that are parallel to the external excitation are more likely to be excited and detected. We perform experiments in the same setup described in previous chapters with some minimal modifications. We replace the 50:50 BS by a dichroic mirror and introduce a bandpass filter to remove the excitation from the emission. We fully open the second spatial filter, so the collection aperture is NA=1.49, and we place a broadband QWP in the detection path. Similarly, we use p- and s-

polarized excitations in Total Internal Reflection Fluorescence TIRF configuration. The illustration of the setup is shown in Fig. 6.1.

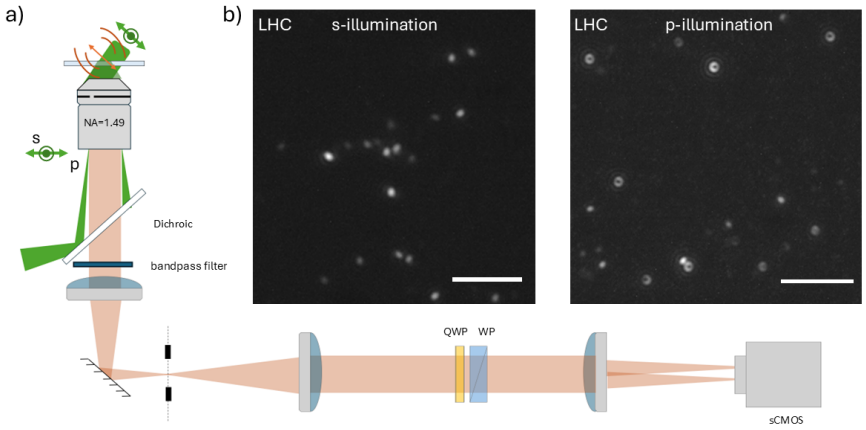

Figure 6.1.: a) Set up and b) raw images in the LHC of 2D located molecules excited with s- and p-polarized illumination. Note the difference in the PSF shapes related to the external electric field. The image contrast was modified to highlight the PSFs. (Scale bar 2.8 μm and 3.5 μm respectively).

For the s-polarized illumination, we expect to mostly detect molecules parallel to the coverslip and for p-polarization, we expect to detect molecules with a significant off-plane component, as shown in early work on single 3D oriented molecules [81]. Whereas the s-polarized illumination remains linearly polarized after passing through the glass-water interface, the longitudinal and transverse components of the p-illumination are phase-shifted resulting in an elliptically polarized illumination. For the experiments, we prepared a sample of sparse Alexa 532 deposited on a coverslip immersed in water attached to Polylisine (PLL). We measured a stack of 500 frames with an exposure time of 200 ms. We analyzed the data with the same algorithm described in Chapter 4. In this case, it is known that the molecules are located over the coverslip, hence in the partial derivatives basis computation we perform the axial derivative on the spatial coordinate d that accounts for displacements of the water-glass interface to the focal plane. In Fig. 6.1b we show images of PSFs within the same FOV under different polarized illuminations. We clearly notice a difference in the measured PSF shapes. In the s-polarization condition, we observe elongated 2D Gaussian distributions and in the p-polarized illumination, we observe several doughnut-like PSFs. This illustrates another useful feature of C-3POL: when the contrast is adjusted in the camera during the live mode it is possible to distinguish by eye if the illuminations correspond to s- or p-polarization. Some results of these experiments are shown in Fig. 6.2a-b. We observe in Fig. 6.2a in the representation of the dipole orientation and in the polar distributions that the measured molecules are mostly aligned with the y axis. In this case, the sticks represent the expected dipole orientations and the colors represent the in-plane and off-plane angle. The strong photoselection is reflected in the color uniformity displayed for the in-plane angle.

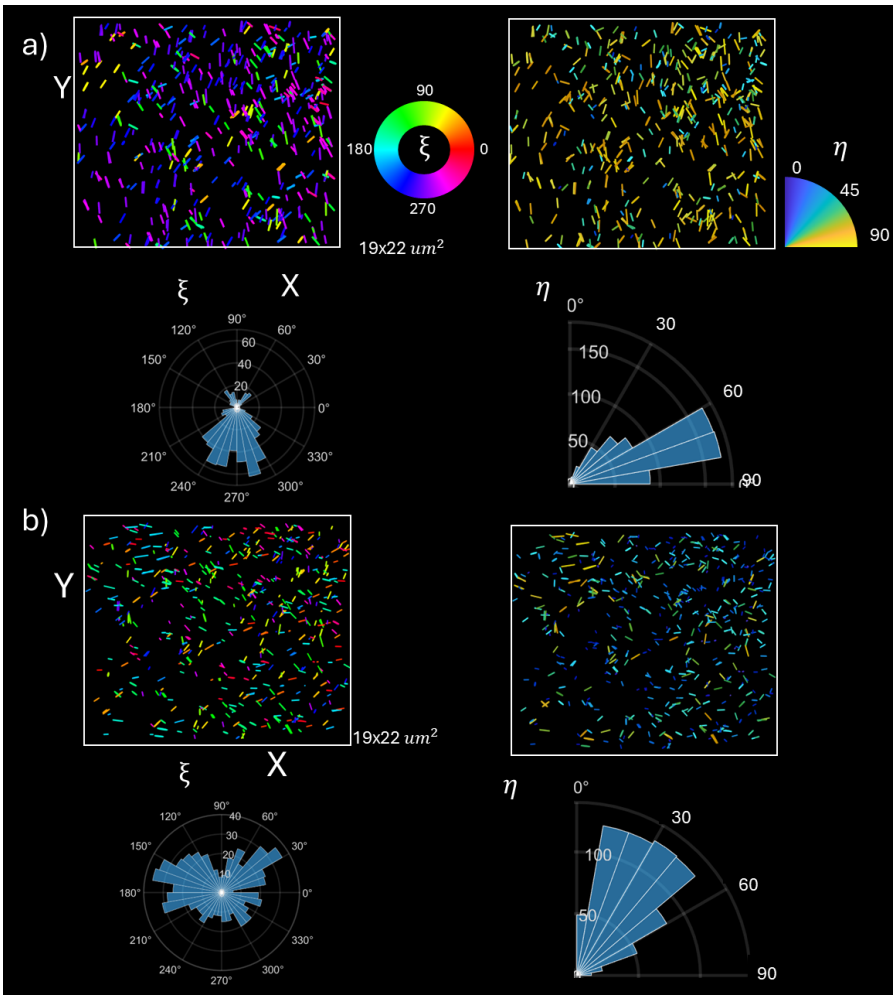

Figure 6.2.: Alexa 532 on a coverslip illuminated with s- and p- waves. 2D localizations and polar histograms of single molecules within a FOV of 19×22 μm^2. The sticks represent the actual 3D orientation and the colors the in-plane and off-plane angles for a) s-polarized and p-polarized illuminations.

In Fig. 6.2b we show results for p-polarized illumination. In this case, we notice that directionality in the in-plane angle disappears and that the polar histograms and hence the color associated with the off-plane angle dramatically changes, the peak value of the distribution moving from $\sim 70°$ to $\sim 30°$. The loss of directionality in the measured in-plane angle is explained by the fact that η is an absolute measure of the orientation deviation from the z-axis and hence all molecules with significant longitudinal components can be excited under p-polarized illumination.

6.3. C-3POL applied to STORM.

STORM is one of the several techniques developed in the early 2000s [8] that surpass the diffraction limit by localizing individual fluorophores photo-activated in a stochastic manner. A super-resolved image of an object can be computed by plotting a Gaussian distribution centered at the measured 2D position with a standard deviation equal to the precision of the center estimation. C-3POL is based on the individual detection of dipole sources, which makes it compatible with STORM. Furthermore, we showed in Chapter 4 that in the case of rectilinear dipoles (fluorescent molecules), we can unambiguously decouple the 3D localization and orientation information of rectilinear dipoles with C-3POl. We decided to test the performance of C-3POL in a high emitter density that naturally exhibits low SNR.

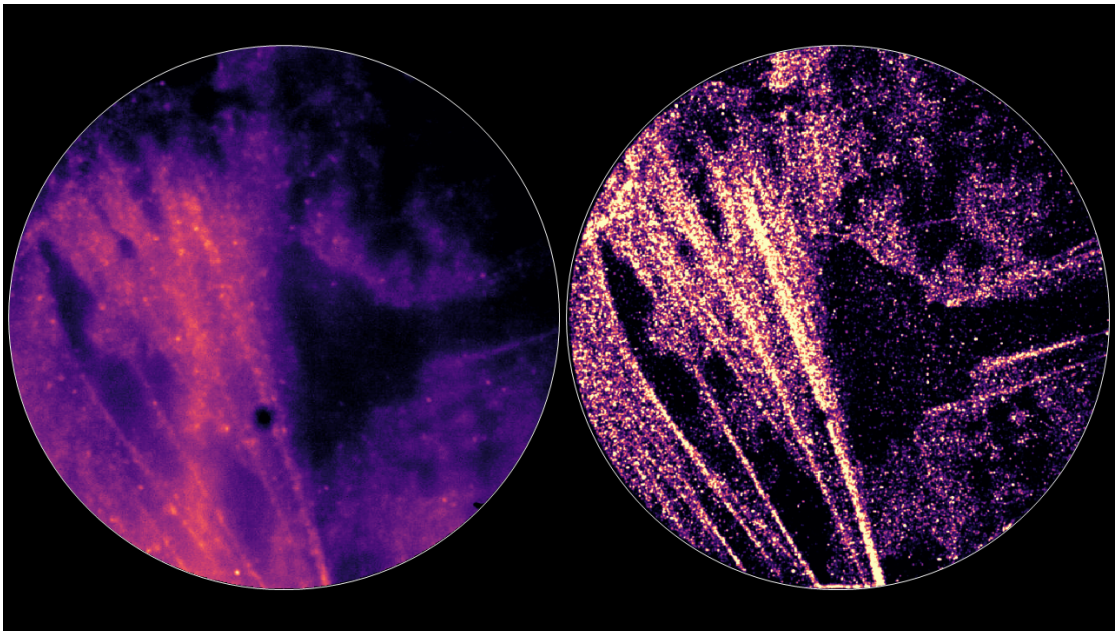

Figure 6.3.: Difraction limited vs STORM image. The image on the left is obtained by averaging 1000 frames from the measurement stack. On the right, the STORM image of fixed actin in cells. The FOV diameter is 36 μm.

We performed measurements on fixed actin in cells labelled with phalloidin Alexa 568 in TIRF configuration with a p-polarized illumination. We construct the super-

resolved image, presented in Fig. 6.3, by plotting 2D Gaussian distributions at each localization point with standard deviation $\sigma_{x,y} = 40nm$. Note that this value is slightly smaller than the pixel size of $52.7nm$. We measure 10k frames with an exposure time of 200 ms and localize ~ 900k fluorophores. The super-resolved image and a comparison with an averaged diffracted limited image are presented in Fig. 6.3. We observe a well-defined structure of stressed fibres that is hidden under the background from out-of-focus contributions. The STORM image is formed with all the detections without any filtering.

In the next graphs, we present the 2D scattered localizations colored according to the measured in-plane angle in Fig 6.4a, off-plane angle in Fig 6.5a, and the axial coordinate in Fig 6.6a. This last variable was estimated via the Taylor expansion dicussed in Chapter 4. This illustrates the power of PSF engineering techniques: 5 orientation+3 spatial parameters can be encoded in the same PSF distributed in two polarized channels measured on the same camera in a single shot.

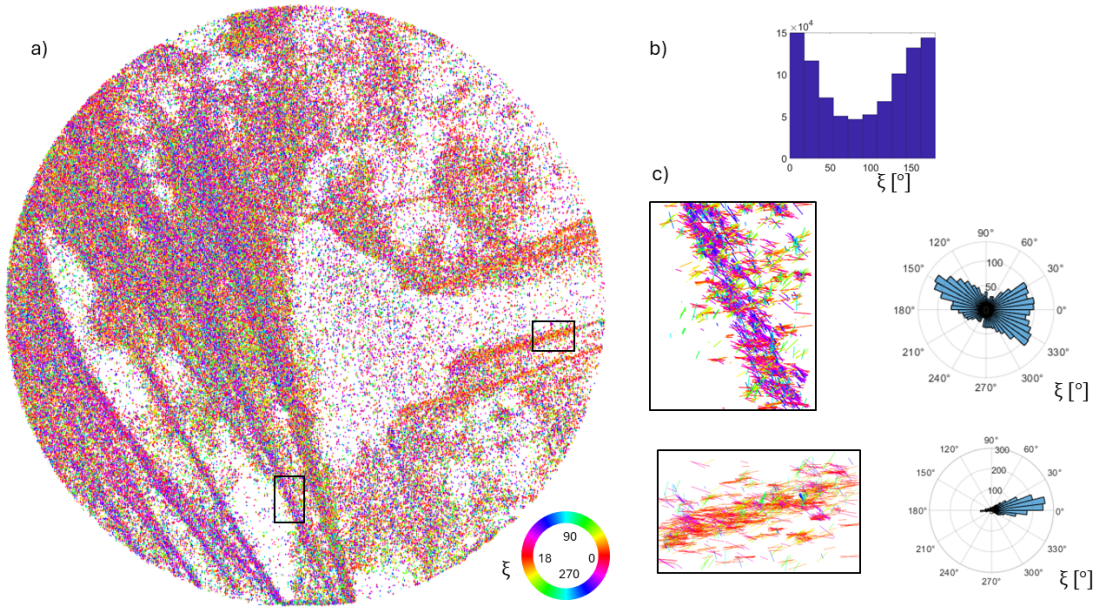

Figure 6.4.: a) 2D scattered localizations colored according to the in plane ξ orientation of Alexa 568. Note that the angle is represented up to a modulus of 180°. b) Histogram of all the measured angles ξ. c) Example of two ROIs having different distributions of the measured ξ. The sticks represent the actual 3D-oriented dipole.

In Fig. 6.4b we show the complete histogram of all the measured in-plane angles ξ. We clearly see an over-represented population along the horizontal axis. This explains the general uniformity of color on the image. Despite this bias, which can be due to a degree of photoselection introduced by the illumination, or by a small error in the affine transformation calibration, we can identify the stressed fibres from the rest of the cell structure. In 6.4c we show examples of two regions of interest (ROI) that

exhibit different statistics on the measured in-plane angle. By comparing these ROIs with the polar histogram we can identify some correlation with the fiber direction. This is a well-known feature for this kind of sample [60].

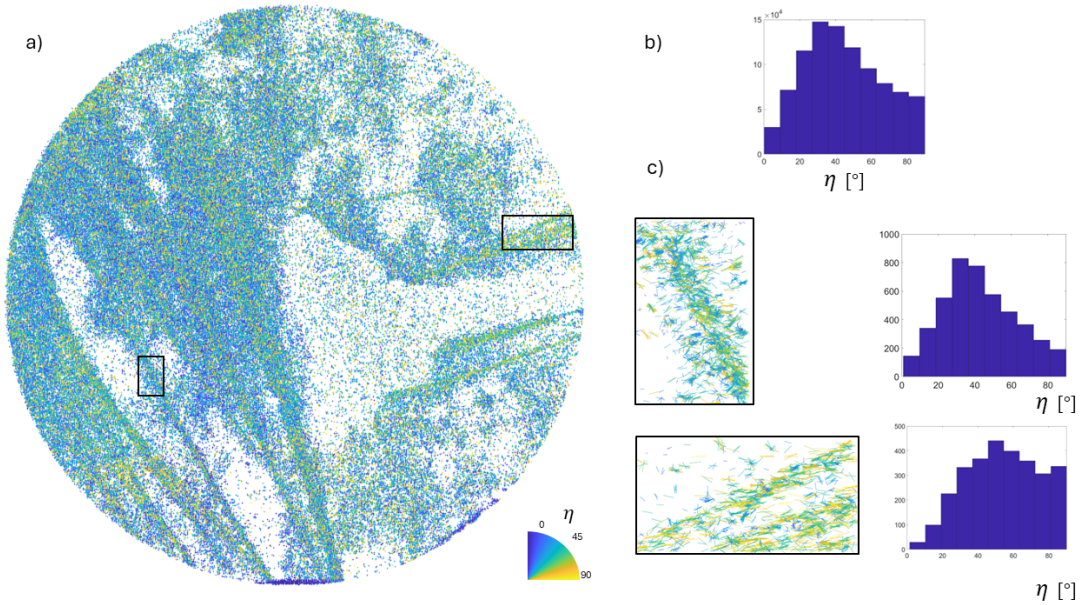

Figure 6.5.: a) 2D scattered localizations colored according to the off-plane η orientation of Alexa 568. b) Histogram of all the measured angles η. c) Example of two ROIs having different distributions of the measured η. The sticks represent the actual 3D-oriented dipole.

In Fig. 6.5b we show the complete histogram of all the measured off-plane angles η. Note that we can cover all the range of expected values with a peak at 30°. This was possible by illuminating the sample with a p-polarized illumination. However, along some stressed fibers, we can see that the predominant off-plane angles are $\eta > 50°$. In 6.5c we show examples of two ROIs that exhibit different statistics on the measured off-plane angle.

In Fig. 6.6b we show the complete histogram of all the measured axial positions z_0. We compute the Stokes-Gell-Mann PSF basis assuming that the interface was located at a constant distance d to the nominal focal plane. This assumption is valid as our microscope is provided with an auto-focus system that keeps the sample position almost constant during the acquisition time. Hence, we calculate the axial derivative for the z_0 coordinate. The range of recovered values is 400 nm, from -100 to 300 nm, with a peak at 100 nm. However, some of those values are non-physical, as z_0 represents the distance to the coverslip which can be only positive. In the 2D scattered plot we restrict the color map to the domain from 0 to 200 nm to highlight the variations in z.

Unfortunately, we do not have a reference position to explain the measured values. The image corresponds to a region where three cells were overlapping. This could

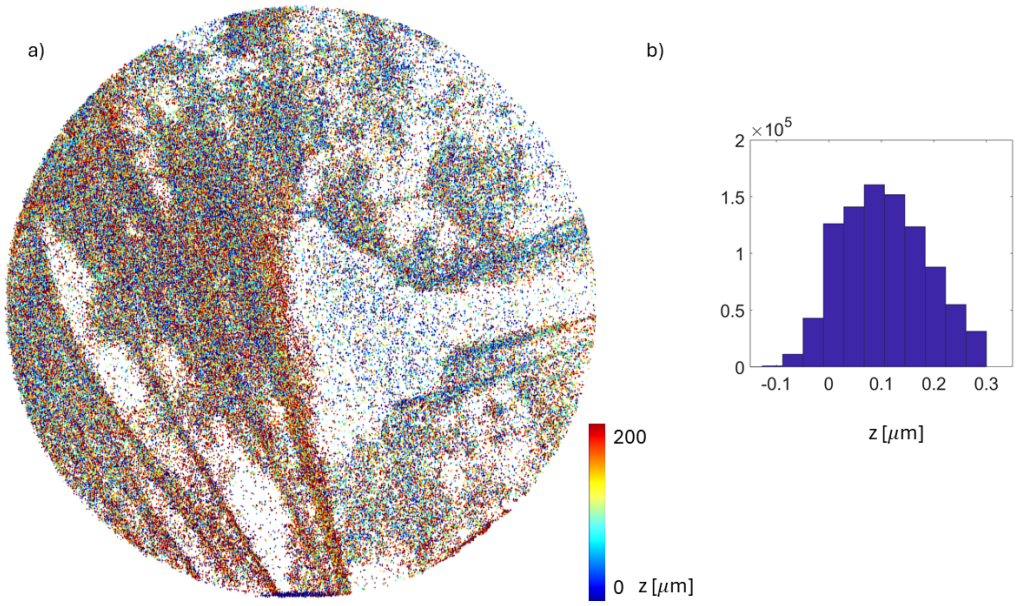

Figure 6.6.: a) 2D scattered localizations colored according to the estimated axial position z_0 of Alexa 568. b) Histogram of all the measured estimated heights. Notice that the limits in the histogram are defined from $-0.1\ \mu m$ to $0.3\ \mu m$, on the other hand. The limits on the colormap are restricted from 0 to $0.2\ \mu m$ to highlight the variations in z.

explain why the group of stressed fibers (mostly in red) on the left seems to be located higher with respect to the cell membrane (mostly in blue) located on the right side. Also, note that in some fibers it is possible to distinguish a smooth color gradient indicating a smooth variation in z.

6.4. Final remarks

In this chapter, we presented experimental results on florescent emitters measured with C-3POL. We show with a sample of single fluorophores under different polarization excitations that we can photo-select populations of molecules based on the external electric field direction of oscillation. This photoselection affects the statistics of the measured fluorophores and it has to be taken into account in any experimental situation where the fluorescent molecules are restricted to wobble at small angles.

We tested the performance of C-3POL in STORM conditions. We showed that with the combined information of the two circular PSFs it is possible to construct a super-resolved image of fixed actin in cells. We also showed that the measured values of ξ and η are consistent with previous work on similar samples and with the illumination polarization. We show results on the estimation of the fluorophores' axial position. Based on the sample features, it is possible to measure a group of stressed fibers at different heights compared to the cell membrane. Also in some stressed

fibres is possible to see some smooth transition from low to high z values. These measurements could indicate that, as the Monte Carlo simulations showed, we are experimentally sensitive to the axial position of fluorophores in cells. Future work can involve changing the illumination polarization during the measurements of cell samples. By changing from s- to p-polarized excitation, it is possible to uniformly excite all possible 3D oriented fluorophores so that the bias due to the photoselection can be reduced. We can also apply our method to the measurement of samples presenting 3D-oriented molecules with known heights, for instance, lipid-coated spheres as in Ref. [33], where the actual height of the fluorophores is known based on their (x, y) position. Compared to state-of-the-art PSF-based methods that achieve simultaneous and unambiguous 3D orientation and 3D position, C-3POL, is the one that offers the smallest PSF size, since it is just the separation of the natural PSF into its circular polarization components. This implies that the method is suitable for measuring samples with a high density of emitters. C-3POL is among the simplest methods in terms of actual experimental implementation, and probably the fastest in terms of data processing. In some state-of-the-art methods, a computational time of $\sim 5h$ to process 5000 frames is reported [33]. In our case, the complete localization and parameter estimation for the STORM data lasted $\sim 2.5h$, analyzing a stack of 10,000 images, with a total of $\sim 925,000$ detections.

Conclusion

This thesis project focused on aspects related to the polarization of light, ranging from the macro to the nanometric scales. We constructed an optical setup to fully modulate the amplitude and phase of paraxial beams to measure polarization states exhibiting all possible 2D ellipses of polarization. The generation and measurement of skyrmionic and meron polarization textures were published recently [40, 41]. The same setup used to design these paraxial polarization states was also used to generate simple non-paraxial states of light. A potential future application is to create more complex polarization structures in the non-paraxial regime.

The other part of the project was focused on the problem of measuring dipole sources with a high NA objective in imaging configuration. We presented theoretical, numerical and experimental results developed during this thesis project. Among the theoretical results, we highlighted the advantages of describing and characterizing microscopes working with PSF-based measurements in terms of the Fisher Information Matrix calculated for the generalized Stokes-Gell-Mann parameters. We also described the advantages of calculating the Stokes-Gell-Mann PSF basis associated with the microscope configuration to obtain physical intuition on the capabilities and limitations of the system. These results are presented in a recent publication [23]. This formalism is not restricted to PSF-based methods. It is always possible to compute the corresponding Stokes-Gell-Mann basis for ratiometric techniques or methods where the measurements are performed at the pupil plane of the objective. In this direction, one interesting question is whether there is a simple radiometric configuration capable of measuring the complete 3D directions of rectilinear dipoles with simple modifications to state-of-the-art techniques.

With the developed theoretical tools, we show that by simply separating the signal from dipole sources into its circular polarization components, the Stokes parameters are unambiguously encoded in the PSF shape. We also highlighted some phase symmetries present in the dipole circular polarization components that explain the PSF behavior for rectilinear dipoles such as: the PSF rotation as a function of ξ, and counter rotation as a function of z_0. We discussed how other methods that imprint phase or polarization modulation with phase vortices such as CHIDO [80] and vortex phase modulation [13] exhibit similar PSF behavior. This provides physical insights into the search for the Jones mask that more efficiently encodes the polarization information on the PSF shape.

If we consider the discrete nature of the data, we have shown that the Stokes formalism is useful to retrieve the dipole polarization and spatial information. We show that, when we vectorized our data arrays, we can invert the numerical problem with a simple matrix multiplication. This matrix is constructed from the discrete version

of the Stokes-Gell-Mann PSF basis. This last result is also related to the numerical contributions of this project.

The circular decomposition represents a simple alternative to other methods measuring 3D-oriented dipoles: it is easy to implement and the associated PSFs reach the diffraction limit, as they are the components of the natural PSF of the system. During this PhD project, we built a setup to measure the circular components of dipoles in scattering and fluorescence configurations. To analyze the data we coded an algorithm based on the linearity of the PSFs to the Stokes-Gell-Mann PSF basis. We exploited the physical constraints of the Stokes-Gell-Mann parameters to discard or renormalize some estimated parameters. This allows us to avoid using non-linear optimization routines that might slow down the computational speed. However, this comes at the price of introducing some bias in our measurements. Future directions for this algorithm could be to use the estimated Stokes-Gell-Mann parameters and the spatial coordinates as the starting point of a non-linear optimization algorithm.

We performed Monte Carlo studies showing that our method is competitive in localizing in 3D and retrieving the orientation information of rectilinear dipoles, although its performance at estimating the degree of polarization is diminished by the natural correlations of some Stokes-Gell-Mann parameters. We also performed numerical studies on elliptical dipoles that showed the capabilities of the system for detecting 3D-oriented polarization ellipses and their spin vector. However, there is a natural correlation between the spatial and the Stokes-Gell-Mann parameters that induced bias on the orientation parameters of elliptical dipoles.

In the experimental part, we performed measurements with an array of nanoparticles to prove that our method is sensitive to the 3D nature of the sources. We measured constant 3D oriented linearly and elliptically polarized beams. We also measured the polarization structure resulting of the interference pattern of two p-polarized waves. This pattern presents subwavelength variations of polarization ($\leq$ 100 nm) that we can resolve by displacing the particle with a piezo stage and capturing the measurements in a video mode. A future application of that system is to measure more complex polarization polarization structures presenting variations in the three spatial dimensions.

During the development of our algorithm, it became evident that the spatial and spin parameters are coupled only in the case of elliptical dipoles. This motivates us to look for an experimental configuration that completely decouples the spatial and polarization parameters. We have shown that C-3POL and CHIDO already decouple the spatial and polarization parameters for rectilinear dipoles. Hence, it might be possible that some slight modification of those configurations could provide the missing extra information.

Finally, we performed experiments with fluorescent emitters. We have shown that it is possible to photoselect the population of excited molecules by controlling the polarization illumination and quantifying this photoselection with C-3POL. Once we showed that our method is compatible with fluorescent emitters, we implemented STORM experiments to test the performance of C-3POL in high emitter density and low SNR situations. We were able to compute STORM image of an actin cell by using the

information of ~ 900000 fluorophores. We also retrieved their 3D orientation and 3D localization information. We observed that the estimated orientation parameters are in agreement with previous measurements on this type of sample [60]. However, we observed a strong bias in the measurement of the in-plane angle. Sources of this bias can be the photoselection or errors on the affine transformation calibration. Future directions on this part could involve increasing the number of measured frames, from 10000 to 40000, which is typical for STORM, and controlling the excitation polarization during the measurement process to homogenize the 3D excitation of fluorophores.

As a general improvement for scattering and fluorescence experiments, it can be useful to quantify the field-of-view dependent aberrations. Since we are working in a small region of the accessible FOV, we do not expect to be strongly affected by them [75]. State-of-art algorithms can be used to quantify those aberrations to include them in the Stokes-Gell-Mann PSF basis computation [82] making possible the extension to larger FOVs.

Bibliography

[1] Miguel A. Alonso. “Geometric descriptions for the polarization of nonparaxial light: a tutorial”. In: *Adv. Opt. Photon.* 15.1 (Mar. 2023), pp. 176–235. DOI: 10.1364/AOP.475491. URL: https://opg.optica.org/aop/abstract.cfm?URI=aop-15-1-176 (cit. on pp. 8, 22, 24, 26, 27).

[2] L. Novotny, M. R. Beversluis, K. S. Youngworth, et al. “Longitudinal Field Modes Probed by Single Molecules”. In: *Phys. Rev. Lett.* 86 (23 June 2001), pp. 5251–5254. DOI: 10.1103/PhysRevLett.86.5251. URL: https://link.aps.org/doi/10.1103/PhysRevLett.86.5251 (cit. on pp. 9, 22, 27, 28).

[3] Thomas Bauer, Peter Banzer, Ebrahim Karimi, et al. “Observation of optical polarization Möbius strips”. In: *Science* 347.6225 (2015), pp. 964–966. DOI: 10.1126/science.1260635. eprint: https://www.science.org/doi/pdf/10.1126/science.1260635. URL: https://www.science.org/doi/abs/10.1126/science.1260635 (cit. on pp. 9, 27, 28, 35).

[4] Thomas Bauer, Sergej Orlov, Ulf Peschel, et al. “Nanointerferometric amplitude and phase reconstruction of tightly focused vector beams”. In: *Nature Photonics* 8.1 (2014), pp. 23–27. DOI: 10.1038/nphoton.2013.289. URL: https://doi.org/10.1038/nphoton.2013.289 (cit. on pp. 9, 22, 28, 30).

[5] Oscar G. Rodríguez-Herrera, David Lara, Konstantin Y. Bliokh, et al. “Optical Nanoprobing via Spin-Orbit Interaction of Light”. In: *Phys. Rev. Lett.* 104 (25 June 2010), p. 253601. DOI: 10.1103/PhysRevLett.104.253601. URL: https://link.aps.org/doi/10.1103/PhysRevLett.104.253601 (cit. on pp. 10, 29, 30).

[6] Mickaël Lelek, Melina T. Gyparaki, Gerti Beliu, et al. “Single-molecule localization microscopy”. In: *Nature Reviews Methods Primers* 1.1 (June 2021). ISSN: 2662-8449. DOI: 10.1038/s43586-021-00038-x. URL: http://dx.doi.org/10.1038/s43586-021-00038-x (cit. on pp. 10, 29, 93).

[7] Eric Betzig, George H. Patterson, Rachid Sougrat, et al. “Imaging Intracellular Fluorescent Proteins at Nanometer Resolution”. In: *Science* 313.5793 (Sept. 2006), pp. 1642–1645. ISSN: 1095-9203. DOI: 10.1126/science.1127344. URL: http://dx.doi.org/10.1126/science.1127344 (cit. on pp. 10, 29).

[8] Michael J Rust, Mark Bates, and Xiaowei Zhuang. “Sub-diffraction-limit imaging by stochastic optical reconstruction microscopy (STORM)”. In: *Nature Methods* 3.10 (Aug. 2006), pp. 793–796. ISSN: 1548-7105. DOI: 10.1038/nmeth929. URL: http://dx.doi.org/10.1038/nmeth929 (cit. on pp. 10, 29, 114).

[9] Alexey Sharonov and Robin M. Hochstrasser. "Wide-field subdiffraction imaging by accumulated binding of diffusing probes". In: *Proceedings of the National Academy of Sciences* 103.50 (Dec. 2006), pp. 18911–18916. ISSN: 1091-6490. DOI: 10.1073/pnas.0609643104. URL: http://dx.doi.org/10.1073/pnas.0609643104 (cit. on pp. 10, 29).

[10] J. Enderlein, E. Toprak, and P. R Selvin. "Polarization effect on position accuracy of fluorophore localization". In: *Opt. Express* 14 (2006), pp. 8111–8120. DOI: 10.1364/OE.14.008111 (cit. on pp. 11, 31).

[11] Kim I Mortensen, L Stirling Churchman, James A Spudich, et al. "Optimized localization analysis for single-molecule tracking and super-resolution microscopy". In: *Nature Methods* 7.5 (Apr. 2010), pp. 377–381. ISSN: 1548-7105. DOI: 10.1038/nmeth.1447. URL: http://dx.doi.org/10.1038/nmeth.1447 (cit. on pp. 11, 31, 55, 56, 60, 62).

[12] Mikael P. Backlund, Matthew D. Lew, Adam S. Backer, et al. "The double-helix point spread function enables precise and accurate measurement of 3D single-molecule localization and orientation". In: *Single Molecule Spectroscopy and Superresolution Imaging VI*. Ed. by Jörg Enderlein, Ingo Gregor, Zygmunt K. Gryczynski, et al. Vol. 8590. SPIE, Feb. 2013, p. 85900L. DOI: 10.1117/12.2001671. URL: http://dx.doi.org/10.1117/12.2001671 (cit. on pp. 11, 31, 32).

[13] Christiaan N. Hulleman, Rasmus Ø. Thorsen, Eugene Kim, et al. "Simultaneous orientation and 3D localization microscopy with a Vortex point spread function". In: *Nature Communications* 12.1 (Oct. 2021). DOI: 10.1038/s41467-021-26228-5. URL: https://doi.org/10.1038/s41467-021-26228-5 (cit. on pp. 11, 31, 56, 57, 60–62, 75, 93, 119).

[14] Isael Herrera, Miguel A. Alonso, Luis Aleman-Castaneda, et al. "Stokes-based analysis for the estimation of 3D dipolar emission". In: (Aug. 2024). DOI: 10.1364/opticaopen.26502499.v1. URL: http://dx.doi.org/10.1364/opticaopen.26502499.v1 (cit. on pp. 11, 31).

[15] Lukas Novotny and Bert Hecht. *Principles of Nano-Optics*. Cambridge University Press, Sept. 2012. ISBN: 9780511794193. DOI: 10.1017/cbo9780511794193. URL: http://dx.doi.org/10.1017/CBO9780511794193 (cit. on pp. 20, 50).

[16] Eileen Otte, Kemal Tekce, Sebastian Lamping, et al. "Polarization nano-tomography of tightly focused light landscapes by self-assembled monolayers". In: *Nature Communications* 10.1 (2019), p. 4308. DOI: 10.1038/s41467-019-12127-3. URL: https://doi.org/10.1038/s41467-019-12127-3 (cit. on pp. 22, 28).

[17] Paul Soleillet. "Sur les paramètres caractérisant la polarisation partielle de la lumière dans les phénomènes de fluorescence". In: *Annales de Physique* 10.12 (1929), pp. 23–97. ISSN: 1286-4838. DOI: 10.1051/anphys/192910120023. URL: http://dx.doi.org/10.1051/anphys/192910120023 (cit. on p. 22).

[18] Valentina Curcio, Luis A. Alemán-Castañeda, Thomas G. Brown, et al. "Birefringent Fourier filtering for single molecule coordinate and height super-resolution imaging with dithering and orientation". In: *Nature Communications* 11.1 (Oct. 2020). DOI: 10.1038/s41467-020-19064-6. URL: https://doi.org/10.1038/s41467-020-19064-6 (cit. on pp. 22, 32, 56, 64, 65, 75, 88, 93).

[19] Emil Wolf. *Introduction to the Theory of Coherence and Polarization of Light*. Cambridge University Press, 2007 (cit. on pp. 23, 24).

[20] Luis Arturo Aleman Castaneda. "Structured light, polarization and birefringence". 2022AIXM0031. PhD thesis. 2022. URL: http://www.theses.fr/2022AIXM0031 (cit. on p. 24).

[21] Halina Rubinsztein-Dunlop, Andrew Forbes, M V Berry, et al. "Roadmap on structured light". In: *Journal of Optics* 19.1 (Nov. 2016), p. 013001. DOI: 10.1088/2040-8978/19/1/013001. URL: https://dx.doi.org/10.1088/2040-8978/19/1/013001 (cit. on pp. 24, 27, 35).

[22] Amber M. Beckley, Thomas G. Brown, and Miguel A. Alonso. "Full Poincaré beams". In: *Opt. Express* 18.10 (May 2010), pp. 10777–10785. DOI: 10.1364/OE.18.010777. URL: https://opg.optica.org/oe/abstract.cfm?URI=oe-18-10-10777 (cit. on pp. 24, 40).

[23] Isael Herrera, Luis A. Alemán-Castañeda, Sophie Brasselet, et al. "Stokes-based analysis for the estimation of 3D dipolar emission". In: *Journal of the Optical Society of America A* 41.11 (Oct. 2024), p. 2134. ISSN: 1520-8532. DOI: 10.1364/josaa.538706. URL: http://dx.doi.org/10.1364/JOSAA.538706 (cit. on pp. 26, 31, 50, 55, 70, 119).

[24] José J. Gil, Andreas Norrman, Ari T. Friberg, et al. "Polarimetric purity and the concept of degree of polarization". In: *Phys. Rev. A* 97 (2 Feb. 2018), p. 023838. DOI: 10.1103/PhysRevA.97.023838. URL: https://link.aps.org/doi/10.1103/PhysRevA.97.023838 (cit. on p. 26).

[25] Christian Brosseau and Aristide Dogariu. "Symmetry properties and polarization descriptors for an arbitrary electromagnetic wavefield". In: *Progress in Optics*. Elsevier, 2006, pp. 315–380. DOI: 10.1016/s0079-6638(06)49004-1. URL: http://dx.doi.org/10.1016/S0079-6638(06)49004-1 (cit. on p. 26).

[26] Jose J. Gil, Jose M. Correas, Pedro A. Melero, et al. "Generalized polarization algebra". In: *Monografias del Seminario Matematico Garcia de Galdeano* 31 (2004), pp. 161–167 (cit. on p. 27).

[27] Jeremy Ellis, Aristide Dogariu, Sergey Ponomarenko, et al. "Degree of polarization of statistically stationary electromagnetic fields". In: *Optics Communications* 248.4-6 (Apr. 2005), pp. 333–337. DOI: 10.1016/j.optcom.2004.12.050. URL: https://doi.org/10.1016/j.optcom.2004.12.050 (cit. on p. 27).

[28] Mark R. Dennis. "A three-dimensional degree of polarization based on Rayleigh scattering". In: *Journal of the Optical Society of America A* 24.7 (June 2007), p. 2065. ISSN: 1520-8532. DOI: 10.1364/josaa.24.002065. URL: http://dx.doi.org/10.1364/JOSAA.24.002065 (cit. on p. 27).

[29] Beth Schaefer, Edward Collett, Robert Smyth, et al. "Measuring the Stokes polarization parameters". In: *American Journal of Physics* 75.2 (Feb. 2007), pp. 163–168. ISSN: 1943-2909. DOI: 10.1119/1.2386162. URL: http://dx.doi.org/10.1119/1.2386162 (cit. on p. 27).

[30] K. G. Lee, H. W. Kihm, J. E. Kihm, et al. "Vector field microscopic imaging of light". In: *Nature Photonics* 1.1 (Dec. 2006), pp. 53–56. ISSN: 1749-4893. DOI: 10.1038/nphoton.2006.37. URL: http://dx.doi.org/10.1038/nphoton.2006.37 (cit. on p. 28).

[31] S. Tsesses, E. Ostrovsky, K. Cohen, et al. "Optical skyrmion lattice in evanescent electromagnetic fields". In: *Science* 361.6406 (Sept. 2018), pp. 993–996. DOI: 10.1126/science.aau0227. URL: https://doi.org/10.1126/science.aau0227 (cit. on pp. 28, 40).

[32] J. S. Eismann, L. H. Nicholls, D. J. Roth, et al. "Transverse spinning of unpolarized light". In: *Nature Photonics* 15.2 (Dec. 2020), pp. 156–161. ISSN: 1749-4893. DOI: 10.1038/s41566-020-00733-3. URL: http://dx.doi.org/10.1038/s41566-020-00733-3 (cit. on pp. 29, 30).

[33] Oumeng Zhang, Zijian Guo, Yuanyuan He, et al. "Six-dimensional single-molecule imaging with isotropic resolution using a multi-view reflector microscope". In: *Nature Photonics* 17.2 (Dec. 2022), pp. 179–186. ISSN: 1749-4893. DOI: 10.1038/s41566-022-01116-6. URL: http://dx.doi.org/10.1038/s41566-022-01116-6 (cit. on pp. 32, 70, 93, 118).

[34] Chao He, Yijie Shen, and Andrew Forbes. "Towards higher-dimensional structured light". In: *Light: Science amp; Applications* 11.1 (July 2022). ISSN: 2047-7538. DOI: 10.1038/s41377-022-00897-3. URL: http://dx.doi.org/10.1038/s41377-022-00897-3 (cit. on p. 35).

[35] Wei Ting Chen, Mohammadreza Khorasaninejad, Alexander Y. Zhu, et al. "Generation of wavelength-independent subwavelength Bessel beams using metasurfaces". In: *Light: Science amp; Applications* 6.5 (Dec. 2016), e16259–e16259. ISSN: 2047-7538. DOI: 10.1038/lsa.2016.259. URL: http://dx.doi.org/10.1038/lsa.2016.259 (cit. on p. 35).

[36] G. A. Siviloglou, J. Broky, A. Dogariu, et al. "Observation of Accelerating Airy Beams". In: *Physical Review Letters* 99.21 (Nov. 2007). ISSN: 1079-7114. DOI: 10.1103/physrevlett.99.213901. URL: http://dx.doi.org/10.1103/PhysRevLett.99.213901 (cit. on p. 35).

[37] Mark R. Dennis, Robert P. King, Barry Jack, et al. "Isolated optical vortex knots". In: *Nature Physics* 6.2 (Jan. 2010), pp. 118–121. ISSN: 1745-2481. DOI: 10.1038/nphys1504. URL: http://dx.doi.org/10.1038/nphys1504 (cit. on p. 35).

[38] Danica Sugic, Ramon Droop, Eileen Otte, et al. "Particle-like topologies in light". In: *Nature Communications* 12.1 (Nov. 2021). ISSN: 2041-1723. DOI: 10.1038/s41467-021-26171-5. URL: http://dx.doi.org/10.1038/s41467-021-26171-5 (cit. on p. 35).

[39] Yijie Shen, Qiang Zhang, Peng Shi, et al. "Optical skyrmions and other topological quasiparticles of light". In: *Nature Photonics* 18.1 (Dec. 2023), pp. 15–25. ISSN: 1749-4893. DOI: 10.1038/s41566-023-01325-7. URL: http://dx.doi.org/10.1038/s41566-023-01325-7 (cit. on p. 35).

[40] David Marco, Isael Herrera, Sophie Brasselet, et al. "Propagation-Invariant Optical Meron Lattices". In: *ACS Photonics* 11.6 (May 2024), pp. 2397–2405. ISSN: 2330-4022. DOI: 10.1021/acsphotonics.4c00292. URL: http://dx.doi.org/10.1021/acsphotonics.4c00292 (cit. on pp. 35, 40, 119).

[41] David Marco, Isael Herrera, Sophie Brasselet, et al. "Periodic skyrmionic textures via conformal cartographic projections". In: *APL Photonics* 9.11 (Nov. 2024). ISSN: 2378-0967. DOI: 10.1063/5.0230959. URL: http://dx.doi.org/10.1063/5.0230959 (cit. on pp. 35, 40, 41, 45, 119).

[42] Christian Maurer, Alexander Jesacher, Severin Fürhapter, et al. "Tailoring of arbitrary optical vector beams". In: *New Journal of Physics* 9.3 (Mar. 2007), pp. 78–78. ISSN: 1367-2630. DOI: 10.1088/1367-2630/9/3/078. URL: http://dx.doi.org/10.1088/1367-2630/9/3/078 (cit. on p. 37).

[43] Eliot Bolduc, Nicolas Bent, Enrico Santamato, et al. "Exact solution to simultaneous intensity and phase encryption with a single phase-only hologram". In: *Optics Letters* 38.18 (Sept. 2013), p. 3546. ISSN: 1539-4794. DOI: 10.1364/ol.38.003546. URL: http://dx.doi.org/10.1364/OL.38.003546 (cit. on p. 37).

[44] Naoto Nagaosa and Yoshinori Tokura. "Topological properties and dynamics of magnetic skyrmions". In: *Nature nanotechnology* 8.12 (2013), pp. 899–911 (cit. on p. 39).

[45] Hao Ge, Xiang-Yuan Xu, Le Liu, et al. "Observation of acoustic skyrmions". In: *Physical Review Letters* 127.14 (2021), p. 144502 (cit. on p. 39).

[46] R. Rantanen and V. B. Eltsov. "Transition in vortex skyrmion structures in superfluid ^{3}He–A driven by an analog of the zero-charge effect". In: *Phys. Rev. B* 107 (10 Mar. 2023), p. 104505. DOI: 10.1103/PhysRevB.107.104505. URL: https://link.aps.org/doi/10.1103/PhysRevB.107.104505 (cit. on p. 39).

[47] Yijie Shen, Qiang Zhang, Peng Shi, et al. "Topological quasiparticles of light: optical skyrmions and beyond". In: *arXiv preprint arXiv:2205.10329* (2022) (cit. on p. 39).

[48] Rodrigo Gutierrez-Cuevas and Emilio Pisanty. "Optical polarization skyrmionic fields in free space". In: *Journal of Optics* 23.2 (Mar. 2021), p. 024004. DOI: 10.1088/2040-8986/abe8b2. URL: https://dx.doi.org/10.1088/2040-8986/abe8b2 (cit. on p. 40).

[49] Luping Du, Aiping Yang, Anatoly V Zayats, et al. "Deep-subwavelength features of photonic skyrmions in a confined electromagnetic field with orbital angular momentum". In: *Nature Physics* 15.7 (2019), pp. 650–654 (cit. on p. 40).

[50] Charles S Peirce. "A quincuncial projection of the sphere". In: *American Journal of Mathematics* 2.4 (1879), pp. 394–396 (cit. on p. 41).

[51] Oscar Sherman Adams. *Elliptic functions applied to conformal world maps*. Vol. 297. US Government Printing Office, 1925, pp. 72–78 (cit. on p. 41).

[52] LP Lee. "Some conformal projections based on elliptic functions". In: *Geographical Review* 55.4 (1965), pp. 563–580 (cit. on p. 42).

[53] LP Lee. "Conformal Projections Based On Dixon Elliptic Functions". In: *Cartographica: The International Journal for Geographic Information and Geovisualization* 13.1 (1976), pp. 38–66 (cit. on pp. 42, 132).

[54] Mohamadreza Fazel, Kristin S. Grussmayer, Boris Ferdman, et al. "Fluorescence microscopy: A statistics-optics perspective". In: *Rev. Mod. Phys.* 96 (2 June 2024), p. 025003. DOI: 10.1103/RevModPhys.96.025003. URL: https://link.aps.org/doi/10.1103/RevModPhys.96.025003 (cit. on p. 50).

[55] "Electromagnetic Diffraction in Optical Systems. II. Structure of the Image Field in an Aplanatic System". In: *Proceedings of the Royal Society of London. Series A. Mathematical and Physical Sciences* 253.1274 (Dec. 1959), pp. 358–379. ISSN: 2053-9169. DOI: 10.1098/rspa.1959.0200. URL: http://dx.doi.org/10.1098/rspa.1959.0200 (cit. on p. 54).

[56] Adam S. Backer and W. E. Moerner. "Extending Single-Molecule Microscopy Using Optical Fourier Processing". In: *The Journal of Physical Chemistry B* 118.28 (2014). PMID: 24745862, pp. 8313–8329. DOI: 10.1021/jp501778z. eprint: https://doi.org/10.1021/jp501778z. URL: https://doi.org/10.1021/jp501778z (cit. on p. 54).

[57] Adam S. Backer and W. E. Moerner. "Extending Single-Molecule Microscopy Using Optical Fourier Processing". In: *The Journal of Physical Chemistry B* 118.28 (July 2014), pp. 8313–8329. DOI: 10.1021/jp501778z. URL: https://doi.org/10.1021/jp501778z (cit. on pp. 55, 70).

[58] Cesar Augusto Valades Cruz, Haitham Ahmed Shaban, Alla Kress, et al. "Quantitative nanoscale imaging of orientational order in biological filaments by polarized superresolution microscopy". In: *Proceedings of the National Academy of Sciences* 113.7 (Feb. 2016). ISSN: 1091-6490. DOI: 10.1073/pnas.1516811113. URL: http://dx.doi.org/10.1073/pnas.1516811113 (cit. on pp. 56, 63, 64).

[59] Jeongmo Kim, Reinaldo Chacón, Zijun Wang, et al. "Measuring 3D orientation of nanocrystals via polarized luminescence of rare-earth dopants". In: *Nature Communications* 12.1 (Mar. 2021). ISSN: 2041-1723. DOI: 10.1038/s41467-021-22158-4. URL: http://dx.doi.org/10.1038/s41467-021-22158-4 (cit. on p. 56).

[60] Caio Vaz Rimoli, Cesar Augusto Valades-Cruz, Valentina Curcio, et al. "4polar-STORM polarized super-resolution imaging of actin filament organization in cells". In: *Nature Communications* 13.1 (2022), p. 301. DOI: 10.1038/s41467-022-27966-w. URL: https://doi.org/10.1038/s41467-022-27966-w (cit. on pp. 56, 57, 64, 79, 116, 121).

[61] Martin Böhmer and Jörg Enderlein. "Orientation imaging of single molecules by wide-field epifluorescence microscopy". In: *Journal of the Optical Society of America B* 20.3 (Mar. 2003), p. 554. ISSN: 1520-8540. DOI: 10.1364/josab.20.000554. URL: http://dx.doi.org/10.1364/JOSAB.20.000554 (cit. on pp. 56, 60–62).

[62] Mikael P. Backlund, Matthew D. Lew, Adam S. Backer, et al. "Simultaneous, accurate measurement of the 3D position and orientation of single molecules". In: *Proceedings of the National Academy of Sciences* 109.47 (Nov. 2012), pp. 19087–19092. ISSN: 1091-6490. DOI: 10.1073/pnas.1216687109. URL: http://dx.doi.org/10.1073/pnas.1216687109 (cit. on p. 56).

[63] Adam S. Backer, Mikael P. Backlund, Matthew D. Lew, et al. "Single-molecule orientation measurements with a quadrated pupil". In: *Optics Letters* 38.9 (Apr. 2013), p. 1521. ISSN: 1539-4794. DOI: 10.1364/ol.38.001521. URL: http://dx.doi.org/10.1364/OL.38.001521 (cit. on p. 56).

[64] Oumeng Zhang, Jin Lu, Tianben Ding, et al. "Imaging the three-dimensional orientation and rotational mobility of fluorescent emitters using the Tri-spot point spread function". In: *Applied Physics Letters* 113.3 (July 2018). DOI: 10.1063/1.5031759. URL: https://doi.org/10.1063/1.5031759 (cit. on p. 56).

[65] Oumeng Zhang, Weiyan Zhou, Jin Lu, et al. "Resolving the Three-Dimensional Rotational and Translational Dynamics of Single Molecules Using Radially and Azimuthally Polarized Fluorescence". In: *Nano Letters* 22.3 (Jan. 2022), pp. 1024–1031. DOI: 10.1021/acs.nanolett.1c03948. URL: https://doi.org/10.1021/acs.nanolett.1c03948 (cit. on pp. 56, 64, 65).

[66] Petr Bouchal, Petr Dvořák, Martin Hrtoň, et al. "Single-Shot Aspect Ratio and Orientation Imaging of Nanoparticles". In: *ACS Photonics* 10.9 (Aug. 2023), pp. 3331–3341. ISSN: 2330-4022. DOI: 10.1021/acsphotonics.3c00785. URL: http://dx.doi.org/10.1021/acsphotonics.3c00785 (cit. on pp. 56, 64, 65).

[67] Tingting Wu, Jin Lu, and Matthew D. Lew. "Dipole-spread-function engineering for simultaneously measuring the 3D orientations and 3D positions of fluorescent molecules". In: *Optica* 9.5 (May 2022), p. 505. ISSN: 2334-2536. DOI: 10.1364/optica.451899. URL: http://dx.doi.org/10.1364/OPTICA.451899 (cit. on pp. 56, 72).

[68] Bo Huang, Wenqin Wang, Mark Bates, et al. "Three-Dimensional Super-Resolution Imaging by Stochastic Optical Reconstruction Microscopy". In: *Science* 319.5864 (Feb. 2008), pp. 810–813. ISSN: 1095-9203. DOI: 10.1126/science.1153529. URL: http://dx.doi.org/10.1126/science.1153529 (cit. on p. 56).

[69] Yoav Shechtman, Steffen J. Sahl, Adam S. Backer, et al. "Optimal Point Spread Function Design for 3D Imaging". In: *Physical Review Letters* 113.13 (Sept. 2014). ISSN: 1079-7114. DOI: 10.1103/physrevlett.113.133902. URL: http://dx.doi.org/10.1103/PhysRevLett.113.133902 (cit. on pp. 56, 72).

[70] Sri Rama Prasanna Pavani, Michael A. Thompson, Julie S. Biteen, et al. "Three-dimensional, single-molecule fluorescence imaging beyond the diffraction limit by using a double-helix point spread function". In: *Proceedings of the National Academy of Sciences* 106.9 (Mar. 2009), pp. 2995–2999. ISSN: 1091-6490. DOI: 10.1073/pnas.0900245106. URL: http://dx.doi.org/10.1073/pnas.0900245106 (cit. on p. 56).

[71] Tianben Ding and Matthew D. Lew. "Single-Molecule Localization Microscopy of 3D Orientation and Anisotropic Wobble Using a Polarized Vortex Point Spread Function". In: *The Journal of Physical Chemistry B* 125.46 (Nov. 2021), pp. 12718–12729. ISSN: 1520-5207. DOI: 10.1021/acs.jpcb.1c08073. URL: http://dx.doi.org/10.1021/acs.jpcb.1c08073 (cit. on pp. 64, 65).

[72] Adriaan van den Bos. *Parameter Estimation for Scientists and Engineers*. Wiley, Mar. 2007. ISBN: 9780470173862. DOI: 10.1002/9780470173862. URL: http://dx.doi.org/10.1002/9780470173862 (cit. on p. 68).

[73] Elias Nehme, Daniel Freedman, Racheli Gordon, et al. "DeepSTORM3D: dense 3D localization microscopy and PSF design by deep learning". In: *Nature Methods* 17.7 (June 2020), pp. 734–740. ISSN: 1548-7105. DOI: 10.1038/s41592-020-0853-5. URL: http://dx.doi.org/10.1038/s41592-020-0853-5 (cit. on p. 72).

[74] Anurag Agrawal, Sean Quirin, Ginni Grover, et al. "Limits of 3D dipole localization and orientation estimation for single-molecule imaging: towards Green's tensor engineering". In: *Optics Express* 20.24 (Nov. 2012), p. 26667. ISSN: 1094-4087. DOI: 10.1364/oe.20.026667. URL: http://dx.doi.org/10.1364/OE.20.026667 (cit. on p. 77).

[75] Shuang Fu, Wei Shi, Tingdan Luo, et al. "Field-dependent deep learning enables high-throughput whole-cell 3D super-resolution imaging". In: *Nature Methods* 20.3 (Feb. 2023), pp. 459–468. ISSN: 1548-7105. DOI: 10.1038/s41592-023-01775-5. URL: http://dx.doi.org/10.1038/s41592-023-01775-5 (cit. on pp. 79, 121).

[76] Stephen Boyd and Lieven Vandenberghe. *Introduction to Applied Linear Algebra: Vectors, Matrices, and Least Squares*. Cambridge University Press Assessment, June 2018. ISBN: 9781316518960. DOI: 10.1017/9781108583664. URL: http://dx.doi.org/10.1017/9781108583664 (cit. on p. 83).

[77] François Goudail. "Performance comparison of pseudo-inverse and maximum-likelihood estimators of Stokes parameters in the presence of Poisson noise for spherical design-based measurement structures". In: *Optics Letters* 42.10

(May 2017), p. 1899. ISSN: 1539-4794. DOI: 10.1364/ol.42.001899. URL: http://dx.doi.org/10.1364/OL.42.001899 (cit. on p. 84).

[78] R. Vio, J. Bardsley, and W. Wamsteker. "Least-squares methods with Poissonian noise: Analysis and comparison with the Richardson-Lucy algorithm". In: *Astronomy & amp; Astrophysics* 436.2 (May 2005), pp. 741–755. ISSN: 1432-0746. DOI: 10.1051/0004-6361:20041997. URL: http://dx.doi.org/10.1051/0004-6361:20041997 (cit. on p. 84).

[79] Christian Mätzler. "MATLAB functions for Mie scattering and absorption, version 2". In: (2002) (cit. on pp. 99, 100).

[80] Valentina Curcio. "Polarized super-resolution imaging of single molecules orientations in 3D". 2020AIXM0306. PhD thesis. 2020. URL: http://www.theses.fr/2020AIXM0306/document (cit. on pp. 111, 119).

[81] Robert M. Dickson, D. J. Norris, and W. E. Moerner. "Simultaneous Imaging of Individual Molecules Aligned Both Parallel and Perpendicular to the Optic Axis". In: *Phys. Rev. Lett.* 81 (24 Dec. 1998), pp. 5322–5325. DOI: 10.1103/PhysRevLett.81.5322. URL: https://link.aps.org/doi/10.1103/PhysRevLett.81.5322 (cit. on p. 112).

[82] Rodrigo Gutiérrez-Cuevas, Luis A Alemán-Castañeda, Isael Herrera, et al. "Vectorial phase retrieval in super-resolution polarization microscopy". In: *APL Photonics* 9.2 (2024) (cit. on p. 121).

ANNEXES

A. Complementary expressions.

.1. Conformal maps.

For Peirce's and Adams' projections, $w(z)$ is the inverse function of the Schwarz-Christoffel transformation that maps the unit disk onto a square and an equilateral triangle [53], respectively. The expressions for $w(z)$ of the Peirce, Adams, Lee, and Wray [53]) are:

$$w_{\mathrm{P}}(z) = \frac{e^{i(\phi_0+\alpha)}}{\sqrt{2}}\mathrm{sd}\left(\tilde{z}_1, \frac{1}{\sqrt{2}}\right), \tag{A.1a}$$

$$w_{\mathrm{A}}(z) = e^{i(\phi_0+\alpha)}\mathrm{sm}(\tilde{z}_2), \tag{A.1b}$$

$$w_{\mathrm{L}}(z) = 2^{1/6}e^{i(\phi_0+\alpha)}\mathrm{sm}(\tilde{z}_2)\mathrm{cm}(\tilde{z}_2), \tag{A.1c}$$

$$w_{\mathrm{W}}(z) = \frac{e^{i(\phi_0+\alpha)}}{2}\mathrm{sd}\left(\tilde{z}_3, \frac{\sqrt{3}-1}{2\sqrt{2}}\right), \tag{A.1d}$$

where sd is the ratio between the Jacobi elliptic functions sn and dn, while sm and cm correspond to the Dixon elliptic functions, which can be expressed in terms of the Weierstrass elliptic function denoted as $\wp(z)$ and its derivative $\wp'(z)$: $\mathrm{sm}(z) = 6\wp(z)/(1-3\wp'(z))$ and $\mathrm{cm}(z) = (3\wp'(z)+1)/(3\wp'(z)-1)$. The three complex numbers $\tilde{z}_i$ are defined as $\tilde{z}_{1,2,3} = \gamma_{1,2,3}\, e^{-i\alpha}(z-z_0)/d$, with $\gamma_1 = \Gamma^2(1/4)/(2\sqrt{2\pi})$, $\gamma_2 = \Gamma^3(1/3)/(2\pi)$, and $\gamma_3 = 3^{1/4}\Gamma^3(1/3)/(2^{1/3}\pi)$, where Γ denotes the gamma function.

.2. Computation of the Stokes-Gell-Mann derivatives basis.

For simplicity, we avoid labeling the basis elements of each polarization channel σ, but it is important to remember that this calculation must be done for each component. Let us first focus on the computation of $\partial_{x0} I_0$ (the derivatives of the other spatial variables being performed similarly):

$$\partial_{x0} I_0 = \frac{1}{\sqrt{3}}\sum \partial_{x0} I^j = \frac{1}{\sqrt{3}}\sum \partial_{x0}\left(E^{j*}E^j\right) = \frac{1}{\sqrt{3}}\sum \partial_{x0}\left(E^{j*}\right)E^j + E^{j*}\partial_{x0}\left(E^j\right), \tag{A.2}$$

where I^j and E^j are the intensity and field distributions at the image plane associated with a dipole oriented along the j axis in the sample volume. We can then focus only on the computation of $\partial_{x0}E^j$. The field E^j can be computed by calculating the 2D Fourier transform of the field at the pupil plane $E^j = \mathrm{FT}[E^j_{Pup}]$, so $\partial_{x0}E^j = \mathrm{FT}[\partial_{x0}E^j_{Pup}]$, because the derivative is taken in the dipole coordinates. In Chapter 2

we show that E^j_{Pup} can be decomposed in terms of the Green tensor and the dipole moment, $E^j = \mathbf{G}_{Pup}(\mathbf{r},\mathbf{r}_0)\cdot\hat{\mu^j}$. The explicit dependence on $\mathbf{r}_0$ is given by

$$E^j = e^{-i\left[k_1\left(x_0\frac{x}{r}+y_0\frac{y}{r}\right)-z_0k_1\sqrt{1-\left(\frac{k_2\rho}{k_1 r}\right)^2}\right]}e^{idk_2\sqrt{1-\left(\frac{\rho}{r}\right)^2}}\mathbf{G}_{Pup}(\mathbf{r})\cdot\hat{\mu^j}, \tag{A.3}$$

hence, $\partial_{x0}E^j_{Pup} = -ik_1x/rE^j_{Pup}$. And similar for the rest of the spatial variables. We can then use this expression to compute the derivatives of the field and the intensity in the image plane. The spatial derivatives of I_0, I_{11}, I_{12} are linear combinations of intensities and can be computed similarly.

The remaining basis elements are expressed in terms of $\mathrm{Re}(E^{j*}E^k)$ or $\mathrm{Im}(E^{j*}E^k)$, that can be written as

$$\partial_{x0}\mathrm{Re}(E^{j*}E^k) = \frac{1}{2}\partial_{x0}\left[E^{j*}E^k + E^jE^{k*}\right], \tag{A.4}$$

$$\partial_{x0}\mathrm{Im}(E^{j*}E^k) = \frac{1}{2}\partial_{x0}\left[E^{j*}E^k - E^jE^{k*}\right]. \tag{A.5}$$

$$\tag{A.6}$$

By inserting on the left side the expressions for the fields E^j and E^{j*}, we can compute I_{21}, I_{22}, I_{23}, I_{31}, I_{32} and I_{33}